Sulfide Metabolism Controls Physiological Adaptation in *vhl-1* Mutants and Underlies Mesna-Mediated Cytoprotection via *sqrd-1*/*Sqor* in *C. elegans* and Renal Cells

Doctoral thesis

for

the award of the doctoral degree of the

Faculty of Mathematics and Natural Sciences of the

University of Cologne

submitted by

Willian Goulart Salgueiro

From Uruguaiana, Brazil

Köln, October 2025

Table of contents

List of figures

List of tables

List of abbreviations

ACN — acetonitrile
AE-1 — anion exchanger 1
AKI — acute kidney injury
AMP — adenosine monophosphate
AMPK — AMP-activated protein kinase
AP39 — mitochondria-targeted hydrogen sulfide donor
AST — aspartate aminotransferase (GOT)
ATP — adenosine triphosphate
BCA — bicinchoninic acid (total Protein quantification)
BSA — bovine serum albumin
BODIPY C11 — lipid peroxidation-sensitive boron-dipyrromethene dye
CAT — cysteine aminotransferase
CBS/CBS-1 — cystathionine β-synthase
cDNA — complementary DNA
cGMP — cyclic guanosine monophosphate
CKD — chronic kidney disease
CO — carbon monoxide
CoA — coenzyme A
CoM — coenzyme M (Mesna)
CoQ/CoQ10 — coenzyme Q/ubiquinone-10
CTB — cetyltrimethylammonium bromide
Cth — cystathionine
CTCF — corrected total cell fluorescence
Cys — cysteine
DADS — diallyl disulfide
DATS — diallyl trisulfide
DAO — D-amino acid oxidase
DAS — diallyl sulfide
DHA — dihydroascorbic acid
DHLA — dihydrolipoic acid
DIC — differential interference contrast
DMSO — dimethyl sulfoxide
DMEM — Dulbecco's Modified Eagle Medium
DMEM/F12 — Dulbecco's Modified Eagle Medium/Nutrient Mixture F-12
DNA — deoxyribonucleic acid
dNTP — deoxynucleoside triphosphate
DTNB — 5,5′-dithiobis(2-nitrobenzoic acid)
DTT — dithiothreitol
ECL — enhanced chemiluminescence
EDTA — ethylenediaminetetraacetic acid
EGTA — ethylene glycol-bis(β-aminoethyl ether)-N,N,N′,N′-tetraacetic acid
ER — endoplasmic reticulum
ETC — electron transport chain
ETHE-1/ETHE1 — sulfur dioxygenase (SDO)
FAD — flavin adenine dinucleotide
FBS — fetal bovine serum
FDR — false discovery rate
FUDR — 5-fluoro-2′-deoxyuridine

GFR — glomerular filtration rate
GOT/GOT-1/GOT-2 — glutamate-oxaloacetate transaminase (GOT)
GPx/GPX4 — glutathione peroxidase/glutathione peroxidase 4
GSH — reduced glutathione
GSSG — oxidized glutathione (glutathione disulfide)
GSSH — glutathione persulfide
GST/GSTs — glutathione S-transferase(s)
GYY4137 — slow-releasing hydrogen sulfide donor
HBSS — Hanks' balanced salt solution
HEPES — 4-(2-hydroxyethyl)-1-piperazineethanesulfonic acid
HIF-1/HIF-1α — hypoxia-inducible factor-1/alpha subunit
HPLC — high-performance liquid chromatography
HPLC-MS/MS (LC–MS/MS) — liquid chromatography–tandem mass spectrometry
HRE — hypoxia response element
H_2S — hydrogen sulfide
Hcy — homocysteine
HSip-1 — hydrogen sulfide fluorescent probe
HSP — heat shock protein
IAM — iodoacetamide
HPE-IAM — N-(1-pyrenyl)maleimide-enhanced iodoacetamide
ICAM-1 — intercellular adhesion molecule 1
IF — immunofluorescence
IL — interleukin
IRI — ischemia–reperfusion injury
KEAP1/NRF2 — Kelch-like ECH-associated protein 1/nuclear factor erythroid 2-related factor 2
LC–MS — liquid chromatography–mass spectrometry
LDHA — lactate dehydrogenase A
LDL — low-density lipoprotein
LDH — lactate dehydrogenase
LDS — lithium dodecyl sulfate
LPS — lipopolysaccharide
MALDI — matrix-assisted laser desorption/ionization
MAPK — mitogen-activated protein kinase
MMP — mitochondrial membrane potential
MPST/MPST-1/MPST-3 — 3-mercaptopyruvate sulfurtransferase
MPP — mitochondrial processing peptidase
mRNA — messenger RNA
mIMCD3 — mouse inner medullary collecting duct
MST-SS — MPST-bound persulfide intermediate
MTS — mitochondrial targeting sequence
MitoSOX — mitochondrial superoxide probe
NAD^+ — nicotinamide adenine dinucleotide (oxidized)
NADH — nicotinamide adenine dinucleotide (reduced)
NaHS — sodium hydrosulfide
Na_2S — sodium sulfide
NF-κB — nuclear factor kappa-light-chain-enhancer of activated B cells
NGM — nematode growth medium
NLRP3 — NOD-like receptor protein 3 inflammasome
NO — nitric oxide
NRF2/SKN-1 — nuclear factor erythroid 2–related factor 2

OCR — oxygen consumption rate
OXPHOS — oxidative phosphorylation
PAA — polyacrylamide
PBS — phosphate-buffered saline
PDH — pyruvate dehydrogenase
PDK1 — pyruvate dehydrogenase kinase 1
PFA — paraformaldehyde
PGC-1α — peroxisome proliferator-activated receptor-γ coactivator-1α
PLP — Pyridoxal-5'-phosphate
PMSF — phenylmethylsulfonyl fluoride
Pyr — pyruvate
Q — ubiquinone (coenzyme Q)
QH_2 — ubiquinol (reduced coenzyme Q)
RIPA — radioimmunoprecipitation assay buffer
RNA — ribonucleic acid
RNAi — RNA interference
ROS — reactive oxygen species
RNS — reactive nitrogen species
SDO — sulfur dioxygenase *(*SDO*)*
Ser — serine
SDS — sodium dodecyl sulfate
SEM — standard error of the mean/scanning electron microscopy
SOD — superoxide dismutase
SO_3^{-2} — Sulfite
SO_4^{-2} — Sulfate
SSO_3^{-2} — Thiosulfate
SO/SUOX-1/SUOX — sulfite oxidase
SQOR/SQRD-1 — sulfide:quinone oxidoreductase
SQR-SSH — SQOR-bound persulfide intermediate
SSP4 — sulfane sulfur probe 4
SUIT — substrate–uncoupler–inhibitor titration
TAE — Tris–acetate–EDTA buffer
TBS — Tris-buffered saline
TCA — tricarboxylic acid cycle
TCEP — tris(2-carboxyethyl)phosphine
TEM — transmission electron microscopy
TIM/TOM — translocase of inner/outer mitochondrial membrane
TMRE — tetramethylrhodamine ethyl ester
TRX — thioredoxin
TRXR-1/TXNRD1 — cytosolic thioredoxin reductase
TRXR-2/TXNRD2 — mitochondrial thioredoxin reductase
TST (rhodanese) — thiosulfate sulfurtransferase
TTFA — thenoyltrifluoroacetone
UPRmt — mitochondrial unfolded protein response
VHL/pVHL/VHL-1 — von Hippel–Lindau protein
WT — wild type
Z-stack — optical section stack in fluorescence microscopy

1. Abstract

Hydrogen sulfide (H_2S) has emerged as a critical gaseous mediator at the intersection of hypoxia signaling, redox balance, and mitochondrial function. However, the mechanisms by which H_2S metabolism influences hypoxia-inducible factor (HIF-1) activity, organismal resilience, and lifespan remain incompletely understood. This thesis addresses three central questions: (i) which and how sulfide-metabolizing enzymes mediate the phenotypic consequences of HIF-1 activation in *Caenorhabditis elegans*, (ii) how H_2S and persulfide metabolism interact with the hypoxia pathway to shape stress resistance and longevity, and (iii) whether Mesna, an FDA-approved thiol drug, can be repurposed as a modulator of sulfide/persulfide metabolism with protective effects in ischemia–reperfusion injury. By combining genetics, proteomics, and functional assays in *C. elegans* and kidney cells, I dissect the contribution of specific enzymes—mainly *sqrd-1*/*Sqo*r—to hypoxia adaptation, mitochondrial remodeling, and drug responsiveness.

Genetic analysis identified *sqrd-1(mr28)*, (sulfide:quinone oxidoreductase), as a determinant of lifespan and body size in *vhl-1*(*ok161*) mutants, linking sulfide detoxification to HIF-1-driven adaptations. Proteomics and functional assays revealed that *sqrd-1* loss reprograms mitochondrial pathways, suggesting that sulfide flux directly modulates oxidative phosphorylation. Collagen hydroxylases and glutathione-S-transferases further emerged as lifespan regulators in the *vhl-1* background, highlighting cross-talk between extracellular matrix remodeling, detoxification, and hypoxia signaling. Most importantly, we identified subunits of the mitochondrial complex I seem to mediate the long lifespan of *vhl-1(ok161)* mutants in a *sqrd-1*-dependent manner.

Mesna preconditioning protected *C. elegans* against hypoxia, protein aggregation, paraquat-induced oxidative stress and shortened lifespan, with effects partly dependent on sulfide metabolism. Mechanistically, Mesna improved the redox state by shifting the glutathione pool toward a reduced state, promoted persulfide accumulation, and altered mitochondrial proteome signatures. In *sqrd-1*(*mr28*) knockout mutants, Mesna conferred even greater protection, while *mpst-1*(*ok2040*) mutation ablated the protective effect, underscoring enzyme-specific modulation. In mIMCD3 cells, Mesna preconditioning prevented paraquat-induced cell death, reduced mitochondrial ROS

and lipid peroxidation, and improved ATP maintenance in a SQOR-dependent manner. These findings point to Mesna as a novel modulator of sulfide/persulfide metabolism with translational relevance for renal IRI.

Overall, this work implicates sulfide metabolism as a key player in hypoxia adaptation, lifespan, and mitochondrial resilience, and positions Mesna as a clinically relevant candidate for repurposing in kidney protection strategies.

2. Introduction

2.1. Hydrogen sulfide as a signalling molecule

For a long time H_2S was known only as a toxin, mostly of environmental or occupational relevance, with much of the early literature being directed to its removal from petroleum and pulp products [1]. It has been first proposed as an endogenous signalling molecule in 1996 by the seminal work from Abe and Kimura [2], together with NO (nitric oxide) and CO (carbon monoxide) [34]. According to the coiner of this term, Wang 2002 [5], a gasotransmitter is endogenously produced, freely permeates cell membranes, and has specific signalling functions and molecular targets. The acknowledgement of H_2S as a gasotransmitter has renewed interest in this molecule and pushed the literature around it to considerably grow in size: the number of publications listed in PubMed using H_2S as a keyword increased by more than seven-fold since 1980. Such fast development was the basis to the development of several probes that allow for H_2S detection, thus making exploration of its roles in biological signalling in various organs and systems possible [67]. At a subcellular level, H_2S has indeed been described to modulate a plethora of biological processes from cytotoxicity to cytoprotection [8]. Organs and systems wise, it has been described to regulate important physiological functions such as vasodilation [9], neuromodulation [10], and anti-inflamatory [11].

2.1.2. Hydrogen sulfide chemistry

H_2S is a colourless, flammable gas that has a strong smell of rotten eggs. Due to its small size and high polarity, it is easily soluble in both water and lipids. Being small and lipophilic, it can cross membranes, but it can also be transported by different anion exchangers (AE-1, Cl^-, HCO_3^-) [12]. Since its pKa is 6.8, lower than most biologically relevant thiols (e.g. glutathione), under physiological conditions about 1/5 of it exists in its undissociated form, while the rest is dissociated to HS- (hydrosulfide anion) and H^+ [13,14], and a very small portion exists as S^{2-}. These three species together are commonly referred to as the total free sulfide pool in cells, and it is still unclear if H_2S, HS-, or both are responsible for the biological activities [15]. The hydrosulfide anion can be enzymatically converted into several different species, being oxidised to species such as sulfite (SO_3^{2-}), sulfate (SO_4^{2-}), thiosulfate ($S_2O_3^{2-}$), and polysulfides (S_x^{2-}) in the presence of O_2. Due to its high vapour pressure (1740kPa at 21°), its concentration

can be halved in solution, or even within cells, in a matter of minutes [16]. In light of such chemical diversity, instability, and the freely diffusible nature of all its derivatives, H_2S and its biological role are challenging to study.

2.1.3. Hydrogen sulfide biosynthesis

Enzymatic production of H_2S is mediated by three main enzymes: cystathionine β-lyase (CBS), cystathionine γ-lyase (CSE), and 3-mercaptopyruvate sulfurtransferase (3-MST). While CBS and CSE directly break down cysteine as part of the transulfuration pathway, which is the main route for processing sulfur-containing amino acids, 3-MST works on cysteine indirectly, relying on cysteine aminotransferase (CAT), another enzyme from the same pathway [17,18]. In the cytosol, H_2S is synthesized by CBS or CSE from either L-homocysteine (Hcy) or L-cysteine (Cys), as pointed in the left and center of **Figure 1**. The successive actions of CAT and 3-MST on cysteine yield 3-mercaptopyruvate (3-MP) and, subsequently, 3-MP persulfide (3-MST-SS), as it is displayed in the bottom center and left of **Figure 1,** highlighted in yellow equally as its equivalent in the mitochondria, since both CAT and MST can be both also found there [19]. From 3-MP-SS, H_2S can be released by reductants such as the enzyme thioredoxin (Trx) or the endogenous metabolite dihydrolipoic acid (DHLA), as it is displayed in the bottom right of **Figure 1**. A representative scheme with all reactions involved in H_2S synthesis, including the transulfuration pathway, is provided in **Figure 1**.

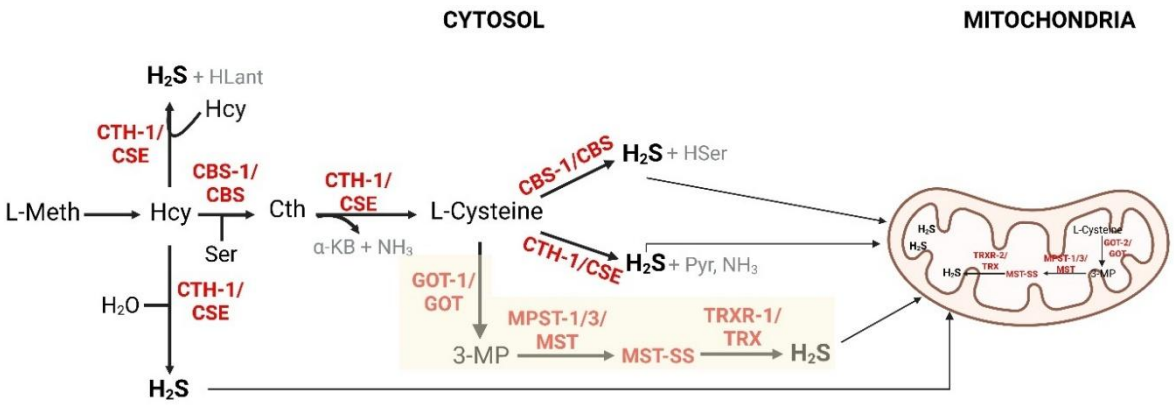

Figure 1. The different H2S production sources.

In the transulfuration pathway, L-methionine is first converted to homocysteine (Hcy), which is metabolized by cystathionine β-synthase (CBS-1/CBS) or cystathionine γ-lyase (CTH-1/CSE) to form cystathionine (Cth) and ultimately L-cysteine. CTH-1/CSE also contributes directly to H_2S generation from homocysteine or cysteine. CBS-1/CBS and CTH-1/CSE catalyze the conversion of L-cysteine into H_2S via multiple reactions, releasing by-products such as pyruvate (Pyr), ammonia (NH_3), and homoserine (HSer), depending on the reaction route. An additional pathway involves the conversion of L-cysteine into 3-mercaptopyruvate (3-MP) via glutamate–oxaloacetate transaminase (GOT-1/GOT). 3-MP is then used by 3-mercaptopyruvate sulfurtransferase (MPST-1/MPST-3/MPST) to produce a protein-bound persulfide intermediate (MST-SS), which is further reduced by thioredoxin (TRXR-1/TRX) to release free H_2S. Highlighted equally in yellow in both cytosol and mitochondria, conversion of 3-MP into H_2S via MPST-1/MPST-3/MPST can occur also in this organelle. However, in the mitochondria the glutamate-oxaloacetate transaminase is GOT-2 and the thioredoxin reductase is TRXR-2. Also in the mitochondria, H_2S synthesis may be directly tied to respiration. This figure was created in https://BioRender.com

In the transulfuration pathway, CBS catalyzes the β-replacement of homocysteine with serine and that yields a cystathionine. Cystathionine formation commits the sulfur from homocysteine to go through the end of this pathway. In the next step CSE α,γ-eliminates cystathionine, yielding cysteine, α-ketobutyrate, and NH_3. From cysteine, both CBS and CSE can generate H_2S via β-elimination reactions, with the difference being that CSE will yield pyruvate (Pyr) and NH_3 in the process, while CBS will only produce a serine (Ser) in addition to H_2S. CAT then transfers an amine group from α-ketoglutarate to cysteine to produce 3-MP, which can finally yield H_2S when 3-MST removes a sulfur from it and forms a persulfide on itself (3-MST-SSH). This persulfide bound to 3-MST can produce release H_2S when Trx or DHLA reduce it, releasing its terminal sulfur as H_2S.

Moreover, just like other pyridoxal 5'phosphate (PLP)-dependent enzymes CBS, CSE, and CAT have a level of substrate promiscuity [20], yielding H_2S from different sources. For example, two molecules of cysteine can generate lanthionine (Lan) via CBS, while

one molecule of homocysteine and one of cysteine can yield cystathionine (Cth) via CSE [21]. However, among these different routes, it has been shown that cystathionine formation from cysteine plus homocysteine via CSE tends to be the predominant reaction [22].

These enzymes exhibit distinct localisation patterns at the subcellular level. While CBS and CSE are mostly considered to be cytosolic, they have been reported to be translocated to the mitochondria under stress or hypoxia [23,24]. There, their role is not completely elucidated, even though it is unlikely to be related to direct production of energy. In principle, this would be possible via the electrons H_2S catabolism can donate to the electron transport chain. However, this path is not expected to be sufficient for sustaining ATP production [23]. Regarding 3-MST, the mitochondrial matrix seems to be its primary subcellular site of location, but it is also commonly found in the cytosol, depending on the metabolic state of the cell and if a stress condition is faced [25,26]. Regarding their expression in different organs, CBS is the predominant enzyme in the heart, while CBS is enriched in the brain [27], two organs with high metabolic rates and, therefore, susceptible to hypoxic injury [28,29]

Non-enzymatic production of H_2S can also occur in the body. One well established mechanism involves readily available polysulfides (H_2S_n) derived from nutrients, namely garlic and, mostly, relies on the presence of glutathione (GSH) and/or cysteine [30,31]. Other less common sources of H_2S include the reduction of thiosulfate (SSO_3^{-2}) by DHLA [32] from volatile organic polysulfides produced in the gut by resident bacteria, and H_2S itself from intestinal bacteria sulfur metabolism [33].

2.1.4. Hydrogen sulfide catabolism

H_2S can be highly toxic depending on its concentration, therefore the capacity of cells to oxidise it has to be far greater than its rate of production, maintaining intracellular levels very low [34]. Like the other gasotransmitters, H_2S has a high affinity for heme-containing proteins, hence the primary biochemical target associated with H_2S toxicity is cytochrome C oxidase (Complex IV), more specifically its α3 heme subunit [35]. Free H_2S concentrations in plasma normally range around 10-30 nM [34,36,37], matching observations where inhaled concentrations as low as 20ppm (a maximum of 6μM of free H_2S in tissues) were already able to elicit deleterious effects in mice. These

animals displayed a state that resembled suspended animation, where body temperature fell and marked decrease metabolic rate [38]. This was linked to a reversible binding of H_2S to cytochrome C oxidase.

H_2S oxidation occurs mainly in the mitochondria, and its major final product is sulfate (SO_4^{2-}), which accounts for around 90% of all urinary sulfur [39]. Even though H_2S can freely diffuse across membranes, the entirety of its catabolism occurs in the mitochondria [4041]. Organ wise, H_2S oxidation occurs throughout the whole body, but is specifically intense in the colonic mucosa, where bacterial contribution to H_2S is high, and in the aorta, where its concentration is especially high [4236], likely due to the role of H_2S in vasodilation. Four mitochondrial enzymes take part in the catabolism of H_2S: Sulfide:quinone oxidoreductase (SQR), sulfur dioxygenase (ETHE), thiosulfate sulfur transferase (TST or rhodonase), and sulfite oxidase (SO).

The inner mitochondrial membrane-bound SQR catalyses the first step in the H_2S oxidation pathway, forming a protein-bound persulfide with one of SQR cysteines (SQR-SSH) [43]. This process supports mitochondrial respiration by reducing flavine adenine nucleotide (FAD), which donates two electrons to ubiquinone [44]. In the bottom half of the mitochondria in **Figure 2** by the mitochondrial complexes, one can see that the sulfane sulfur in the protein-bound persulfide is picked up directly by GSH, which becomes then glutathione persulfide (GSSH) [45,46]. GSSH is further oxidised by ETHE, in the presence of oxygen, to generate sulfite (SO_3^{2-}), restoring one molecule of GSH in the process. At this point , SO_3^{2-} can: a) be further oxidised via SO to sulfate (SO_4^{2-}) [47] or b) become a thiosulfate (SSO_3^{2-}) with a sulfane group coming from GSSH via the sulfur transferase activity of TST [48,49]. Both reactions are labelled under “a” or “b” in the upper right portion of the mitochondria in **Figure 2**. It is important to note that SO activity also donates two electrons to the electron transport chain (ETC), but differently from SQR, it does so directly to cytochrome C (CytC) [50]. Both sulfate and thiosulfate are freely diffusible and are eliminated by the kidneys [43]. A representative scheme of the different reactions described above can be seen in **Figure 2.**

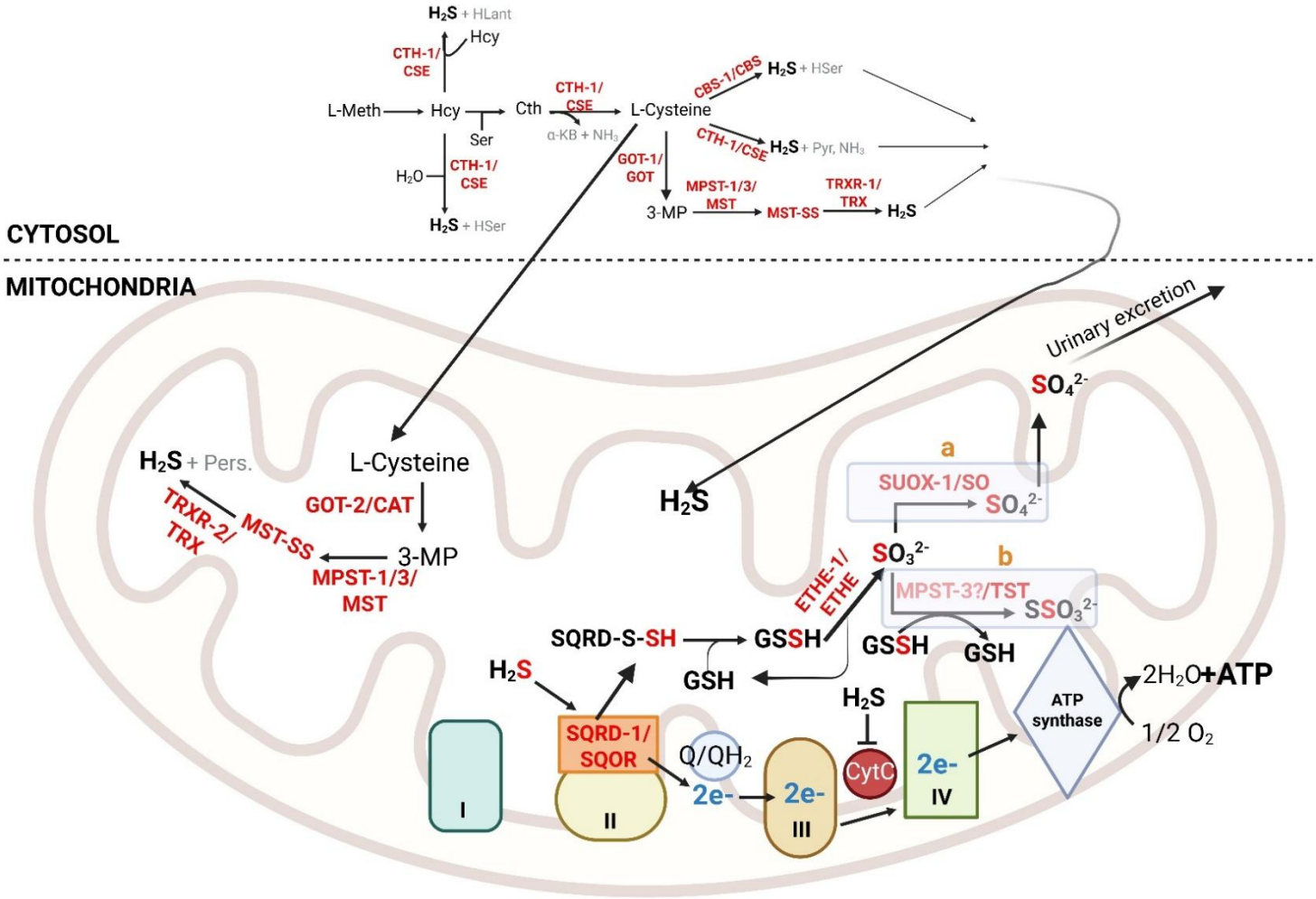

Figure 2. Mitochondrial H_2S catabolism via the sulfide oxidation pathway.

This figure depicts the mitochondrial enzymes and electron transport chain (ETC) components responsible for detoxifying and metabolizing H_2S, which is also produced in the cytosol via multiple enzymatic pathways and transported into mitochondria, as displayed on the upper half. Once inside mitochondria, H_2S is oxidized through the sulfide oxidation unit, beginning with SQRD-1/SQOR (sulfide:quinone oxidoreductase), which transfers electrons from H_2S to ubiquinone (Q), forming a persulfide-bound intermediate (SQRD-1/SQOR-SSH). These electrons reduce the ETC via complexes III and IV, contributing to ATP generation. The sulfane sulfur from the SQRD-1/SQOR-bound persulfide is then transferred to glutathione (GSH) to form glutathione persulfide (GSSH). GSSH is further processed by ETHE-1/ETHE1 (sulfur dioxygenase), which converts persulfide sulfur into sulfite (SO_3^{2-}). Highlighed in light blue, ‘’a” displays the first possible path for SO_3^{2-}, being subsequently oxidized by SUOX-1/SUOX (sulfite oxidase) to sulfate (SO_4^{2-}), which exits the mitochondria and is eventually excreted in the urine. Another possibility is highlighted in ‘’b’’, where TST (likely MPST-3 in *C. elegans*) (3-mercaptopyruvate sulfurtransferase) converts SO_3^{2-} into thiosulfate (SSO_3^{2-}), using the sulfane sulfur donated by a persulfide (likely GSSH).

continued on next page

Persulfide intermediates (such as MST bound persulfide, MST-SS) may be reduced back to H_2S by the action of the mitochondrial TRXR-2/TRX (thioredoxin reductase/thioredoxin system). Notably, excess H_2S can inhibit complex IV (cytochrome c oxidase). This figure was created in https://BioRender.com

Altogether, the balance between hydrogen sulfide production and its mitochondrial oxidation is critical for maintaining cellular homeostasis. While biosynthetic pathways ensure a steady supply of H_2S for signaling and metabolic regulation, the catabolic machinery — dominated by sulfide:quinone oxidoreductase (SQRD-1 in *C. elegans*, SQOR in mammals) — prevents its accumulation to toxic levels and channels sulfide-derived electrons into the respiratory chain [51]. Because SQRD-1 catalyzes the first and rate-limiting step of mitochondrial H_2S oxidation, its activity directly links sulfur metabolism to mitochondrial redox state, electron transport, and oxygen consumption. Perturbations of this system, such as those caused by hypoxia or loss of *vhl-1*, can shift the balance toward sulfide accumulation, amplifying its role as a signaling molecule that modulates HIF-1 activity and metabolic adaptation. This interplay between H_2S metabolism, SQRD-1 function, and hypoxia-related signaling forms a central theme of this thesis, guiding our investigation of how genetic perturbations and pharmacological interventions — notably the thiol drug Mesna — reshape mitochondrial metabolism, stress responses, and organismal physiology.

2.2. Sulfide:quinone oxidoreductase (SQR)

The sulfide:quinone oxidoreductase, also known as SQR or SQOR, is a mitochondrial membrane-bound flavoprotein that oxidizes H_2S to a protein-bound persulfide (SQR-SSH) [51]. This is the first and most critical step in the oxidation of H_2S. SQR couples H_2S oxidation to the reduction of coenzyme Q10 (CoQ), driving electron transport through the ETC, more precisely 2 protons are pumped across the inner mitochondrial membrane and two electrons are passed to the complex III via ubiquinone [52,53]. However, the ATP production derived from such reaction cannot support energy demand by itself when compared to the gradient the 10 and 8 protons NADH and

$FADH_2$ oxidation produce. [26]. The reaction catalysed by SQOR is represented in **Figure 2**.

SQR-SSH uses a mobile carrier (a low molecular weight acceptor) to transport the sulfane sulfur it has just acquired, and this is preferentially GSH, forming GSSH. In a series of steps sulfate and thiosulfate are formed and excreted, being the major (~17 mM) and second major (9µM) sulfur urinary sources, respectively [54–56]. SQR possesses remarkable substrate promiscuity (GSH, sulfite, and metanethiol) [57], and such promiscuity is also reflected on the mobile carrier it uses to transport the sulfane sulfur from its persulfide, these are currently proposed to be GSH or sulfite, leading to the formation of GSSH and thiosulfate, respectively.

Regarding sulfite, its importance as a mobile carrier for the sulfane sulfur in SQR-SSH is likely to be only of relevance under pathological conditions. That is because reported intracellular sulfite concentrations are low (20nM-4.6 µM) [5859] and below the K_M reported for SQR reaction with sulfite (260±30 µM) [46]. Elevated sulfite concentrations could arise from pathological conditions, such as SO deficiency [60], GSH depletion [61], or periodontitis with marked methanethiol increase [62], theoretically possible alterations in the active motif of SQR could become physiologically relevant. On the other hand, GSH is abundant in cells (1-10 mM) [63], and its $K_{M(GSH)}$ for the reaction with SQR is 8±1 mM [46], posting GSH as the dominant acceptor for the sulfane sulfur. The product of such reaction, GSSH, is an efficient substrate for SO (final excretable product is sulfate) and for TST (final excretable product is thiosulfate). Beyond that, the predominant form of GSSH is the persulfide anion (GSS^-), which is highly nucleophilic, facilitating perssulfidation of cysteines in proteins [64].

Two recent studies have shown that SQR/SQOR is indispensable for the survival after ischemia in both kidneys and brain of mice [65,66]. Both have reported that hypoxia induces H_2S accumulation that requires SQOR for its detoxification. When Sqor was excluded from the mitochondria in homozygosis, mice died at 10 weeks of age, highlighting the importance of H_2S oxidation in mammalian development [67]. In kidneys, those authors reported that SQOR inhibited ferroptosis mediated tubular cell death, an important mechanism contributing to ischemia-reperfusion damage in kidney [65]. Treatment with H_2S donors protected kidney from IRI in a Sqor-dependent mechanism

[65], evidencing its importance in mediating the activity of a potential new class of drugs in the treatment of IRI related damage in different organs.

2.3. Hydrogen sulfide in physiology and disease

For some time, H_2S oxidation was only considered physiologically relevant in the context of its elimination and prevention of toxic accumulation by SQR, as a modest antioxidant [68], or a potential driver of mitochondrial respiration at low oxygen concentrations [23,69]. However, nowadays it seems that its deepest effects are actually related to its capacity to inhibit cell death by different mechanisms [7071,72], and more recently, the capacity to promote S-persulfidation of cysteine residues of a growing amount of reported proteins [73]. Nowadays, it has been described to be of importance in the basic physiology and pathophysiology of the brain [74], heart [75], kidneys [76], intestines [77], immune system [78], and in the broader field of aging [79].

2.3.1. Hydrogen sulfide oxidation in the brain

Even though H_2S is abundant in several regions of the brain, including the striatum, cerebellum, and hippocampus [80], H_2S oxidation enzymes such as SQR, SO, ETHE, and TST are only expressed at very low levels in the brain of most mammals [81]. Namely, SQR levels are particularly low in the brain, pointing to a limited capacity of this organ to oxidise H_2S, this makes the brain particularly sensitive to H_2S accumulation and subsequent OXPHOS inhibition [82]. In fact, SQR levels in the brain inversely correlates to its sensitivity to oxygen deprivation, where low SQR levels hinder the brain more sensitive to hypoxia [82]. That stems from the heavy reliance of the brain on oxidative phosphorylation (OXPHOS) to supply its high demand for ATP [83]. While H_2S oxidation can stimulate OXPHOS via SQR, concentrations higher than 10μM are known to inhibit complex IV (cytochrome C oxidase) [84].

The duality of H_2S in the context of mitochondrial respiration is quite apparent in the brain, due to its marked sensitivity to hypoxia. On one side, it has been extensively shown that adequate concentrations of H_2S can protect the brain against IRI [85], and mechanisms such as preservation of mitochondrial function [86], prevention of apoptosis[87], and antioxidant activity [87] have been identified in rodent models. Conversely, ground squirrels, which are naturally resistant to hypoxia, become

sensitive to it after SQR silencing. The same study has shown that neuron-specific expression of SQR prevents ischemic brain injury in mice by counteracting toxic H_2S accumulation and bioenergetic failure [88]. Additionally, SO deficiency leads to a plethora of neurological abnormalities, such as neuronal necrosis, brain atrophy, and cognitive impairment [89,90].

Disturbed H_2S metabolism can also be found in genetic diseases, such as Molybdenum cofactor deficiency, SO deficiency, trisomy 21, Leigh syndrome-like disease, and ethylamonic encelopathy. Molybdenum cofactor deficiency and isolated sulfite oxidase deficiency both disrupt the terminal step of sulfur amino acid catabolism, where sulfite would normally be oxidized to sulfate by SO. In both conditions, sulfite accumulates and reacts with thiosulfate, perturbing H_2S detoxification and leading to elevated urinary thiosulfate levels. This disturbance of sulfur metabolism contributes to the severe neurological manifestations characteristic of these disorders [91]. In Trisomy 21, which results from three copies of the chromosome 21 (where the gene that encodes for CBS is located), it is hypothesised that CBS overexpression and H_2S buildup impair mitochondrial respiration, accounting for differences in brain development [92,93]. In the case of Leigh syndrome, 3 patients have been identified that had mutations in the gene encoding for SQR, potentially causing the reduced complex IV activity these patients displayed [94]. Additionally, the $Sqor^{\Delta N/\Delta N}$ mouse is a Leigh syndrome model, depicting hyperoxia and concurrent excessive ROS in the brain due to complex IV inhibition [95]. Finally, ethylamonic encephalopathy (a subtype of Leigh syndrome) is caused by ETHE deficiency [96], and patients have markedly diminished activity of complex IV and high excretion of ethylamonic acid due to sulfate accumulation [97]. In this case, the subsequent H_2S accumulation is primarily remediated by either sulfur-containing aminoacid restriction, or supplementation with GSH precursor N-acetylcysteine, facilitating SQR activity [98].

2.3.2. Hydrogen sulfide oxidation in the kidney

It is known for quite some time that kidneys produce fairly large amounts of H_2S [99,100]. While CSE is present in glomerular endothelial, mesangial cells, podocytes, proximal and distal tubules epithelial cells, and endothelial cells of capillaries [101], CBS is mostly detected in the epithelial cells of tubules [102]. 3-MST was also detected in epithelial cells of the proximal tubules [25], but considerably less studies have focused on it. In general

about 75% of all renal cells express at least one of these three H_2S producing enzymes, including 87% of all endothelial cells [101,102]. Indeed, reduced plasma levels of H_2S and/or reduced levels of its synthesizing enzymes can be correlated with the severity of some kidney diseases, such as tubulointerstitial fibrosis [103], diabetic nephropathy [104], and are found upon kidney failure [103].

An alternative, and considerably more efficient, pathway for H_2S production is present in the kidneys. It involves D-cysteine, instead of L-cysteine, and the synthesis of 3-MP from it by the action of D-aminoacid oxidase (DAO) in the peroxisomes. Peroxisomes and mitochondria often take part in metabolite exchange, allowing for mitochondrial 3-MST to produce H_2S from peroxisomal 3-MP [105]. Oral administration of D-cysteine can promote an increase in bound sulfane sulfur (H_2S-derived from protein bound sources). Glomerular structural disintegration induced by ischemia-reperfusion is prevented to a greater extent by D-cysteine when compared to L-cysteine treatment [106]. That is likely because the oxidised form of D-cysteine, D-cystine, which is abundant in the extracellular space has greater gastrointestinal absorption [107]. The presence of DAO is almost exclusive to kidneys (it is also present in the cerebellum), highlighting the physiological importance of H_2S there [106].

H_2S has been demonstrated to regulate glomerular filtration, which is represented by glomerular filtration rate (GFR), a clinically relevant index that describes renal clearance function in mice and cyclosporine in pigs [108,109]. More specifically, a $CBS^{+/-}$ mice with abnormally high levels of homocysteine which is a likely risk factor for chronic kidney disease progression, show reduced GFR that is restored after sodium hydrosulfide (NaHS) supplementation in the diet [109]. Conversely, pharmacological inhibition of CBS and/or CSE reduces GFR [110,111]. Infusion of NaHS into the renal artery results in an increased GFR and urine volume at concentrations that do not affect systemic blood pressure [112]. The same study verified that pharmacological inhibition of CSE and CBS reduces GFR, indicating a role for endogenously produced H_2S. Additionally, chronic kidney disease (CKD) patients display decreased expression of CBS and CSE in blood mononuclear cells, but higher 3-MST [113]. Among the possible molecular mechanisms behind such effects, vasodilation via activation of the widely described vasodilator NO/cGMP pathway is a possibility [114].

H_2S in the kidney is also an important mediator of the effects low oxygen has over cell function and metabolism. It has been shown that for an adequate hypoxia response to take place, H_2S is required [115]. Acute kidney injury (AKI), an increasingly common condition in hospitalised patients that often leads to CKD and comes with considerable morbidity and mortality[116], is often caused by hypoperfusion, leading to variable degrees of local hypoxia as well as ischemia-reperfusion in the kidneys [117]. The potential role of H_2S and sulfide-based therapies has been extensively investigated in the context of IRI in the brain and also in the kidneys [118]. Like in several other renal disorders, H_2S is, in general, decreased after IRI [119]. Treatment with different donors has been shown to improve IRI outcomes by reducing oxidative stress [120] and restoring mitochondrial function [121]. A recent meta-analysis that spanned over 20 studies, has shown that H_2S donors have to be given during or before IRI to be effective, and that the mode in which they release H_2S has to be slow [118]. Finally, most studies have consistently found that these pharmacological interventions act via the inhibition of oxidative stress by preventing mitochondrial ROS formation [118]. In conclusion, understanding the molecular mechanisms through which H_2S or molecules that are able to produce H_2S mediate protection are of great relevance to human disease with specific implications for AKI.

2.3.3. Hydrogen sulfide and hypoxia pathway interaction

Hypoxia and H_2S are deeply interconnected in both physiology and pathogenesis, converging on pathways that regulate tissue adaptation and injury. For example, in the kidney, an organ characterized by steep oxygen gradients, endogenously produced H_2S functions as an oxygen sensor and regulator of excretory processes. That includes modulation of renin release and sodium transport in tubular cells [122]. Under hypoxic stress and during ischemia–reperfusion injury (IRI), H_2S metabolism is disrupted. Ischemia acutely increases renal H_2S levels and the expression of its biosynthetic enzymes, while reperfusion provides only partial recovery [123]. This transient surge may help restore oxygen O_2 supply by increasing medullary blood flow and inhibiting of tubular transport [124]. However, prolonged hypoxia leads to continued accumulation of H_2S, which aggravates mitochondrial dysfunction, oxidative stress, inflammation, and regulated cell death pathways such as apoptosis and ferroptosis [122], key drivers of IRI-induced acute kidney injury (AKI) [125].

Therapeutically, restoring H_2S signalling has shown significant renoprotective effects in preclinical models. Administration of H_2S donors (e.g., NaHS, GYY4137) attenuates renal IRI by mitigating oxidative stress, suppressing inflammatory mediators (including NF-κB, ICAM-1, NLRP3 inflammasome), stabilizing mitochondria, enhancing autophagy, and reducing apoptosis and tubular damage [126]. Additionally, H_2S accelerates tubular recovery post-IRI and improves renal perfusion and function [126]

Taken together, these findings place the H_2S–hypoxia axis at the core of IRI-mediated kidney injury, highlighting not only its mechanistic relevance but also its potential as a therapeutic target. H_2S emerges not only as a biomarker for hypoxic distress, but as a modulator of redox homeostasis, inflammatory signalling, and cell survival pathways, making it a promising candidate for interventions to prevent or ameliorate ischemic renal damage.

2.4. Hydrogen sulfide donors

H_2S donors are molecules able to trigger release of H_2S in response to an enzymatic or non-enzymatic stimulus. The development of such molecules comes from the need to study and understand H_2S related processes in physiology and disease, where often H_2S concentrations are too low to be properly analysed. Moreover, the application of H_2S as a therapeutic agent is also greatly limited by its volatility and potential toxicity at high concentrations. By delivering exogenous H_2S into biological systems, researchers were able to better understand the biological role of this gasotransmitter, but also use it as a potential therapeutic in several disease models [1]. The most commonly used H_2S donors were originally sulfide salts such as sodium hydrosulfide (NaHS) and sodium sulfide (Na_2S) [1], along with naturally occurring compounds like the garlic-derived allicin metabolites diallyl sulfide (DAS), diallyl disulfide (DADS), and diallyl trisulfide (DATS) [127]. More recently, synthetic donors such as GYY4137 have gained increasing attention [128].

Sulfide salts like NaHS were among the first ones to be employed to study the vasorelaxant effects of H_2S [129]. However, sulfide salts rapidly establish an acid–base equilibrium in aqueous solution, where only a small fraction remains as free H_2S.

Because H_2S is volatile, it readily escapes from solution, resulting in a rapid decline in its concentration [15]. Overall, the high speed at which H_2S is delivered by such molecules makes the effect challenging to reproduce, impossible to target, and creates the need for successive administrations. This led to the search for alternative donors, such as naturally occurring ones. A group of naturally occurring donors is the one derived from Allicin, an abundant chemical in garlic, which decomposes into DAS, DADS, and DATS. In biological systems, these three chemicals release H_2S in the presence of free thiols, such as GSH due to its high intracellular availability, but also cysteine, and homocysteine [31]. Finally, synthetic donors come with the opportunity to chemically manipulate molecules so that, e. g. the rate at which H_2S is released becomes controllable. The most prominent example of this class of donors is the slow H_2S releasing GYY4137. Even though this molecule releases much less H_2S than NaHS, it reaches maximum H_2S concentration much later, which means is able to maintain H_2S levels in cell culture for over 7 days [130].

2.4.1. Hydrogen sulfide donors in disease models

In vivo models have shown that H_2S donors can exert a range of biological activities, such as protection against IRI in different organs, anti-inflammatory effect, vasodilation and pressure-lowering effects, neurotrauma, and anti-atherosclerosis [131,132]. More specifically, NaHS and H_2S precursor L-cysteine can modulate tubular function in the kidney, and increase GFR via its vasorelaxing effect, two actions that can help prevent damage in different nephrotoxicity models [111,110,133]. Na_2S was among the first H_2S donors shown to mediate protection in a hepatic IRI model by inhibiting ROS-associated damage and restoring GSH balance [134].

A particularly insightful study has recently shown that NaHS is able to alleviate cardiac damage in diabetic cardiomyopathy by activating the Nrf2/GPx4/GSH pathway, suppressing ferroptosis and mitigating apoptosis. This is in accordance with previous studies that had already shown that H_2S can activate Nrf2 by persulfidating its canonical inhibitor Keap1, specifically at the residue Cys151. This prevents Nrf2 degradation and enhances its nuclear translocation and the resulting transcriptional activation [135]. In fact, Nrf2 has been shown to mediate the effects of NaHS in acute liver injury [136], IRI in gastric epithelial cells [137], and kidney injury induced by high salt diet [138] but also the effects of GYY4137 over liver injury induced by streptozotocin [139].

In fact, a large part of the studies employing H_2S donors are dedicated to study its efficacy in IRI models in different organs, namely kidneys, brain, and heart [118,126,140,141]. In AKI, H_2S can prevent mitochondrial dysfunction caused by hypoxia: It sustains ATP production and protects from free radicals accumulation, two commonly deregulated endpoints in mitochondrial dysfunction accompanying AKI [142]. AP39, another synthetic H_2S donor with a slow release profile that targets specifically the mitochondria, can inhibit mitochondrial ROS formation and prevent IRI in both brain and kidney [121143].

Regarding the naturally occurring donors, DAS and DATS are the most potent donors in this class, having a much faster releasing profile than DADS [144]. A number of studies have shown how such potent H_2S production can be exploited in chemotherapy, where DATS is preferentially toxic towards colon, gastric, brain, and breast cancerous cells [145]. A study in *C. elegans* delved into the mechanisms by which DATS could increase the lifespan of these animals, showing a mechanism dependent on *skn-1*/Nrf2 and the induction of important aging and detoxification-related targets such as *gst-4* [146]. Recently, two independent studies found that the naturally occurring H_2S donor ergothioneine is able to promote healthspan and lifespan in different organisms, including mice and worms, via persulfidation of metabolic enzymes in the mitochondria [147,148]. However, while one study found ergothioneine to produce H_2S by serving as a substrate for CSE and boosting NAD+ via cGDPH persulfidation [147], the other has identified MPST to be a direct target that induces H_2S production and improves mitochondrial metabolism [148].

2.4.2. Hydrogen sulfide donors in aging

A number of studies have placed H_2S as a regulator of aging and healthspan across different species. In *C. elegans*, it was shown that exogenous H_2S exposure significantly extends lifespan and enhances thermotolerance by up to ~70%, an effect that is independent of the insulin, mitochondrial, or dietary restriction pathways [149], all well-established lifespan extending interventions. Another study using the slow-releasing donor GYY4137 found lifespan extension (~17–23%) and increased resistance to oxidative and ER stress, effects that depended on the sulfhydrylase *cysl-2* [150], underscoring a role for endogenous H_2S metabolism in longevity. Further, a mitochondria-targeted H_2S donor, AP39 (mtH_2S), prolonged both lifespan and neuromuscular health in worms at nanomolar doses [151]. This conserved role extends

to mammals: endogenous H_2S production declines with age [152] and may underlie the benefits of caloric restriction and mitohormesis through preservation of mitochondrial quality and redox balance [153]. Experimental models further demonstrated that mitochondrial-targeted H_2S donors attenuate endothelial senescence by modulating splicing factors (e.g., SRSF2, HNRNPD) and reducing senescent cell burden—suggesting translational potential in mammalian aging interventions [154,155].

Despite the remarkable therapeutic potential demonstrated by existing H_2S donors across aging, ischemia–reperfusion injury, and oxidative stress models, their clinical translation remains limited by issues of stability, release kinetics, tissue targeting, and safety. This gap underscores the need to identify new modulators of sulfide metabolism, ideally among compounds with an already established safety profile. Drug repurposing offers a powerful and time-efficient strategy to achieve this. In this context, the clinically approved thiol drug Mesna emerges as a promising candidate, whose capacity to modulate redox balance and potentially influence sulfide-related pathways has not yet been fully explored.

2.5. Mesna

Building on the therapeutic promise of sulfide modulation and the current limitations of available H_2S donors, we explored whether the clinically approved thiol compound Mesna could serve as an alternative modulator of sulfide metabolism. Mesna's well-established safety profile, combined with its capacity to interact with thiol and redox systems, makes it an attractive candidate for repurposing as a sulfide-modulating agent.

2-mercaptoethanosulfonic acid, also known as Mesna or Coenzyme M (CoM), is an FDA-approved prophylactic medication used to reduce the incidence of hemorrhagic cystitis in patients receiving chemotherapy with high-dose cyclophosphamide or ifosfamide [156]. Its chemical structure is represented in Figure 3. Mesna is rapidly oxidized in plasma through metal-catalyzed reactions, forming disulfide dimers with itself (dimesna) or with other small thiols such as cysteine and homocysteine. Cysteine and homocysteine depletion have been reported following Mesna administration, a

property that has proven useful in a high-fat diet–induced obesity model [157] and also in homocystinuria [158]. Interestingly, Mesna appears to spare glutathione (GSH) [159], a counterintuitive feature given their structural similarity. This property is particularly relevant because GSH depletion is frequently associated with pathological conditions [160] suggesting that Mesna could modulate redox balance without compromising this critical antioxidant.

It is also worth noting that Mesna/CoM naturally occurs as a cofactor in methanogenic archaea and a small number of bacteria capable of more complex metabolism [161]. Curiously, a recent study describing alternative biosynthetic pathways for Mesna/CoM in bacteria suggests that the salient features of the pathway involve reactivities characteristic of the large family of PLP-dependent enzymes, which includes CBS and CSE [162]. Together, these observations point to Mesna as a chemically and biologically relevant thiol with unexplored potential in sulfide metabolism. In the following sections, we investigate whether Mesna can modulate H_2S homeostasis, stress resistance, and mitochondrial function in *C. elegans* and mammalian kidney cells, and assess its potential as a repurposed therapeutic agent.

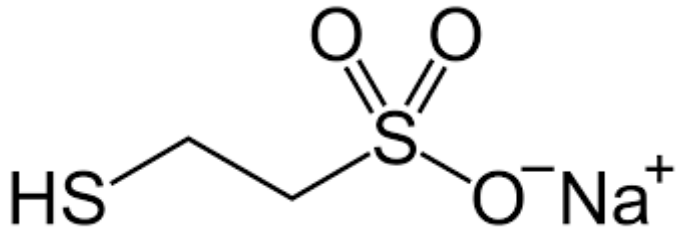

Figure 3. Chemical structure of Mesna (Sodium 2-mercaptoethanesulfonate).

Mesna has several off label uses, all either related to cyclophosphamide or a number of etiologically heterogeneous cholesteatoma [163–166]. On the other hand, since 2010, a large number of studies have been relating the potential usefulness of Mesna in a considerable number of disease models, specially IRI in different organs such as liver [167,168], heart [169], lungs [170], gastric mucosa [171], spinal cord [172], and especially kidneys [173–176]. A large part of this studies has attributed the protective effect of Mesna to its

antioxidant capacity, even though no direct scavenging ability or direct interaction with master regulators of cellular antioxidant response could be shown. Instead, these studies have generally observed reduced ROS and ROS-associated markers [174], such as lipid peroxidation products, key antioxidant enzymes such as GPX4 [173] and GSH restoration [175]. Indeed, a systematic review has identified Mesna as being able to completely prevent oxidative stress markers to sham levels in minimally invasive surgery, being the only out of 7 drugs tested [177].

It is worth noting that, even though it was known for quite a while that Mesna could deplete small thiols, GSH and/or GSH-dependent enzymes restoration is consistently found in kidney [178], brain [174], and heart [169] models of AKI. Additionally, Mesna is often found in heterogeneous mixtures of disulfides with cysteine, reduced GSH, homocysteine, and γ-glutamylcysteine [179], suggesting that this naturally occurring small thiol might impact H_2S metabolism, which itself has been shown to be a key regulator of the molecular pathophysiology of IRI in different organs [126]. Considering that Mesna is already an approved medication, combined with preclinical evidence supporting its potential in IRI models, its impact on sulfide metabolism, and the established protective effects of sulfide in various IRI contexts, we propose that Mesna could prevent IRI by modulating sulfide and/or thiol levels. In this thesis, we address this hypothesis by combining genetic and pharmacological approaches in *C. elegans* and mammalian systems to assess how Mesna influences sulfide metabolism, thiol homeostasis, and downstream molecular pathways under stress, evaluating both protective phenotypes and mechanistic changes at the metabolic and proteomic levels.

2.6. The hypoxia pathway in physiology and disease

2.6.1. Hypoxia definition and pathophysiological relevance

Hypoxia is defined as a state of low oxygen concentration in body tissues, which translates into cellular dysfunction primarily associated with inhibited mitochondrial respiration and an impaired capacity to produce ATP, ultimately leading to cell death and organ damage [180]. It can arise from distinct factors, such as exposure to low oxygen environments, underlying disease conditions, or intrinsic cellular dysfunction.

Complex organisms have evolved mechanisms not only to ensure adequate oxygen delivery to cells and tissues but also to respond and adapt to hypoxia once it occurs. These adaptive responses can involve enhancing oxygen delivery or promoting cellular survival in a hypoxic environment [181].

Physiological hypoxia occurs in a variety of contexts, including during embryonic development, within the mucosa of the gastrointestinal tract, in skeletal muscle during exercise, and as a stable oxygen gradient between the renal medulla and cortex [182]. Moreover, controlled and transient episodes of hypoxia can serve as preconditioning stimuli that improve stress resistance and clinical outcomes in a number of pathological settings [183].

By contrast, pathophysiological hypoxia is a hallmark of many disease states, such as chronic inflammation associated with autoimmune diseases, a broad range of tumours, and virtually all ischemic conditions, including myocardial infarction, stroke, and ischemic kidney injury [182]. In the kidney specifically, hypoxia is both a cause and a consequence of acute kidney injury (AKI) [184] and contributes to increased susceptibility to renal damage as well as to the progression of chronic kidney disease (CKD) [185].

Because hypoxia is such a fundamental physiological and pathological stress, organisms have evolved conserved molecular mechanisms to sense and adapt to oxygen limitation. Central among these is the hypoxia-inducible factor (HIF) pathway, which reprograms mitochondrial metabolism and interfaces with sulfide signaling to promote cellular survival — mechanisms discussed in detail in the following sections.

2.6.2. Molecular basis of the adaptation to hypoxia

The molecular response to hypoxia is coordinated by a group of transcription factors called hypoxia-inducible factors (HIF). HIF proteins are heterodimers consisting of a stable HIFβ and an unstable HIFα subunit. In humans, there are three main HIFα proteins: HIF-1α and HIF-2α, which display classical functions, and HIF-3α, which is inhibitory [180,186]. At normal oxygen levels (normoxia), the α subunit of HIF proteins are hydroxylated by prolyl hydroxylases (PHDs) at specific proline residues, which allows for its interaction with the von Hippel-Lindau tumour suppressor (pVHL) [187,188], which can be seen on the left side of **Figure 4**. pVHL then serves as a recognition substrate to an E3 ubiquitin ligase, promoting HIF1α polyubiquitination and proteosomal

degradation. Since PHD activity is dependent on the presence of oxygen, they are responsible for “sensing” low oxygen levels [189]. Therefore, hypoxia induces HIF1α accumulation and nuclear localisation by, primarily, inhibiting PHDs activity, which in turn prevents pVHL binding and ubiquitination-mediated proteosomal degradation, which is shown on the right panel of **Figure 4**. In the nucleus, HIF1α dimerises with stable HIF1β and binds to so called hypoxia response elements (HRE), where it can activate the transcription of over one thousand genes [190,191] that are essential to survival under hypoxic conditions, such as those related to cell survival, angiogenesis, glycolysis, mitochondrial function, and cell growth and survival [192], displayed at the bottom corner of the right panel of **Figure 4**.

Even though HIF1α stabilisation is the major driver of adaptation to hypoxic conditions, transcriptional regulation is preceded by mitochondrial changes: the ratio NADH/NAD+ increases [193], ROS and ROS-dependent signalling goes up [194], mitochondrial membrane potential goes down together with ATP, ultimately leading to AMPK activation and a drop in overall respiration. While under normoxic conditions the vast majority of ATP is produced by oxidative phosphorylation (OXPHOS) in the mitochondria, under hypoxic conditions, HIF1 activation and transcriptional regulation shift cells from aerobic to anaerobic metabolism. For that, it drives the transcription of glycolysis related genes, such as glucose transporters SLC2A1 (GLUT1) and SLC2A3 (GLUT3), while mitochondrial pyruvate dehydrogenase (PDH) is downregulated due to overexpression of pyruvate dehydrogenase kinase (PDK1) [195,196]. Moreover, all glycolytic enzymes also get upregulated, including aldolases, enolases, and hexokinases [182], but also lactate dehydrogenase (LDHA), which prevents pyruvate from entering the citric acid cycle (TCA) by converting it into lactate [197]. This switch from oxidative to glycolytic metabolism not only ensures efficient ATP production, but it also leads to reduced mitochondrial production of ROS and ROS-associated damage [198].

Oxidative phosphorylation is reduced by HIF1 activation via a series of different target genes, and that ends up reducing the total amount of oxygen consumed in the cell. The expression of different mitochondrial complexes is altered, for example, cytochrome C oxidase (complex IV) subunits are differentially expressed, promoting overall lower oxygen consumption by the electron transport chain (ETC) [199]. The total

pool of Coenzyme Q (ubiquinone, oxidized; ubiquinol, reduced), which is a key redox carrier in the mitochondrial electron transport chain, is critical for survival under hypoxia [200]. The ratio between its reduced and oxidized forms is also an important redox sensor, coupling electron passage between the different complexes to their assembly and function [201]. Finally, mitochondrial biogenesis is reduced while mitophagy is promoted [199,202]. A graphical representation of the described hypoxia-mediated modifications to the metabolism of the cell is shown in **Figure 4**.

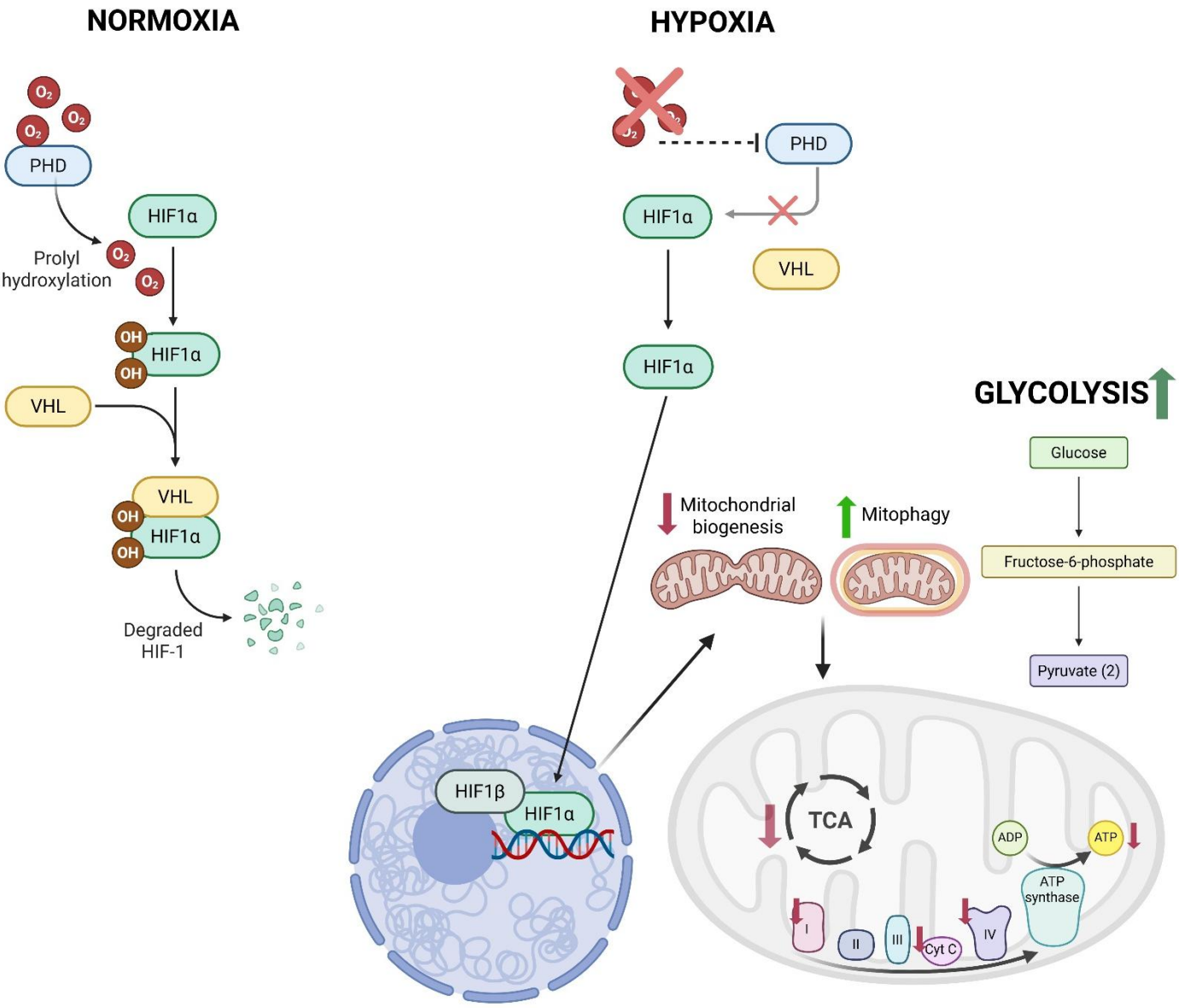

Figure 4. Oxygen availability regulates HIF-1α stability and drives metabolic reprogramming under hypoxia.

Under normoxic conditions (~21% O_2, left panel), prolyl hydroxylase domain enzymes (PHDs) hydroxylate specific proline residues on hypoxia-inducible factor 1α (HIF-1α), creating a recognition site for the von Hippel–Lindau (pVHL) E3 ubiquitin ligase complex.

continued on next page

This leads to polyubiquitination and subsequent proteasomal degradation of HIF-1α, thereby preventing activation of the hypoxic transcriptional program. Under hypoxic conditions (<5% O_2, right panel), PHD activity is inhibited due to limited oxygen availability, preventing HIF-1α hydroxylation and recognition by pVHL

Stabilized HIF-1α accumulates in the cytoplasm, translocates to the nucleus, and dimerizes with HIF-1β to form the active HIF-1 transcription factor complex. This complex binds to hypoxia-responsive elements (HREs) in the promoters of target genes, driving a broad transcriptional program that enhances cellular adaptation and survival. Key downstream effects include increased transcription of glycolytic enzymes and glucose transporters to sustain ATP production under low oxygen, and a coordinated downregulation of tricarboxylic acid (TCA) cycle enzymes and oxidative phosphorylation (OXPHOS) components, reducing mitochondrial oxygen consumption. Additionally, HIF-1 signaling decreases mitochondrial biogenesis while promoting mitophagy, thereby limiting reactive oxygen species (ROS) generation and preserving mitochondrial quality under hypoxic stress. This figure was created in https://BioRender.com

2.6.3. The hypoxia pathway and aging

Recently, a number of studies have shown that hypoxia can accelerate aging and metabolic diseases [203]. Factors such as reactive oxygen species (ROS) and chronic inflammatory mediators, which are linked to the hallmarks of aging, can lead to HIF-1 accumulation even under normoxic conditions. Aging is also characterized by reduced tissue oxygenation, for example due to impaired vascularization [204]. HIF-1 activity itself has been linked to aging too: it can promote longevity through metabolic reprogramming and stress resistance, but in other contexts, chronic HIF activation may contribute to age-associated pathologies such as cancer or fibrosis [205]. The pathway also interacts with nutrient-sensing and mitochondrial stress pathways, which are deeply implicated in the regulation of lifespan. For example, ROS can influence *HIF1α* gene expression, while it is also is a key player in the development of aging and aging-associated diseases. Conversely, through HIF1α stabilization and activation, mitochondrial function declines, and with it energy production, as well as ROS accumulation, and ROS-associated damage also decreases, delaying aging [206].

Activation of HIF1 has been shown to extend lifespan in several organisms. In *C. elegans*, stabilization of HIF1α/HIF-1 through genetic mutations (e.g., in *vhl-1* or *egl-9*)

or environmental conditions promotes longevity by enhancing stress resistance and metabolic adaptation [207]. In Drosophila melanogaster, hypoxia exposure or HIF/Sima/Tango pathway activation can also improve survival and slow aging under certain conditions, such as caloric restriction [208]. In mammals, while chronic HIF1 activation is often linked to disease, moderate or tissue-specific activation—such as in the liver or adipose tissue—has been associated with metabolic benefits and potential lifespan extension in mice, particularly in contexts like caloric restriction or intermittent hypoxia [209203]. The long-lived and highly hypoxia-tolerant naked mole rat (*Heterocephalus glaber*) displays high level of ROS and impaired pVHL binding to HIF1, allowing for constitutive activation even under normoxic conditions [210]. These findings suggest that the longevity effects of HIF-1 activation are dose-, tissue-, and context-dependent, but evolutionarily conserved across species. Further studies that shed light on the relationship between aging and HIF1 activation are needed, as well as providing evidence as to whether different HIF1 activating factors (e.g. different mutations) might activate the expression of different genes, allowing for cellular outcomes similar to those seen in preconditioning, potentially improving stress resistance and other aging associated phenotypes.

2.7. *C. elegans* as a model organism

Caenorhabditis elegans is a genetically tractable and experimentally accessible model organism that has contributed significantly to our understanding of developmental biology, neurobiology, and aging [211,212]. It is a small (~1 mm), free-living nematode that is transparent throughout its life, allowing for live imaging of cells and tissues using differential interference contrast (DIC) or fluorescence microscopy [213]. The organism has an invariant and fully mapped cell lineage of exactly 959 somatic cells in the adult hermaphrodite, making it particularly powerful for developmental studies [214]. Its life cycle is rapid and temperature-dependent, lasting approximately 3 days at 20°C. Development proceeds from the embryo through four larval stages (L1 to L4) to adulthood. After hatching, the organism begins life as a first-stage larva (L1), which molts sequentially through the L2, L3, and L4 stages before undergoing a final molt to reach the adult form. Each molt involves the synthesis and shedding of a new cuticle—a collagen-rich extracellular matrix that is essential for body shape, barrier function,

and growth. Proper molting requires tightly regulated expression of stage-specific cuticular collagen genes and enzymes responsible for collagen modification, such as prolyl and lysyl hydroxylases [215], as well as redox and metabolic support for disulfide bond formation and cross-linking [216]. Under adverse conditions such as starvation or overcrowding, L1 larvae may enter an alternative developmental stage called dauer, a stress-resistant, non-feeding, and long-lived form that allows survival until conditions improve [217] . The hermaphroditic reproductive system enables both self-fertilization and controlled outcrossing with males, simplifying genetic analysis while maintaining flexibility [218]. Furthermore, the complete genome of *C. elegans* has been sequenced and shares a high degree of conservation with human genes, including those involved in metabolism, signaling, and disease [219,220], establishing it as an ideal in vivo model for studying fundamental biological processes.

2.7.1 The hypoxia pathway in *C. elegans*

The nematode *C. elegans* offers a good model to study the underlying mechanisms of hypoxia adaptation. Its usefulness in this specific research topic comes from the fact that it possesses a single HIFα homologous (HIF-1), a single pVHL homologous (VHL-1), as well as a single PHD homologous (EGL-9), all of which when knocked out yield viable animals [221222], although unable to adapt to hypoxia (0,5%-1% O_2) [222]. In fact, the first prolyl hydroxylase (EGL-9) described to integrate oxygen sensing and HIF1/HIF-1 activation came from a study in *C. elegans* [221]. This genetic tractability has helped to identify the conserved mechanism by which HIF-1 is activated under hypoxia, where low oxygen availability prevents EGL-9 mediated hydroxylation of HIF-1 and VHL-1 mediated ubiquitination. HIF-1 can be activated in response to hypoxia, which these nematodes experience often in their natural habitat. HIF-1 can be also activated in response to toxic chemicals (e.g. heavy metals, selenium, hydrogen peroxide, and H_2S), pathogens, thermal stress and related proteotoxicity. All of these scenarios can induce extended lifespan that can range from 30-50% depending on the specific inducer and exposure time [207,223,224]. Similar to mammals, genes regulated by HIF-1 activation in *C. elegans* are involved in stress resistance, innate immunity, proteostasis, mitochondrial metabolism, glycolysis, and H_2S metabolism [225226].

Both deletion of the *vhl-1* and *egl-9* genes, which encode the *C. elegans* homologues of the von Hippel–Lindau protein and the prolyl hydroxylase EGL-9, respectively,

extend the lifespan of *C. elegans*. In *vhl-1(ok161)* mutants, this lifespan extension is entirely dependent on *hif-1*, the gene encoding HIF-1α [223]. Similarly, *egl-9(sa307)* mutants also display a *hif-1*-dependent increase in lifespan [227]. However, the consequences of *vhl-1* and *egl-9* deletion are not equivalent, highlighting that the mode of HIF-1 activation strongly influences physiological and molecular outcomes. While *vhl-1* deletion leads to generalized and prolonged stabilization of HIF-1, resulting in a broader activation of hypoxia-responsive genes [228], *egl-9* deletion prevents hydroxylation of HIF-1 but leaves VHL-1 functional, meaning that any HIF-1 that becomes hydroxylated through EGL-9–independent or alternative oxygen-sensitive mechanisms can still be degraded [229,207,230,231]. This difference may underlie the fact that *vhl-1* deletion extends lifespan across a range of culturing conditions, whereas *egl-9* deletion does so only under specific temperatures [232], and can extend lifespan independently of *vhl-1* [229,207,230,231]. Moreover, genome-wide analyses show that although hundreds of genes are commonly activated in both mutants, 20–30% of HIF-1 targets are uniquely regulated depending on whether HIF-1 activation is triggered by *egl-9* or *vhl-1* mutation [228], further illustrating distinct transcriptional programs downstream of each mutation. Notably, a shortened body size at developmental stages and adulthood has been consistently observed in *vhl-1(ok161)* mutants and in *vhl-1* knockdown animals [233], a phenotype that has not been reported for *egl-9* mutants, reinforcing the idea that different forms of HIF-1 activation produce distinct organismal outcomes.

HIF-1 accumulation and the promotion of the transcription of its targets occurs not only in hypoxia but it is also regulated by excessive ROS, inflammation markers, and H_2S [234,235]. H_2S has attracted considerable interest in recent literature [236,237], in part because it can be administered through diverse donor compounds and delivery system [126,238]. Perhaps the most well studied animal model regarding the interaction between HIF1 and H_2S is *C. elegans*, in which H_2S and HIF-1 are part of a tightly regulated adaptive pathway to low-oxygen and sulfide-rich environments. H_2S stabilizes HIF-1 by inhibiting EGL-9 with the help of the sulfide-sensing protein CYSL-1 [239], as displayed on the right side of **Figure 5**. In turn, HIF-1 activates expression of genes like *sqrd-1*, which detoxify H_2S [240], establishing a feedback loop where H_2S promotes HIF-1 activity (**Figure 5**, textbox 1 and 2), and HIF-1 helps reduce H_2S levels via overexpression of SQRD-1 (**Figure 5**, textbox 3), bringing HIF-1 activation back down via CYSL-1

(**Figure 5**, textbox 4). This coordination supports cellular survival under hypoxia and H_2S stress [240,241]. A graphical representation of these interactions is displayed in

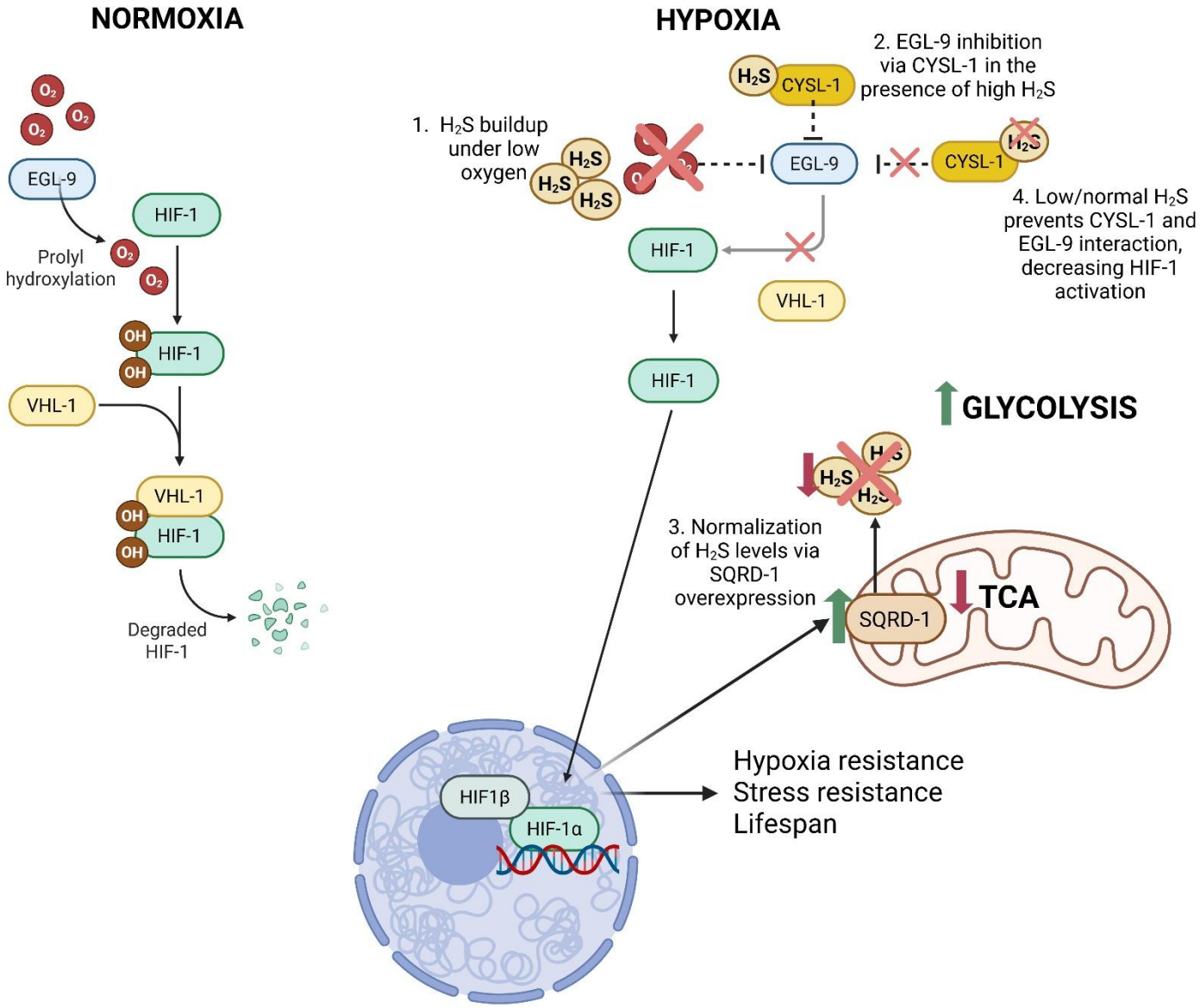

Figure 5.

Figure 5. Regulation of HIF-1 activation by H_2S metabolism via SQRD-1 during hypoxia in *C. elegans*.

Under hypoxic conditions (<1% O_2 for *C. elegans*), oxygen scarcity inhibits the prolyl hydroxylase EGL-9, preventing HIF-1 hydroxylation and subsequent degradation by the VHL-1 ubiquitin ligase complex. As a result, HIF-1 accumulates, translocates to the nucleus, and activates a transcriptional program that enhances hypoxia resistance, stress resilience, and lifespan. Oxygen limitation also impacts sulfide metabolism, introducing additional regulatory layers to HIF-1 control. (1) Low oxygen reduces the activity of mitochondrial sulfide-oxidizing enzymes, causing H_2S to accumulate. (2) Elevated H_2S levels inhibit EGL-9 through the sulfide sensor CYSL-1, further stabilizing HIF-1. (3) Prolonged HIF-1 activation

induces the expression of the mitochondrial sulfide:quinone oxidoreductase SQRD-1, which metabolizes excess H_2S and restores its physiological levels.

continued on next page

(4) Once H_2S concentrations normalize, CYSL-1 no longer inhibits EGL-9, leading to reduced HIF-1 stabilization and re-establishing regulatory balance. Through this feedback mechanism, sulfide metabolism integrates with oxygen sensing to fine-tune HIF-1 activity and metabolic reprogramming, characterized by increased glycolysis and reduced tricarboxylic acid (TCA) cycle activity and mitochondrial respiration.

2.8. Hydrogen sulfide and the hypoxia pathway interaction in *C. elegans*

H_2S metabolism is crucial for the nematode *C. elegans*. These nematodes are often exposed to low oxygen environments in their natural habitat, and under hypoxic conditions H_2S builds up due to its oxygen-dependent oxidation. This leads to further activation of HIF-1 orchestrated adaptive responses, where several sulfide-metabolism related enzymes are upregulated [242239]. Interestingly, the occurrence of life in natural environments that are low in oxygen and rich in sulfide, such as hot springs, swamps, and deep sea hydrothermal vents [243] illustrates how important SQR/SQRD-1 enzymatic function might have been: in primitive earth atmosphere ATP synthesis was likely dependent on H_2S oxidation at some level [13].

The multiple pathways that generate H_2S from cysteine and its derivatives serve not only as alternative routes for ATP production under hypoxic conditions, but also as signaling mediators that convey information about mitochondrial oxygen availability and energy status to the cytoplasmic HIF-1 pathway. Beyond its own metabolism, H_2S signaling can proceed through the formation of persulfides, which have been shown to modulate cellular energetics by targeting mitochondrial metabolic enzymes oxidized[147,244].

In more detail, exogenous H_2S leads to HIF-1 translocation to the nucleus in *C. elegans*, however that effect seems to be specific to the hypodermis, and independent from *vhl-1*, whereas activation in the intestine, a major organ in these nematodes, only occurs under actual hypoxia [240] or in specific mutants that lead to HIF-1 stabilisation.

Key genes in the H_2S oxidation pathway are HIF-1 targets in *C. elegans* and indeed, *hif-1* is indispensable for survival of *C. elegans* exposed to toxic H_2S levels [240]. It is believed that H_2S induces HIF-1 activation by promoting the physical interaction of CYSL-1 and the prolyl hydroxylase EGL-9, thus preventing HIF-1 hydroxylation, leading to its nuclear translocation and transcriptional activation of target genes [239].

Targets of the master cytoprotective transcription factor Nrf2/*skn-1,* such as *rhy-1,* can bypass HIF-1 to promote adaptation to elevated H_2S [229]. RHY-1 can activate CYSL-1, which not only can induce HIF-1 activation, but could, hypothetically, detoxify H_2S by producing cysteine from it [240]. Surprisingly, overexpression of RHY-1 can bypass the need for *sqrd-1* (key and limiting step to the only known pathway to metabolise H_2S in vivo) to survive in H_2S [229], suggesting that the mitochondrial pathway to metabolise H_2S is not absolutely necessary. Consistent with that, *egl-9* knockdown can also partially rescue H_2S toxicity via HIF-1 activation [245]. Indeed, H_2S-induced SKN-1 activation leads to the transcription of targets that are not only critical for survival, but are neither identical to those in classical SKN-1 activation under stress [246], nor identical to those induced by HIF-1 after H_2S exposure. This suggests a coordination in between these two master transcription factors in the response and adaptation to H_2S and, potentially, in mediating its beneficial effects [246].

A number of studies have reported the effect of H_2S in *C. elegans* stress resistance and lifespan. For example, exogenously providing non-toxic H_2S concentrations to these nematodes can extend their lifespan [147247248249149250]. Conversely, endogenous H_2S production is important in a number of long-lived mutants, such as genetic caloric restriction model *eat-2* [251], germline loss by *glp-1* knockout [252], and mTORC inhibition [253]. Moreover, in *glp-1* mutants, the activation of *skn-1* is required to extend lifespan [252]. To this date, no study has established a causal relationship between H_2S and the longevity induced by the activation of HIF-1 *in C. elegans*. This is somewhat surprising, since many molecules capable of producing H_2S non-enzymatically have been shown to induce lifespan extension in *C. elegans* and other organisms [254248].

Together, these findings highlight a complex interplay between sulfide metabolism, mitochondrial function, and hypoxia signaling in *C. elegans*, yet fundamental questions remain about how these pathways converge to shape organismal physiology. Addressing how sulfide oxidation and HIF-1 activation intersect to influence traits such

as lifespan, body size, and stress resistance — and how these processes can be modulated pharmacologically — formed the central aims of this thesis.

2.9. Thesis aims

The activation of the hypoxia pathway is required for adaptation and response to oxygen deprivation and hypoxia-associated damage in all organs, particularly in those with high metabolic demand such as the kidney [255]. Not surprisingly, genetic and pharmacological activation of the hypoxia pathway has been explored as a potential strategy to prevent or ameliorate ischemic damage, with implications also for aging-associated diseases [256–259]. Increasing evidence indicates that H_2S is not only a toxic by-product of metabolism but also a signaling molecule that interacts with the hypoxia pathway. In *C. elegans* and mammals, H_2S can stabilize or modulate the transcriptional activity of HIF-1, either through inhibition of prolyl hydroxylases (e.g., EGL-9/PHDs) or through persulfidation of downstream effectors, thereby influencing hypoxia responses, metabolic reprogramming, and stress resistance [239,242] Thus, dissecting the crosstalk between H_2S metabolism and hypoxia signaling provides a promising avenue to identify specific pathways or protein nodes that could be targeted to achieve controlled protection against ischemic and age-associated pathologies.

This thesis aimed to:

I. Identify the molecular mediators of the phenotypic consequences of HIF-1 activation in *C. elegans*

II. Examine the molecular basis to the link of H_2S metabolism and hypoxia signaling in resilience and longevity

III. Study the impact of Mesna on H_2S/persulfide modulation as a basis to a potential therapeutic use in ischemia-reperfusion injury

3. Materials and methods

3.1. Materials

3.1.1 Disposable materials

Table 1. List of disposable materials used

Materials	Product Number	Company
Blotting Paper / Grade BF 4	FT-2-521-110170G	Sartorius
Bis-Tris gel, 4% to 12% 1.0 mm, Mini Protein Gel, 12-well	10247002	Thermo Fischer Scientific
Carl Roth™ Opaque Blue Disposable Antistatic Polystyrene Weighing Trays	10057602	Fischer Scientific
Centrifuge tubes, Falcon® (15 ml)	734-0451	VWR
Centrifuge tubes, Falcon® (50 ml)	734-0448	VWR
CryoPure Tube 1.0ml white	72.377	Sarstedt
Empty Gel Cassette Combs, mini, 1.0 mm, 10 well	NC3010	Thermo Fischer Scientific
Empty Gel Cassettes, mini, 1.0 mm	NC2010	Thermo Fischer Scientific
Microtubes (1.5 ml)	72.690.001	Sarstedt
Femtotips®, injection capillary, sterile, set of 20	930000035	Eppendorf
Immobilon-P PVDF membrane	T831.1	Roth
Micro tube 1.5ml	72.690.001	Sarstedt
MicroAmp™ Fast Optical 96-Well Reaction Plate, 0.1 mL	4346907	Thermo Fischer Scientific
Microscope Slide 76 x 26 mm	11102	Engelbrecht
Multiply®-µStrip 0.2ml chain	72.985.002	Sarstedt
Parafilm M laboratory film	PM996	Bemis
Pasteur pipettes	612-1701	VWR
Petri dish 60x15mm with cams	82.1194.500	Sarstedt
Petri dish 92x16mm with cams	82.1473.001	Sarstedt
Polypropylene Bottle (250 ml)	334205	Beckman Coulter

Polypropylene Bottle (1000 ml)	A98812	Beckman Coulter
Platinum Wire 0.2 mm diameter/ 99.9%	900543	CHEMPUR
Pipette bulbs	612-2693	VWR
Peha-soft® nitrile white powder-free	9422083	Hartmann
PIPETMAN Classic	P1000 (F123602), P10 (F144802), P200 (F123601), P20 (F123600)	Gilson
Rotilabo® disposable weighing pans, opaque blue, anti-static (100 ml)	2150.1	Roth
Rotilabo® disposable weighing pans, opaque blue, anti-static (330 ml)	2159.2	Roth
Safe Lock Tubes 1.5 ml	0030120086	Eppendorf
Semi-micro cuvette, PS	67.742	Sarstedt
Strippettes (5 ml)	4051	Corning
Strippettes (10 ml)	4101	Corning
Strippettes (25 ml)	4251	Corning
Yellow Bevelled Tip 10 µl (Sterile), Racked	S1111-3810-C	Starlab
Yellow Bevelled Tip 1000 µl (Sterile), Racked	S1111-6811-C	Starlab
Yellow Bevelled Tip 200 µl (Sterile), Racked	S1111-1816-C	Starlab

3.1.2 Equipments

Table 2. List of equipments used

Instrument	**Product Number**	**Company**
Centrifuge 5810/ 5810 R	5811000620	Eppendorf

Drying / heating oven	T 6030 300	Heraeus
EnSpire Multimode Plate Reader	2300-0000	Perkin Elmer
Ertical floor-standing autoclaves Systec V-Series	V-150	Systec
Fusion solo Chemiluminator	60-FU-SOLO	PeqLab
Gas burner Fuego SCS pro	8.204.000	Wild-tec
Homogeniser	432-3750	VWR
Horizontal Electrophoresis system size L	40-1214	PeqLab
Hypoxia Chamber (Oxymeter)	GMH 3690 GL	Greisinger
Mediaclave 10/30	-	Integra
Mediajet, Petri Dish Filler	-	Integra
Minicentrifuge	521-2844	VWR
Microcentrifuge	5409000210	Eppendorf
Microscope Axio Zoom.V16	495010-0001-000	Zeiss
Microscope Observer.A1	-	Zeiss
NanoDrop Spectrophotometer	1000	PeqLab

Precision balance PCB	PCB 1000-2	Kern
Scanner Perfection V800	B11B223401	Epson
Sonicator/Bioruptor Pico	B01060010	Diagenode
Stereomicroscope	MDG35	Leica
Thermal Cycler	S100	Biorad
Tube roll mixer SRT6	9.728 810	Häberle
UV Transilluminator	Ti5	Biometra

3.1.3 Chemicals and Reagents

Table 3. List of chemicals and reagents used within this work

Chemical / Reagent	**Product no.**	**Provider**
[gamma-P32] Adenosine 5'-triphosphate (ATP)	SRP-501	Hartmann Analytics
Acetic acid	7332.1	Carl Roth
Acetonitrile	701881	AppliChem
Agarose	A9539	Sigma-Aldrich
Agar	11396.03	Serva
Ampicillin Sodium Salt	K029.2	Carl Roth
Ampuwa (Water)	7610894	Fresenius
AP39	SML2389	Sigma
Bacto Peptone	211820	BD
BODIPY™ 581/591 C11	D3681	Invitrogen
Bovine Serum Albumin (BSA)	1066	Gerbu
Calcium chloride ($CaCl_2$)	HN04.2	Carl Roth
Carbenicillin	6344.2	Roth
Cholesterol	C8667-5G	Sigma
Citric acid monohydrate	27490	Fluka
Coenzyme Q9	27597	Sigma-Aldrich
cOmplete™ EDTA-free Protease Inhibitor Cocktail	4693132001	Roche
(L-)Cysteine	168149	Sigma
Diallyl disulfide	30648	Sigma
Diallyl trisulfide	SMB00577	Sigma
Dimethyl sulfoxide (DMSO) Hybri-Max	D2650	Sigma-Aldrich
Dithiothreitol (DTT)	6908.1	Carl Roth

Chemical / Reagent	**Product no.**	**Provider**
DiYO-1	17580	AAT Bioquest
DNase/RNase-Free Distilled Water	15657708	ThermoFisher Scientific
dNTP Mix (10 mM each)	R0191	ThermoFisher Scientific
Dulbecco's Modified Eagle Medium (DMEM)	D6429	Sigma-Aldrich
Ethanol (99.8%)	9065.3	Carl Roth
Ethidium bromide solution	2218.1	Carl Roth
Ethylenediaminetetraacetic acid (EDTA)	15575020	ThermoFisher Scientific
Fetal Bovine Serum (FBS)	S 0115	Biochrom AG
Gel Loading Dye, Orange (6X)	B7022S	New England Biolabs
GeneRuler 1kb DNA Ladder	SM0311	ThermoFisher Scientific
GeneRuler 50bp DNA Ladder	SM0372	ThermoFisher Scientific
Glucose	G7021	Sigma-Aldrich
GlutaMAX	35050061	ThermoFisher Scientific
Glutathione Monoethyl Ester	353905	Milipore
Glycerol	3783	Carl Roth
GYY4137 Dichloromethane complex	SML0100	Sigma-Aldrich
Heparin Natrium solution	15782698	Braun
HEPES	H0887	Sigma-Aldrich
Hoechst 33342 Solution (20 mM)	62249	ThermoFisher Scientific
Hydrogen chloride (HCl)	T134	Carl Roth
Hydrogen Peroxide (H_2O_2) 30%	107209	Merck
Igepal CA-630	I8896	Sigma-Aldrich
Isopropanol	5752.3	Carl Roth
Isopropyl-β-D-thiogalacto-pyranosid (IPTG)	730-1497	VWR
KH_2PO_4	P5655	Sigma-Aldrich
LB-Agar	X965	Roth
LB-Medium	X964	Roth
Lipofectamine RNAiMAX	13778075	ThermoFisher Scientific
Luminol	9253	Fluka
Magnesium chloride ($MgCl_2$)	1.05833.0250	Merck
Mesna-cell 400mg (Injektionslösung)	03194720	Stada
Magnesium sulphate heptahydrate ($MgSO_4$)	P027.2	Carl Roth
Methanol	4627.5	Carl Roth
Methyl viologen dichloride hydrate (Paraquat)	856177-1G	Sigma-Aldrich
MitoSOX	M36008	Invitrogen

Chemical / Reagent	Product no.	Provider
Monopotassium phosphate (KH_2PO_4)	3904.1	Roth
Normal Donkey Serum (NDS)	017-000-121	Dianova
Nystatin (10 mg/ml)	475914	Calbiochem
Opti-MEM	31985-047	ThermoFisher Scientific
Paraformaldehyde (PFA)	P6148	Sigma-Aldrich
Penicillin-Streptomycin 10,000 U/mL (Pen-Strep)	15140-122	ThermoFisher Scientific
Phenylmethylsulfonyl fluoride (PMSF)	A0999	AppliChem
Polyacrylamide (PAA)	T802.1	Carl Roth
Potassium chloride	6781.1	Carl Roth
Protease Inhibitor Cocktail III	539134-1ML	Merck
Sodium Azide	S2002	Sigma
Sodium chloride (NaCl)	3957.1	Carl Roth
Sodium dodecyl sulfate (SDS) powder	A2263	AppliChem
Sodium hydrogen phosphate (Na_2HPO_4)	S9390	Sigma-Aldrich
Sodium hydroxide (NaOH)	A3910.1000	AppliChem
Sodium hydroxide solution 2N	T135	Roth
Sodium orthovanadate (Na_3VO_4)	S6508	Sigma-Aldrich
SSP4	SB10	Dojindo
Tetramethylrhodamine ethyl ester perchlorate	87917	Sigma-Aldrich
Tecan Spark		LifeSciences
TRI Reagent®	T3934-200ML	Sigma-Aldrich
Tris Hydrochloride (Tris-HCL)	9090.3	Carl Roth
TritonX-100	3051.2	Carl Roth
Trizma base	T1503	Sigma-Aldrich
Tryptone	1010817	MP Biomedicals
Yeast Extract	2363.1	Carl Roth
5-Fluoro-2′-deoxyuridine (FUDR)	F0503	Merck

3.1.4 Primers

Table 4. Table of primers for *C. elegans* genotyping and sequencing

vhl-1 fp	TCATAAACCGCTGTCAATCG	Genotyping PCR
vhl-1 rp	AAAACGACCGTATGGGGAAT	Genotyping PCR
vhl-1 fp	ATCATCCATGGGTTGCTAGG	Genotyping PCR
sqrd-1 fp	GGATGTGGATGGTGGGTCAT	Genotyping PCR
sqrd-1 rp	AACAGAGTGTAGCGGAACCC	Genotyping PCR
L4440 fp	CAGTGAGCGAGGAAGCAA	RNAi sequencing

L4440 rp	AAAACGACGGCCAGTGAG	RNAi sequencing

3.1.5 Assays and Kits

Table 5. List of assays and kits used within this work

Assay / Kit	Product no.	Provider
ADP/ATP Ratio Assay Kit	MAK135-1KT	Sigma-Aldrich
Direct-zol RNA Miniprep Kit	R2052	Zymo Research
High-Capacity cDNA Reverse Transcription Kit	4368814	Applied Biosystems
High-Performance GoTaq® G2 DNA Polymerase with Mg-Free Buffer System	M7801	Promega
Mitochondrial Membrane Potential Kit	MK159-1KT	Sigma-Aldrich
PCR Mycoplasma Test Kit I/C	PK-CA91-1096	PromoKine
Pierce™ BCA Protein Assay Kit	23225	Thermo Fischer
Quick-DNA Miniprep Plus Kit	D4069	Zymo Research

3.1.6 Buffers and solutions

Table 6. List of buffers and solutions used within this work

Buffer / Solution	Composition
Base solution (50x)	12.5 ml NaOH (5N)
	1 ml EDTA (0.5 M)
	36.5 ml ddH_2O
Bleach Solution	0.4M NaOH 7.5% NaClO
Cell Culture Medium (mIMCD3)	10% (vol/vol) FBS
	2 mM GlutaMAX
	1 x Pen-Strep
	in DMEM/F12
Enhanced Chemiluminescence Solution (ECL)	100 mM Tris (pH 8.5)
	1.25 mM Luminol
	0.2 mM Coumaric acid
	0.75% (vol/vol) H_2O_2
	pH 8.5
Freezing medium	90% (vol/vol) FBS
	10% (vol/vol) DMSO
Freezing Solution	100mM NaCl 50mM KH2PO4 3.26M Glycerol 300mM MgSO4

Laemmli (5x)	62.5 mM Tris pH 6.8
	10% (wt/vol) Glycerol

	2% SDS
	50 mM DTT
	Bromphenolblue
Lysis Buffer	100 mM Tris pH 7.5 500 mM LiCl 10 mM EDTA pH 8 1% LiDS 5 mM DTT 1 Tablet Protease inhibitor per 50 mL
Lysis Buffer (H_2S)	6M Urea 2% SDS 150 mM Tris-HCl (pH 7.4)
Modified RIPA buffer	10 mM Tris, pH 8
	1 mM EDTA
	0.5 mM EGTA
	1 % Triton-X100
	0.1% Sodiumdeoxycholate
	44 µg/µl PMSF
	2 mM Na3VO4
M9 buffer	3g KH_2PO_4 6g Na_2HPO_4 5g NaCl Fill up to 1L of dH_2O Autoclave 1mL $MgSO_4$ 1M
NGM media	NaCl 3g Bactopeptone 2.5g Agar 17g dH_2O till 1000ml Autoclave 1 mL Cholesterol 5mg/mL 1 mL $CaCl_2$ 1M 1 mL $MgSO_4$ 1M 25 ml KPO_4 buffer 1M pH6 10.000units/mL
PBT-X	0.1 % Triton X-100
	in PBS
Phosphate Buffered Saline (PBS)	137 mM NaCl
	2.7 mM KCl
	10 mM Na_2HPO_4
	2 mM KH_2PO_4

Protein wash buffer	30 mM Tris
	300 mM NaCl
	0.3% Tween20
	pH 7.5
RNAi plates	NGM media IPTG 1M 1mL

	Ampicillin 5mg/mL 1mL Tetracycline 12.5mg/mL 1mL
Running buffer	25 mM Trizma base
	192 mM Glycine
	0.1% (wt/vol) SDS
S-medium	5.9g NaCl 50mL 1M KH_2PO_4 pH6 950mL dH_2O Autoclave 1mL of 5mg/mL cholesterol (in EtOH) 10mL 1M Potassium Citrate Buff. pH6 10mL Trace Metals solution Use to suspend fresh OP50 to 1.5O.D
Separating gel buffer	750 mM Tris
	10% (vol/vol) PAA
	0.2% (wt/vol) SDS
	pH 8.8
SOC medium	2% (wt/vol) Tryptone 0.5% (wt/vol) Yeast Extract 8.6 mM NaCl 2.5 mM KCl 20 mM $MgSO_4$ 20mM Glucose
Stacking gel buffer	250 mM Tris 5% (vol/vol) PAA 0.2% (wt/vol) SDS pH 6.8
TAE buffer (1x)	40 mM Tris (pH 8.5) 20 mM Acetic Acid 1mM EDTA
Tris Buffered Saline (TBS) (20x)	300 mM Tris-HCl 92.5 mM Tris Base 3 M NaCl pH 7.6
Transfer buffer	25 mM Tris 188 mM Glycine 0.1% (wt/vol) SDS
Trace Metals solution	1.86g EDTA 0.69g $FeSO_4$ 0.2g $MnCl_2$ 0.29g $ZnSO_4$ 0.016g $CuSO_4$ dH_2O to 1000mL
Tris-EDTA buffer (10x)	100 mM Tris Base 12.7 mM EDTA 0.05% Tween-20 pH 9

3.1.7 Strains of *C. elegans*

Table 7. List of *C. elegans* strains used

Strain	Genotype	Source
N2 (Bristol)	WT	CGC
CB5602	*vhl-1(ok161)*	CGC
TMB032	*vhl-1(ok161)* 3x outcrossed to WT	Nephrolab
AR13	*sqrd-1(mr28)*	CGC
TMB100	*sqrd-1(mr28) 3*x outcrossed to WT	Nephrolab
TMB101	*vhl-1(ok161);sqrd-1(mr28)*	Nephrolab
ZG31	*hif-1(ia4)*	CGC
TMB009	*hif-1(ia4)* 3x outcrossed to WT	Nephrolab
CB6090	*hif-1(ia4);vhl-1(ok161)*	CGC
TMB069	*hif-1(ia4)* 3x outcrossed to WT	Nephrolab
TMB071	*vhl-1(ok161);hif-1(ia4)*	Nephrolab
PHX6787	*sqrd-1::mKate2::3xFLAG (syb6787)*	Sunny Biotech
RB1651	*mpst-1(ok2040)*	CGC

TMB107	*mpst-1(ok2040)* 3x outcrossed with WT	Nephrolab
VC4718	*cbs-1(gk5787)*	CGC
VC2569	*cth-1(ok3319)*	CGC
RB899	*cysl-1(ok762)*	CGC
VC40209	*mpst-7(gk514674)*	CGC
VC3092	*ethe-1(ok3755)*	CGC
EU31	*skn-1(zu67)*	CGC
LD1	ldIs7 [skn-1b/c::GFP + rol-6(su1006)]	CGC
AA1065	ldIs7 [skn-1b/c::GFP + rol-6(su1006)] 2x outcrossed	Antebi's Lab
DMS640	*nIs470[cysl-2p::GFP+ myo-2p::mCherry]*	CGC
CL2122	*dvIs19[pAF15(gst-4::GFP::NLS)]*	CGC
CF1553	*muIs84 [(pAD76) sod-3::GFP* + *rol-6]*	CGC

3.1.8 Bacteria

Table 8. List of bacterial strains used

Species	Strain	Source
Escherichia coli	OP50	CGC
Escherichia coli	HT115 (DE3)	CGC

3.1.9 RNA interference

Table 9. List of bacteria used for RNA interference

Target	Sequence	Source
Empty vector	L4440	CGC
sqrd-1	F02H6.5	Ahringer Library
hif-1	F38A6.3	Ahringer Library
vhl-1	F08G12.4	Ahringer Library
dod-24	C32H11.12	Ahringer Library
fmo-2	K08C7.5	Ahringer Library
srx-12	Y55F3AM.2	Ahringer Library
nhr-251	ZK488.4	Ahringer Library
dod-21	C32H11.10	Ahringer Library
gst-19	F37B1.8	Ahringer Library
srd-15	C04E6.10	Ahringer Library
ets-7	F19F10.5	Ahringer Library
fbxc-7	C32B5.9	Ahringer Library
nuo-4	K04G7.4	Ahringer Library
nuo-5	Y45G12B.1	Ahringer Library
col-8	F11H8.3	Ahringer Library
col-149	B0024.1	Ahringer Library
sdha-1	C03G5.1	Ahringer Library
mpst-3	H12D21.7	Ahringer Library
ldh-1	F13D12.2	Ahringer Library
pck-1	W05G11.6	Ahringer Library
phy-2	F35G2.4	Ahringer Library

3.1.10 Cells

Table 10. List of cell lines used

Name	Species	Parental cell line	Clone number	Genotype
mIMCD3 #8	Mouse	mIMCD	#8	WT

3.1.11 Software

Table 11. List of software used

Software	Version	Provider
Perseus	1.6.2.2	https://maxquant.net/perseus/
GraphPad Prism	10.4	https://www.graphpad.com/
Fiji	2020-02-25 15:47	https://imagej.net/Fiji
Excel	Microsoft Office Professional Plus 2016	https://www.office.com/?omkt=de-DE
STRING	Online	https://string-db.org/
ZEN Blue	3	Zeiss

3.1.12 Antibodies

Table 12. List of antibodies used

Antigen	**Catalog Number**	**Provider**	**Dilution**	**Usage**
Anti-SQRDL	HPA017079	Sigma	1:2000	Western Blot IF
Anti-RFP	ab203129	Abcam	1:500	Western Blot
IgG Mouse	115-035-003	Dianova	1:30000	Western Blot
IgG Rabbit	111-035-045	Dianova	1:15000	Western Blot

3.2 Caenorhabditis elegans

3.2.1 *C. elegans* culture and maintenance

The strains used were acquired from the Caenorhabditis Genetics Center (CGC) or, in the case of double mutants, were crossed in our lab. All the strains acquired from the CGC have been crossed at least once with our wild type (N2, Bristol) animal, so that background mutations specific to our laboratory were accounted for in every genotype. All strains (except when stated otherwise) have been kept on NGM (Nematode Growth Media) agar plates seeded with *E. coli* OP50 (uracil auxotroph) at 20°C. Long term culture of all strains was kept in triplicate in a 50/50 mixture of M9 medium containing L1 (Larval stage 1) starved worms (L1 arrest) and Freezing solution. Cryotubes were kept at -80°C.

3.2.2 Escherichia coli culture

E. coli has been cultured in LB medium overnight, under constant agitation (120rpm) at 37°C. Grown culture had its OD (optical density) measured at 600nm and concentrated to an OD of 1. Large (90mm), medium (60mm), or small (30mm) petri dishes were seeded with 500 µL, 200 µL, and 100 µL of *E. coli* culture, respectively, and left to dry overnight. Original culture was long term kept in a 80/20 mixture of LB culture+OP50 and glycerol at -80°C.

3.2.3 *C. elegans* culture synchronization/staging

Big amounts of age-synchronized worms were obtained by bleaching, where a final concentration of 0.5% NaOCl and 300mM NaOH were added to a pellet of gravid worms (second day of egg laying period) collected in M9 buffer. After strong shaking, only eggs are left and these are placed in an OP50 seeded NGM plate to hatch overnight.

For smaller amounts of worms, synchronization was done via egg-laying, where a small number of young adults (first day of reproductive period) animals were placed in a 60mm OP50 seeded NGM plate for a period not longer than 2h, and allowed to lay eggs. The adult animals were sacrificed after the time was over and the eggs were allowed to hatch overnight in the plate. The number of animals and the egg laying

period were determined depending on how many animals were needed in each individual assay.

3.2.4 RNAi mediated knockdown

RNAi mediated knockdown was conducted by feeding *C. elegans* with the HT115 strain of *E. coli,* which expresses double stranded RNA that can be processed into a single strand capable of knocking down complementary mRNA inside *C. elegans'* body [260]. HT115 culture was grown overnight in LB medium supplemented with 100 µg/mL of ampicilin and 12.5 µg/mL of tetracyclin. Culture OD was adjusted to 1.5 and a final concentration of 1mM of IPTG was added to it. Concentrated culture was then seeded onto NGM plates containing 1mM of IPTG and 100 µg/mL of Ampicilin. Worms have been kept feeding on RNAi containing bacteria for variable periods of time depending on the specific gene to be knocked down, or the duration of the experiment. All RNAi constructs were confirmed by sequencing with the use of L4440-specific plasmids and blasting it against the *C. elegans* genome.

3.2.5 *C. elegans* genotyping

Single worm genotyping was conducted by adding 11µL of base solution on top of one animal, and letting it incubate for 30min at 95°C. Lysis was stopped by adding 11µL of neutralisation solution. 2µL of lysate containing genomic DNA was used as template for a PCR reaction using 100µM of primers specific to the expected genotype. The following was added to the PCR mix:

Table 13. Composition of PCR mix for genotyping

Flexi Green Buffer	10 µL
$MgCl_2$ (25mM)	3 µL
dNTP (25mM)	0,2 µL
Primer 1 (100µM)	0,5 µL

Primer 2 (100µM)	0,5 µL
Primer 3 (100µM)	0,5 µL
ddH_2O	10 µL
Worm Lysate	2 µL

The PCR setup to genotype *sqrd-1(mr28)* mutants and *vhl-1(ok161)* mutants was:

Table 14. Detailed PCR settings for genotyping

1. Denaturation	95°C	30s
2. Annealing	55°C (*vhl-1*)/56°C (*sqrd-1*)	30s
3. Extension	72°C	45s
Cycling (2 and 3)		40x
4. Ending	72°C	5min
Store	4°C	∞

Amplified DNA fragments were run on a 2% Agarose gel prepared with 1µL of 1% ethidium bromide for detection. *vhl-1* (ok161) mutant band is 300bp, while its WT counterpart is 650bp. *sqrd-1* (mr28) mutant band is the same size as its WT counterpart, since this mutation comprises a T>C substitution. Therefore, 12µL of amplified DNA was sequenced (Microsynth - Sanger) using 3µL of the 100µM stock of the FW primer for *sqrd-1* (mr28).

3.2.6. Preconditioning

Supplementation with different chemicals was conducted with previously bleach-synchronised L4 animals. L4 larval stage animals were removed from 60mm NGM plates with the help of M9 buffer and collected in a 15mL falcon tube and washed 3x with 10mL of M9 for complete bacteria removal. A total of 500 L4 animals were suspended in 5mL of S-medium with resuspended OP50 (O.D 1.5). Finally, the media with the animals and OP50 was supplemented with the indicated concentrations of the metabolites (L-cysteine, Na_2SO_3, GYY4137, Mesna, AP39, DADS, DATS). The tubes were kept at light rotation in the horizontal position for 24h in a dark environment at 20°C.

3.2.7. Lifespan assay

Lifespan assays were conducted using the Lifespan Machine [261]. Briefly, 20-25 D0 bleaching staged (first day of egg-laying) animals were placed in OP50-seeded 60mm NGM plates. 200µM of fluorodeoxyuridine (FUDR) were added to the media during its preparation in order to inhibit reproduction and keep homogenously aged populations in the plates. Plates were set to be scanned every thirty minutes, providing a high resolution to the verification of whether animals were dead or alive. Experiments were run for a maximum of 25 days, which is enough to reach the maximum lifespan of most strains we used. After the experiment reached its end, the machine software was run to determine whether animals were dead or alive and when. Every single animal was then manually checked via a storyboard with hundreds of pictures collected by the machine around the calculated time of death. Animals got their time of death either confirmed or adjusted by manual inspection, and animals with either inconclusive death time, or that escaped the area scanned and recorded by the machine, were censored. Finally, the machine outputs the time of death of every individual animal in a table that is then plotted as a survival graph using GraphPad Prism 9.

3.2.8. Body length

Body length measurement was conducted with either L1 or L4 staged animals, after RNAi mediated knockdown or exposure to different chemicals, respectively. Specifically, bleaching staged L1 (F1) animals were obtained from adult worms (P0) that had been cultivated in RNAi capable HT115 bacteria specific to the mRNA we

wanted to knockdown. 500 eggs were allowed to hatch into L1 worms overnight in empty (no source of food) 90mm NGM plates, so that growth due to food ingestion cannot happen while body size measurement is being conducted. For L4 staged animals, the process happened as described in the “Preconditioning” session.

The actual measurement was conducted by using the Fiji plugin “Wormsizer” (https://github.com/bradtmoore/wormsizer) [262], in identical manner for both experimental setups. Animals were either kept or transferred to empty 90mm NGM plates (L4 animals had to be washed 3 times with M9 buffer in order to eliminate all bacterial food source). Images of the animals were obtained with the Axiozoom (Zeiss) microscope at either 69x magnification for L1 animals or 25x for L4 animals. The plugin was calibrated by imaging a micrometric ruler at several different magnifications and entering the values in pixel per micron on Fiji.

3.2.9. Stress resistance

Stress resistance was assessed by cultivating D0 worms in NGM plates prepared with 5mM paraquat till they were all dead, or, alternatively, till the day of sample collection (D2 for proteomics or D1 for ROS and lipid peroxidation). The same protocol was followed using preconditioned animals. Briefly, a fresh (a new solution was prepared every time a new batch of plates was made) stock solution was prepared by adding 3.9mL of ultra-pure water directly on top of 1g of paraquat (methyl viologen). 3.1mL of the stock solution were used to prepare 500mL of NGM plates by mixing it while the media is still liquid and kept at 60°C, yielding a 5mM solution (3.9mL of H_2O + 1g of methyl viologen results in 4.8mL of a 810mM solution). Plates also contained 200μM of FUDR. Plates were stored safe from light overnight. One day after preparation, 60mm NGM plates were seeded with freshly grown OP50 and let to dry, safe from light, for one more day. D0 animals were washed out of their original plates with M9 buffer and 20-25 were then pipetted on top of Paraquat/FUDR-containing plates. Death was then monitored by the lifespan machine for 8 days, while for other assays the animals were collected from Paraquat/FUDR-containing plates at previously mentioned specific timepoints for analysis.

3.2.10. Hypoxia chamber

A digital oximeter (Greisinger GMH3690GL) was used to monitor and control O_2 concentration inside in-house built sealed containers shaped to fit samples, such as NGM plates. These containers were connected to our gas supply (O_2 and N_2) and to a separate container with water, to prevent dehydration of the plates, and to allow for quick visualisation of gas flow. 50 L4 animals in open 60mm NGM plates were placed in the hypoxia chamber where O_2 concentration was 0.1% (hypoxia) for 24h. In an adjacent chamber, where O_2 concentration was 21% (normoxia), control NGM plates with the same amount of worms were placed.

3.2.11. Development under hypoxia

Preconditioning was done by preparing plates with the chemicals (Mesna, DADS, or DATS) inside the NGM media, where exposition was conducted from eggs (egg laying synchronisation) till L4 larval stage (48h). L4 animals were then exposed to either hypoxia or normoxia for 24h in new NGM plates, without any preconditioning chemicals, were scored either as an adult or not depending on the presence of eggs in their uterus.

3.2.12. Protein aggregation under hypoxia

Preconditioning was done by preparing plates with the chemicals (Mesna, DADS, or DATS) inside the NGM media, where exposition was conducted from eggs (egg laying synchronisation) till L4 larval stage (48h). Preconditioning was done by preparing plates with the Mesna inside the NGM media, where exposition was conducted from eggs (egg laying synchronisation) till L4 larval stage (48h). Protein aggregation was assessed by scoring the number of foci of fluorescent Q35::YFP that accumulate over the intestine of adult animals.

3.2.13. Sulfur metabolites measurement

Frozen samples containing 5000 D1 aged worms were slowly thawed in ice bath and centrifuged at 14000g, 4°C for 5 minutes. The supernatants were carefully aspirated and discarded, the pellets were resuspended in 200 µl ice-cold 75% MeOH solution containing 5mM HPE-IAM. Samples were sonicated on ice for 20 cycles (0.1s on - 0.9s

off). After the first 10 cycles, the tubes were briefly vortexed to loosen the pelleted worms. The tubes were transferred to dry block heaters and incubated at 37 °C for 20 minutes under constant mixing. Then the samples were immediately cooled off in an ice bath, centrifuged at 14000g, 4°C for 5 minutes. 100µl of the supernatants were mixed with 5µl formic acid, diluted twice fold with 0.1% FA/H_2O in HPLC autosampler vials with inserts and placed into the autosampler unit set to 5°C for HPLC-MS/MS analysis. The precipitated proteins were dissolved in 1%SDS/PBS and subjected to BCA assay for protein content determination.

HPLC-MS/MS measurement was carried out on a Thermo Scientific Vanquish UHPLC, coupled to a Thermo Scientific Q Exactive Focus instrument and samples were analyzed using two different methods described below [263].

Low molecular weight thiols and persulfides were separated using a Phenomenex Kinetex C18 (50 x 2.1 mm, 2.6 µm) column with an injection volume of 5µl. A linear gradient consisting of 0.1%FA in H_2O (A) and 0.1% FA in MeOH (B) was employed, with a flow rate of 0.5 ml/min. The gradient started with 5%B, increased to 13%B in 2 minutes, further increased to 95%B in 4 minutes and held there for 0.5 minutes. B% was decreased to 5% in 0.1 min and held there for 3.4 minutes until the next injection. The column was kept at 40°C and positive ESI ionization was used for the MS/MS detection. Mass transitions monitored and HCD energies used can be found in **Table 12** below.

Thioethers and disulfides were separated using a Thermo Hypercarb (100 x 2.1 mm, 3µm) column with an injection volume of 5µl. A linear gradient consisting of 0.5%FA in H_2O (A) and 0.5% FA in 1:1 ACN/IPA (B) was employed, with a flow rate of 0.2 ml/min. The gradient started with 0%B, increased to 3%B in 1.5 minutes, further increased to 30%B in 3.5 minutes, then to 100% in 1 minute. 100%B was held for 2 minutes, then decreased to 0% in 1 min and held there for 8 minutes until the next injection. The column was kept at 40°C and positive ESI ionization was used for the MS/MS detection. Mass transitions monitored and HCD energies used can be found in **Table 15**.

Table 15. Detailed settings for sulfur metabolites detection

Analyte	Precursor (m/z)	Fragment (m/z)	HCD fragmentation energy
LMW thiols and persulfides			
cysteine	299	121	34
cysteine-persulfide	331	121	35
glutathione	485	356	16
glutathione-persulfide	517	388	18
hydrogen sulfide	389	252	15
Thioethers and disulfides			
cystathionine	223	134	19
oxidized glutathione	307	130	

3.2.14. Proteomics

3.2.14.1. Worm sample preparation

4 µL lysis buffer (0.25% DDM, 125 mM TEAB, 10 mM TCEP (Tris(2-carboxyethyl) phosphine), 20 mM CAA (chloroacetamide)) were added to each PCR tube on ice. A single worm was added to each tube, and the tubes were immediately frozen in liquid nitrogen until ready for further processing. 8 single worms were used for each condition. The tubes with a single worm each were thawed simultaneously in a water bath at RT, and the samples were frozen and thawed two additional times to ensure proper cell lysis. The samples were then sonicated with Bioruptor Plus (Diagenode S.A.) coupled to Minichiller 300 (Huber) (20 cycles, 30 seconds on, 30 seconds off) while maintaining a temperature of 4°C. While the Bioruptor was running, Trypsin/LysC protease (1 µg/µl Trypsin and 0.5 µg/µl LysC in 50mM acetic acid) was diluted 10-fold in LCMS water to create the "DiluteProtease" solution. After the Bioruptor treatment, 5 µL of cold PBS (“Invitrogen 10x PBS” diluted 10-fold with LCMS water) was added to each sample, followed by 1 µL of the DiluteProtease. The samples were mixed briefly

and spun down. The samples were incubated at 37°C overnight in a PCR cycler. After the incubation, the samples are ready for loading into EvoTips for further analysis.

3.2.14.2. Mass spectrometry

The digested single worm lysis was loaded to the EvoTip Pure according to manufacturer's instruction. The Evosep One liquid chromatography system (Bache, Geyer et al. 2018) was used for analyzing the samples with the predefined 30 samples per day (30SPD) method. The analytical column used was an ReproSil-Pur column, 15 cm x 150 µm, with 1.9 µm C18 beads (EV1106 Endurance Column, Evosep). The mobile phases A and B were 0.1 % formic acid in water and 0.1% formic acid in 100% ACN, respectively. Peptides were analyzed on a hybrid TIMS quadrupole TOF mass spectrometer (timsTOF Pro 2, Bruker) in a data-independent acquisition parallel accumulation, serial fragmentation (diaPASEF) mode. The mass spectra range was set to 100-1700 m/z and TIMS ion accumulation and ramp times were set to 100 ms and total cycle time was 2.0 s. The ion mobility range was set to 1/K0 = 0.8-1.25 V s/cm2. Isolation windows in the m/z versus ion mobility plane were defined to cover the region of highest precursor ion density with an m/z slice width of 26 Th. Collision energy was applied linearly with ion mobility from 0.6 to 2.0 V s/cm2, and collision energy from 20 to 59 eV.

3.2.14.3. Analysis

Raw data was analyzed using Spectronaut version 19.3.24 (Biognosys) using the default parameters against the one-protein-per-gene reference proteome for C. elegans, UP000001940, downloaded August, 2022. Methionine oxidation and protein N-terminal acetylation were set as variable modifications; cysteine carbamidomethylation was set as fixed modification. The digestion parameters were set to "specific" and "Trypsin/P," with two missed cleavages permitted. Protein groups were filtered for at least two valid values in at least one comparison group and missing values were imputed from a normal distribution with a down-shift of 1.8 and standard deviation of 0.3. Differential expression analysis was performed using limma, version 3.60.6 (Ritchie, Phipson et al. 2015), in R, version 4.4.0 (Ritchie, Phipson et al. 2015).

3.2.14.4. Pathway enrichment analysis (STRING)

For pathway enrichment analysis we used the online tool STRING (https://string-db.org/). For all analysis we used a list with all proteins detected as the background proteome. Terms were put in order by their FDR values, and similar terms were merged when above 1.0 similarity. Pathway enrichment analyses were performed to interpret the functional significance of differentially expressed genes. KEGG pathway enrichment was used to identify overrepresented biological pathways. *C. elegans* Phenotype Ontology (MONARCH) analysis linked gene expression changes to known phenotypic outcomes. Subcellular localization was predicted using COMPARTMENTS to determine where the encoded proteins are likely to act within the cell. Molecular function enrichment assessed the main biochemical activities associated with the gene set.

3.2.15. Microscopy

To obtain quantifiable images from different fluorescent reporters or dyes, Axio Observer (Zeiss) microscope with Apotome. Briefly, worms to be imaged were mounted in agarose pads over glass slides. The animals were placed side by side in a drop of 5mM Levamisole, so that they would be paralyzed at the time of imaging. Capturing was conducted in a dark room, with all worms fitting together in the frame, and exposition times were adjusted accordingly to fit the highest fluorescence obtained across all groups without overexposure. Each group was mounted into the slides only briefly before imaging, so as to avoid changes induced by such procedure on reporter levels.

3.2.16. Mitochondrial reactive oxygen species

Mitochondrial reactive oxygen species (ROS) were measured by preparing 5mM stock solution of MitoSOX (Sigma) with DMSO, from which a 10µM working solution was then prepared using M9 buffer, and pipetted onto a 60mm OP50-seeded NGM plate. MitoSOX plates were then covered in foil and left to dry at 20°C overnight. 20-30 L4 worms were then added to the dried MitoSOX plates and left to incubate, still covered in foil, for 24h.

At the day of the image acquisition, each group was individually transferred to a new OP50-seeded 60mm NGM plate and the animals were let to crawl for 2h, so that their intestines and cuticle would be free of excess dye. Times were planned ahead so that each group would be the same amount of time in the cleaning plates. Image acquisition followed the standard procedure with the red filter and the Z-stack function (30-40 sections per slide). Analysis was conducted with the Z-stack function of Fiji, where 10-15 slides were used to create a single image that was then analysed for integrated fluorescence per area at the pharynx of the worms. Pharynx was selected with the manual drawing function.

3.2.17. Lipid peroxidation

Lipid peroxidation was measured by preparing a 2mM stock solution of BODIPY C11 (Sigma) with DMSO, from which a 10µM working solution was prepared using M9 buffer. 500µL of working solution was added on top of a OP50-seeded 60mm NGM plate and let to dry under a hood for at least 10min. 20-30 D1 worms (previously grown for 24h in plates containing 5mM of paraquat) were then manually transferred to the plates, which were covered in foil and incubated for 24h.

At the day of the image acquisition, D1 animals were individually transferred to a new OP50-seeded 60mm NGM plate and let to crawl for 2h, so that their intestines and cuticle would be free from excess dye. Times were planned ahead so that each group was given the same amount of time in the cleaning plates. Image acquisition followed the standard procedure with both red and green filters being used to acquire both reduced and oxidized versions of the dye, respectively. Whole body fluorescence was measured and normalised by the area of each individual worm. The final data was expressed as a reduced/oxidized ratio (red/green fluorescence).

Alternatively, a plate reader was used to confirm our measurements. There, 100 D1 animals (previously grown for 24h in plates prepared with 5mM of paraquat) were transferred to 1,5mL tubes containing 500µL of 10µM BODIPY C11 solution (5µL of 2mM stock + 995µL of M9 buffer), or alternatively containing only M9 buffer as a control. A M9 buffer + 10µM BODIPY C11 was also kept as a control. The groups were then submitted to constant agitation for 30min, washed 3x with 1mL of M9 buffer, and finally transferred to a 96-well plate with the help of non-sticky 200µL tips that were

previously filled with M9 buffer to improve their non-stickness to the worms. The volume pipetted varied, therefore all wells were adjusted to contain 200µL of buffer and worms in total.

Microplates were read at 590nm emission and 568nm excitation for reduced (red) and at 530nm emission 488nm excitation for oxidized (red) dye using the Tecan Spark™ microplate reader. Results were calculated by substracting M9 only buffer from non-stained samples, and using this individual value from each strain to substract from its respective stained group.

3.2.18. Mitochondrial membrane potential (MMP) and Mitotracker

A 100mM stock was prepared by diluting 25mg in 500 µL of DMSO. The stock solution was further diluted till 100 µM with M9 buffer. 150 µL of the 100 µM stock were added on top of a 60mm OP50 seeded NGM plate. The plates have been dried with an open lid under a sterile hood for at least 10min, till complete drying. The plates were covered in foil and stored for 24h at 20°C.

As a control, Mitotracker Green (MT) was used to normalise TMRE signal. Mitotracker plates were prepared by adding 1 µL of a 1mM stock to 199 µL of M9 buffer, and then diluting it 10x in freshly grown OP50 culture. 60mm NGM plates were then seeded with 150uL of OP50+MT mixture.

20 young adult worms were allowed to egg-lay for 2h in regular OP50 seeded plates. The progeny was allowed to grow for 48h and then 50 L4 worms were transferred to the TMRE, TMRE+MT, or only MT containing plates, wrapped on foil. Worms were allowed to crawl and ingest TMRE/MT for 24h. After that, the worms were transferred to non-TMRE plates for 1h, so that excess stain would be removed by pure OP50 ingestion.

Each biological replicate consisted of at least 15 worms per group, all mounted together in 1% agarose pads and immobilised using 5µL of 20mM Levamisole. TMRE ingestion was checked by visualising the hypodermic tissue on the head of the animals at 40x magnification. Pictures at 10x magnification, including all worms, were taken and total fluorescence in both red (TMRE) and green (MT) channels were quantified

and analysed using ImageJ. TMRE (red channel) signal was normalised by MT (green channel) signal by expressing TMRE/MT ratio.

3.2.19. Oxygen consumption rate (Respiration)

One day before the experiment, one Seahorse Extracellular Flux Plate was prepared by adding 200µL of Calibrant solution in each well and incubating it overnight at 37°C. At the day of the experiment, 22µL of a 500µM FCCP solution (in DMSO) were added to their respective chambers (slot B) in the Extracellular Flux Plate, for a final concentration of 50µM final concentration of 50µM of FCCP. The same procedure was done with NaN_3 (in water) (slot C) for a final concentration of 4mM. For respiration measurement worms were obtained via the egg-laying synchronization protocol. After 4 days, 15 to 20 D1 of age worms per condition were manually transferred to a 96-well plate filled with 200µL of M9 buffer. Final measurements for basal (initial measurement before FCCP induction) and maximal (FCCP induced – spare respiration) respiration were normalised to the number of worms in each well.

3.2.20. qPCR

qPCR reactions were performed with Power SYBR™ Green PCR Master Mix. qPCR primers (IDT) used for thw qPCR are listed in Table 4. qPCR compositions and cycling conditions are listed in the **Table 13**. qPCR was run using the samples in technical triplicates and genomic DNA, -RT (sample lacking the reverse transcriptase), and H_2O as controls. The reaction was performed using the QuantStudio 12K Flex Real-time PCR System and data was analyzed with Quantstudio and Prism software.

3.2.20.1. RNA extraction

RNA extraction was done by adding 700µLof TRIzol to freshly collected D0 old animals in a 2mL safelock tube containing beads for homogenization in the Precellys 24 at 4000rpm 3x 10s with 10s pause between cycles. RNA was extracted with the Direct-zol™ RNA Miniprep Plus kit according to the manufactures protocol. The RNA concentrations were measured using the Nanodrop 1000 spectrophotometer.

3.2.20.2. Reverse transcription

cDNA synthesis was performed using the High-Capacity cDNA Reverse Transcription kit according to manufacturer's protocol. The reaction composition and settings are listed in the **Table 16**.

Table 16. cDNA synthesis composition and settings

Method	Component	Volume	
Reverse transcription	10X RT Buffer	2.0	µl
	25X dNTP Mix (100 mM)	0.8	µl
	10X RT Random Primers	2.0	µl
	MultiScribe™ Reverse Transcriptase	1.0	µl
	H_2O	4.2	µl

Settings	Step 1	Step 2	Step 3	Step 4
Temperature [°C]	25	37	85	4
Time [min]	10	120	5	Hold

Table 17. Primers used for qPCR in *C. elegans*

rpl-32 fp	AGGGAATTGATAACCGTGTCCGCA
rpl-32 rp	GTAGGACTGCATGGGAGCATGT
sqrd-1 fp	TGGAGGAAGGAGATGAGCTG
sqrd-1 rp	TGGAGGTGAGTTGGTGATGA

3.2.21. Western blot

50 worms were picked into 1 ml lysis buffer and sonicated (Sonopuls sonicator) 5 times for 10 seconds at 65% potency. Afterwards, 2xLaemmli buffer was added and the sample was incubated for 5 minutes at 95°C. 30 µl of the samples were loaded on a 12% Bis-Tris polyacrylamide gel and the gel was run at 150V constant for 60 minutes. The PVDF membrane was activated before by incubation for 30 seconds in methanol. Meanwhile, the gel and the two filter papers were soaked in transfer buffer. Next, the gel was transferred into a transfer chamber where a sandwich was built with the

following order from bottom to top: filter paper, PVDF membrane, gel, filter paper. The transfer was run at 12V for 60 minutes. The membrane was incubated with a blocking solution (4% BSA in wash buffer) for one hour. Then the membrane was washed three times with wash buffer and incubated for 1 hour with the primary antibody (1:1500) recognizing the mKate2 antigen (RFP). After another washing round of three times the membrane was incubated for 1 hour with the horseradish peroxidase (HRP) labeled secondary antibody (1:15000) anti-rabbit. Finally, the membrane was washed three times and overlaid with 100µl Femto Luminol buffer. The chemiluminescence was visualized using a chemiluminescence imaging system (Fusion solo).

3.3 Cell culture

3.3.1. Culturing immortalized cell lines

Cells were grown at 37°C and 5% CO_2 in standard incubators. All cell culture handling was done under sterile conditions inside laminar-flow hoods. Cells were propagated by washing them with PBS, adding 1mL of trypsin and incubating it for 5min inside a standard CO_2 incubator. Trypsinisation was interrupted by resuspending the cells in FBS (Fetal Bovine Serum)-containing culture media, and they were seeded in fresh, pre-warmed media in new 10cm culture dishes in a 1:6 dilution for maintenance or 1:2 before experiments. Inner medulla collecting duct (mIMCD3) cells were kept in DMEM media supplemented with 10% FBS, 2mM GlutaMAX and 1% penicillin/streptomycin. mIMCD3 cells used were a previously characterised subclone (subclone #8) that presented considerable ciliation and the expression of distal tubule specific markers compared to the polyclonal population of mIMCD3 cells, therefore here we will refer to it as mIMCD3#8.

3.3.2. Freezing and thawing cells

Cells were prepared to be frozen for long term storage by letting them expand to about 90% confluence in a 10cm dish, washed with PBS, and incubated for 5min with 1mL trypsin. After 5min incubation inside a CO_2 incubator, 5mL of FBS-containing DMEM was added and the whole content was transferred to a 15mL tube, which was

centrifuged for 5min at 1500rpm at room temperature. Supernatant was removed and the pellet resuspended in 1mL of freezing medium. Cryogenic vials containing 1 mL of cells and freezing medium mixture were first put at -80°C inside a Mr. Frosty™ freezing container, and later transferred to a liquid nitrogen tank. Thawing was done by letting cryogenic vials at room temperature till all content was liquid, after that the cells were resuspended in 5mL of FBS-containing DMEM and centrifuged at 1500rpm for 5min at room temperature. The pellet was then resuspended in media and seeded onto 10cm dishes. All cells were tested for mycoplasma using a PCR Mycoplasma Test Kit.

3.3.3. siRNA-mediated knockdown

Cells were split 1:7 in 6-well plates with FBS-containing DMEM media, supplemented with 1% GlutaMAX and no antibiotics and left to grow overnight to reach a confluence of around 50-60%. Next morning, the cells were transfected with 40nM of the respective siRNA (ON-TARGETplus SMARTpool, Dharmacon), or control siRNA (ON-TARGETplus NON-targeting Control pool, Dharmacon) per well, using Lipofectamine RNAiMAX™ transfection reagent. was used. Two solutions, A and B, were prepared as described in the **Table 18**, mixed, and incubated for 5min at room temperature.

Table 18. Preparation of solutions for siRNA transfection

	Solution A	Solution B	Non-Targeting Control (ID)	Sqor siRNA (ID)
Opti-MEM	6 µL	-		
siRNA (20µM)	-	4.8 µL	D-001810-10	L-063889-01-0005
LipoRNAiMAX	200 µL	200 µL		

After the 5min incubation, solution A and B were mixed and incubated for more 20min at room temperature. At the end of the incubation time, 400µL of the mix was added to

the wells, properly mixed, and let incubate for 24h, when further experiments were then conducted.

3.3.4. Exposure to preconditioning drugs

Cells were submitted to a preconditioning protocol with different H_2S donors either after siRNA mediated knockdown and before the stress resistance, or skipping siRNA mediated knockdown and going directly for the stress resistance assay. Briefly, cells were split 1:2 and let to grow overnight to a confluence of around 80-90% in a 90mm plate, so that the maximum number of cells would be obtained. After that, the cells were either seeded in a 6-well plate for siRNA mediated knockdown, or directly seeded in 96-well plate at a density of 5000 cells per well and let to attach to the bottom of the plate overnight (procedure described in detail in the "Live cell imaging" session). Finally, H_2S donors (Mesna, GYY4137, or DAS) were diluted on FBS-containing DMEM (2mM GlutaMAX, no antibiotics) and used to culture the cells. Controls with the respective solvents were used with the equivalent amount of solvent of the highest concentration tested. **Table 19** described how each drug was diluted, as well as which solvent was used, and respective volumes.

Table 19. Preconditioning media preparation

	Mesna 600µM	**Solvent/Control: H_2O**	**GYY4137 100µM**	**GYY4137 200µM**	**DAS 1mM**	**Solvent/Control: DMSO 0.8%**
Stock	(Stock 100mg/mL) 10µL	10µL	(Stock 25mM) 40µL	(Stock 25mM) 80µL	(Stock 25mM) 40µL	(Stock 100%) 80µL
Media	9990µL	9990µL	9960µL	9920µL	9960µL	9920µL
Total	200µL	200µL	200µL	200µL	200µL	200µL

3.3.5. Live-cell imaging and stress resistance

Cells that had been transfected with specific siRNA were were trypsinised and resuspended in FBS-containing DMEM medium, supplemented with 2mM GlutaMAX and no antibiotics. The number of cells was then counted with the help of the Luna-II™ Automated Cell counter (Logo Bioscience). 5000 cells were then seeded in a 96-well plate, where all outermost wells were filled with media only to avoid drying during the long time live cell imaging was conducted. Cells were let to attach to the bottom of the wells overnight. Cells were then either exposed to a drug of interest or their respective vehycles for 24h, at the end of which they were washed with the same media they were cultivated by emptying the wells completely and adding the original volume (200µL) back again two times. At the last wash, 200µL of media with 15µM of DIYO-1 or DIYO-1 + paraquat 10mM was added on top of the cells. Monitoring of cell death was done with the Incucyte™ S3 (37°C; 5% CO_2). A 20x objective was used to acquire a total of four green fluorescent images per well (dead cells), and four phase-contrast images of the same fields (total cells), every 2 hours. The Incucyte™ Cell-by-Cell Analysis software conduced the analysis based on selected images of different timepoints that were analysed by hand to determine what was and what was not a dead cell.

3.3.6. Lipid peroxidation

Lipid peroxidation was assessed using a final concentration of 1µM of BODIPY C11 (Sigma). 15000 cells were cultured in 300µL of FBS-containing DMEM media within an imaging-prone 8-well µ-slide with the ibiTreat™ coating for cell adhesion and proliferation. At the day of the assay, cells (previously exposed to siRNA and aftwerwards to H_2S donors) were exposed to 10mM paraquat-containing media for 6h, and very carefully (drops added from the corners) washed 2x (complete removal of supernatant, followed by 300µL of HBSS) with HBSS media (with Hoescht 1:1000). At the end cells were kept in Ringers solution. Washing and paraquat exposure were timed so that each group was exposed to the same conditions for the same time. Each well was imaged at 4 different fields at 40x magnification using both green and red channels. Data was analysed by measuring the total green and red fluorescence in each individual cell, which were individualised with the help of the Hoescht staining, and normalising it by area and background, according to the CTCF (Corrected Total Cell Fluorescence) formula: Integrated Density – (Area of selected cell x Mean

fluorescence background). Background measurement were taken at any empty field in each well. The ratio in between green (non-oxidized) and red (oxidized) fluorescence was used to plot a graph.

3.3.7. Mitochondrial reactive oxygen species

Mitochondrial reactive oxygen species were measured using a final concentration of 5μM of MitoSOX (Sigma). 15000 cells were cultured in 300μL of FBS-containing DMEM media within an imaging-prone 8-well μ-slide with the ibiTreat™ coating for cell adhesion and proliferation. At the day of the assay, cells (previously exposed to siRNA and aftwerwards to H_2S donors) were exposed to 10mM paraquat-containing media for 6h, and very carefully (drops added from the corners) washed 2x (complete removal of supernatant, followed by 300μL of HBSS) with HBSS media (with Hoescht 1:1000). At the end cells were kept in Ringers solution. Washing and paraquat exposure were timed so that each group was exposed to the same conditions for the same time. Each well was imaged at 4 different fields at 40x magnification using the red channels. Data was analysed by measuring the total green and red fluorescence in each individual cell, which were individualised with the help of the Hoescht staining, and normalising it by area and background, according to the CTCF (Corrected Total Cell Fluorescence) formula: Integrated Density – (Area of selected cell x Mean fluorescence background). Background measurement were taken at any empty field in each well. The red fluorescence measurement was used to plot a graph.

3.3.8. Hydrogen sulfide measurement

1mg of HSip-1 was diluted with 139μL of PBS to prepare a 100 μM working solution: 7500 cells (previously exposed to specific siRNA and/or H_2S donors) were grown in a 96-well plate. Media removed and cells were washed with HBSS buffer 2x. 50μL of lysis buffer was added and (carefully as to not form bubbles) pipetted up and down 3x. 100μL of HSip-1 working solution was added to each well and let incubate at room temperature for 30min. Green fluorescence was measured in the Tecan Spark™ (Exc. 491nm, Em: 516nm). Results were obtained by using the obtained measurements to calculate sulfide concentration from an equation obtained from a calibration curve using Na_2S (200-0μM) diluted in water as standard, with the same incubation time as the one applied to the samples.

3.3.9. Persulfides measurement

A 10 mM stock solution of SSP4 (Dojindo) was prepared by adding 165µL of DMSO on top of 1mg of SSP4, from which a 10 µM working solution was prepared in serum-free DMEM containing 0.5mM of permeabilising agent cetyltrimethylammonium bromide (CTB). 15000 cells, previously exposed to siRNA and to H_2S donors, were grown in an imaging-prone 8-well µ-slide with the ibiTreat™ coating for cell adhesion and proliferation. Cells were washed off of FBS by adding and removing two times 300µL of serum-free DMEM. As a positive control, 100 µM of Na_2S_3 was added to some wells for 15min, and washed 2x with PBS. Finally, cells were incubated with SSP4 and CTB -containing serum-free DMEM for 15min inside of a CO_2 incubator. Supernatant was discarded and the cells were washed twice with HBSS containing Hoescht 1:1000, and kept in 200µL of Ringer's solution for imaging after the last wash. Cells were then imaged at 40x magnification using the green fluorescence filter.

3.3.10. ADP/ATP ratio

The ratio between ATP and ADP was measured according to the instructions provided by the manufacturer of the kit (ATP/ADP Ratio Assay Kit – Milipore/Sigma). Briefly, 10.000 cells (previously exposed to specific siRNA and/or H_2S donors) were seeded in a white 96-well plate with flat and clear bottom and let to attach and grow overnight. To measure ATP, ATP reagent was prepared according to the instructions within the kit, and 90µL of it were added to the cells without any media. After 1min of incubation at room temperature, luminescence was measured to obtain RLU_A. ADP reagent was prepared according to the instructions within the kit, and after 10min of ATP measurement, the plate was read again to obtain RLU_B. Immediately after, 5µL of ADP reagent were added and well mixed into each well and luminescence was again measured after 1min of incubation to obtain RLU_C. ADP/ATP ratio was obtained by calculating $(RLU_C - RLU_B) / RLU_A$.

3.3.11. Mitochondrial membrane potential

Mitochondrial membrane potential was measured according to the instructions provided by the manufacturer of the kit (Mitochondrial Membrane Potential Kit – Milipore/Sigma). Briefly, 10.000 were seeded in a 96-well black plate with a clear flat bottom and let to attach and grow overnight. 50µL of JC-10 Loading Dye Solution

(prepared according to the instructions included in the kit) were added to each well with cells and media and incubated inside a CO_2 incubator for 60min. At the end of the incubation period, 50µL of Assay buffer B were added and carefully mixed into each well. Fluorescence was measured in the microplate reader Tecan Spark™ (red: 540nm ex, 590nm em; green: 490nm ex, 525nm em). MMP was determined by calculating the ration red/green fluorescence, where red fluorescence is emitted on high polarised mitochondria, and green fluorescence is emitted on low polarised mitochondria.

3.3.12. Immunofluorescent staining of cells

Cells were grown in 24 well plates on round glass coverslips until reaching a confluence of 60-80%. The growth medium was removed, the cells were carefully washed with PBS and fixed in 4% formaldehyde for 15 minutes. After washing 3x 5 minutes with PBS the cells were blocked in 5% normal donkey serum (NDS) in PBT-X for 1 h at RT. The cells were washed 3x 5 minutes with PBS and incubated with the first antibodies diluted in 5%NDS/PBT-X as listed in Table 12 overnight at 4°C. Three times washing with PBS was followed by incubation with fluorescently labeled secondary antibodies (Table 14) and Hoechst (1:1000) for 45 minutes at RT. The coverslips were washed 3x 5 minutes with PBS and mounted using Prolong Diamond antifade reagent. Imaging was performed using the TCS SP8 Confocal microscope and image analysis was performed with ImageJ/Fiji.

3.3.13. Cell lysis and RNA extraction

Harvesting was conducted by removing growth media, placing cells on ice, and washing them with ice cold PBS. After PBS was removed, 700µL of Trizol were added and a cell scrapper was used to detach all cells from the plate. Cell pellets plus Trizol were let to incubate at room temperature for 15min and then submitted to RNA extraction with the Direct-zol™ RNA miniprep kit, including DNAseI digestion. RNA was then eluted in 20µL of ultrapure, RNAse-free, H_2O. Quality and quantities were assessed using the Nanodrop™ 1000 spectrophotometer, according to the manufacturer's instructions.

3.3.14. Reverse transcription and qPCR

1µg of RNA was transcribed into cDNA using the High-Capacity cDNA Reverse Transcription kit, following the manufacturer's instructions. One sample was submitted to Cdna reverse transcription without the reverse transcriptase, to be used as a control in the qPCR. Primers targeting the mRNA of interest were used and SYBR green was used to detect amplification in 384-well plates in the Quantstudio 12L Flex Real-Time PCR system. Data was analysed using the Quantstudio software provided with it. A description of the amounts of reagents used for each reaction are depicted in **Table 20**.

Table 20. Master mix composition for qPCR

	Sample	**Negative Control**	**Amplification control**
cDNA	1µL	-	-
Not amplified (genomic DNA)	-	-	1µL
Master mix	5µL	5µL	5µL
Primers mix	0,5µL	0,5µL	0,5µL
H_2O	4,5µL	5,5µL	4,5µL

4. Results

4.1. Identification of the sulfide-quinone oxidoreductase *sqrd-1* as a mediator of HIF-1 induced body length and lifespan phenotypes

We aimed to investigate how different modes of HIF-1 activation shape organismal physiology and gene expression programs in *C. elegans*, with a particular focus on the metabolic and developmental outcomes of *vhl-1* deletion. In line with our broader goal of understanding how HIF-1 influences growth and adaptation, we had previously observed that *vhl-1(ok161)* mutant *C. elegans* are shorter throughout their larval development and adult life, and that this phenotype is *hif-1* dependent (**Figure 6A–C**). To gain insight into the molecular basis of this phenotype, we performed RNA sequencing of these worms. A hierarchical clustering analysis (HCA) revealed close transcriptomic similarity between wild-type (WTN2), *hif-1* mutants, and *vhl-1;hif-1* double mutants, whereas *vhl-1* mutants clustered separately (**Figure 6D**). The HCA identified three major clusters of genes with similar regulatory patterns across genotypes. While cluster 1 comprises genes that are upregulated in *vhl-1* mutants and downregulated in *vhl-1;hif-1* double mutants, cluster 3 shows the opposite pattern, and cluster 2 displays a more complex relationship between genotype and gene regulation.

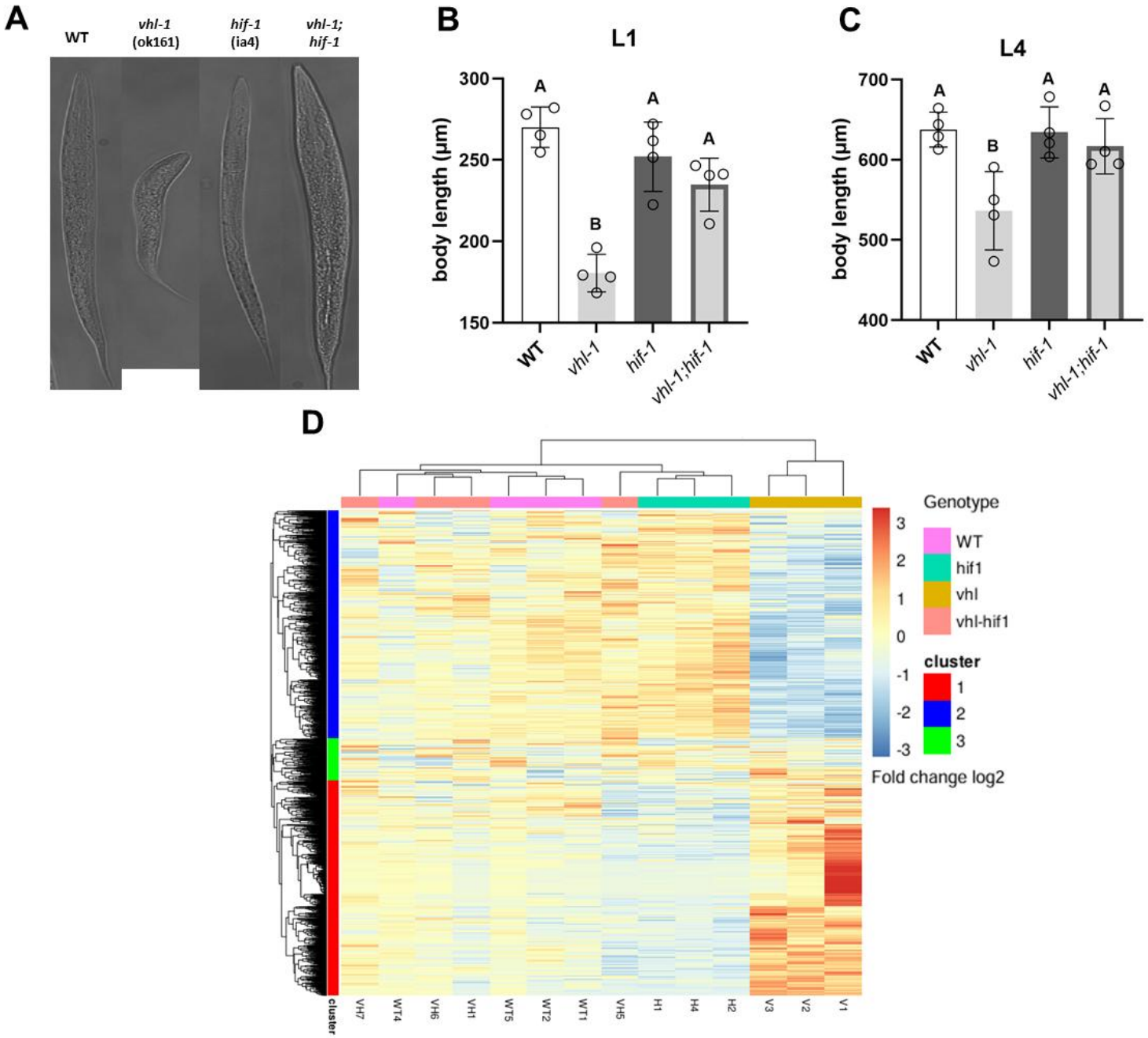

Figure 6. The *vhl-1(ok161)* mutation leads to shortening of *C. elegans* in a *hif-1* dependent manner.

A) Representative images of L1 stage worms; B) Body length measurement of L1 stage worms. Each dot represents one biological replicate consisting of at least 100 individual worms; C) Body length measurement of L4 stage worms. Each dot represents one biological replicate consisting of at least 100 individual worms; D) Heat map representing the hierarchical clustering analysis of differentially regulated genes identified by RNA-seq in L4 stage worms. n≥3 for all groups. Differential expression is displayed as Log2 fold change. For figures B and C groups that are statistically different (at least $p<0.05$, One-Way ANOVA, Tukey's post-hoc test) are highlighted by different letters on their top. Similar letters denote no statistical difference.

As the impact on body length was clearly dependent on *hif-1*, we only considered genes regulated in a *hif-1* dependent manner as a basis to a genetic interaction screen. Log2 fold change values for expression of the selected candidates are represented in **Table 21**

	log_2 fold change *vhl* vs WT	log_2 fold change *hif-1* vs WT	log_2 fold change *vhl-1* vs *vhl-1;hif-1*
comt-4	8.2	-1.82	9.38
dod-21	7.8	0.23	8.37
gst-19	7.6	-1.59	8.84
srx-12	6.6	-2.04	6.89
fmo-2	5.6	-1.21	7.63
srx-21	5.1	-2.4	4.5
srd-13	5.1	-0.006	4.2
nhr-251	4.7	0.23	4.5
sqrd-1	3.8	-1.96	6.1
smf-3	3.69	-5.21	8.09
dod-24	3.51	-2.56	3.67
srd-15	3.39	-0.006	3.18
fxbc-7	3.4	-0.006	3.18
ets-7	2.7	-0.7	1.006

Table 21. Top upregulated *hif-1* dependent genes in *vhl-1(ok161)* mutants.

Red denotes positive regulation of expression, while blue denotes negative regulation of expression. Values are displayed as a Log2 fold change.

We selected the top genes that were 1) upregulated in *vhl-1* mutants in comparison to WT (Log_2 fold change ≥2); 2) unchanged or downregulated in *hif-1* mutants in comparison to WT; 3) upregulated in vhl-1 mutants compared to *vhl-1;hif-1* double mutants. We considered a p-value <0.05 as indication of significant statistical difference between the groups. Out of these over 100 genes, 14 were selected due to their availability in the RNAi library we have access to. This screen was performed in *vhl-1* loss-of-function worms and knockdown of hif-1 served as a positive control. As expected, RNAi mediated knockdown for *hif-1* did not display the same capacity to counteract the shortened body length size as *hif-1* (ia4) knockout did (**Figure 6B** and

C), but still increased *vhl-1* mutants body size (**Figure 7A**). Among the candidates tested, 5 were able to produce an appreciable and comparable effect in increasing size of *vhl-1* mutants. The strongest rescue was obtained by knockdown of *sqrd-1*, which encodes the sulfide:quinone oxidoreductase, a mitochondrial protein that is the limiting step in the catabolism of H_2S [51]. A known and characterized *srqd-1* mutant strain (sensitivity to high concentrations of H_2S [264] knockout mutant, *sqrd-1(mr28)*, we crossed this strain into the *vhl-1(ok161)* mutant background. While characterizing this genotype, we observed that indeed *sqrd-1* is – at least largely – responsible for the short size of *vhl-1* mutants in L1 and L4 larval stages (**Figure 7B-D**). It is worth noting that *sqrd-1* mutants are slightly shorter than WT animals at L4 larval stage (**Figure 7D**). Because development is directly associated with the body length of *C. elegans*, we considered the possibility of vhl-1 interfering with developmental timing, which seems to be the case only for reaching adulthood (**Figure 7E**), therefore not interfering with our previous observations. Finally, we wondered if the long lifespan of *vhl-1* mutants could also be regulated by *sqrd-1*. Intriguingly, loss of *sqrd-1* completely abrogates the increased lifespan of *vhl-1* mutant worms while having no effect on lifespan in the wildtype background (**Figure 7F**).

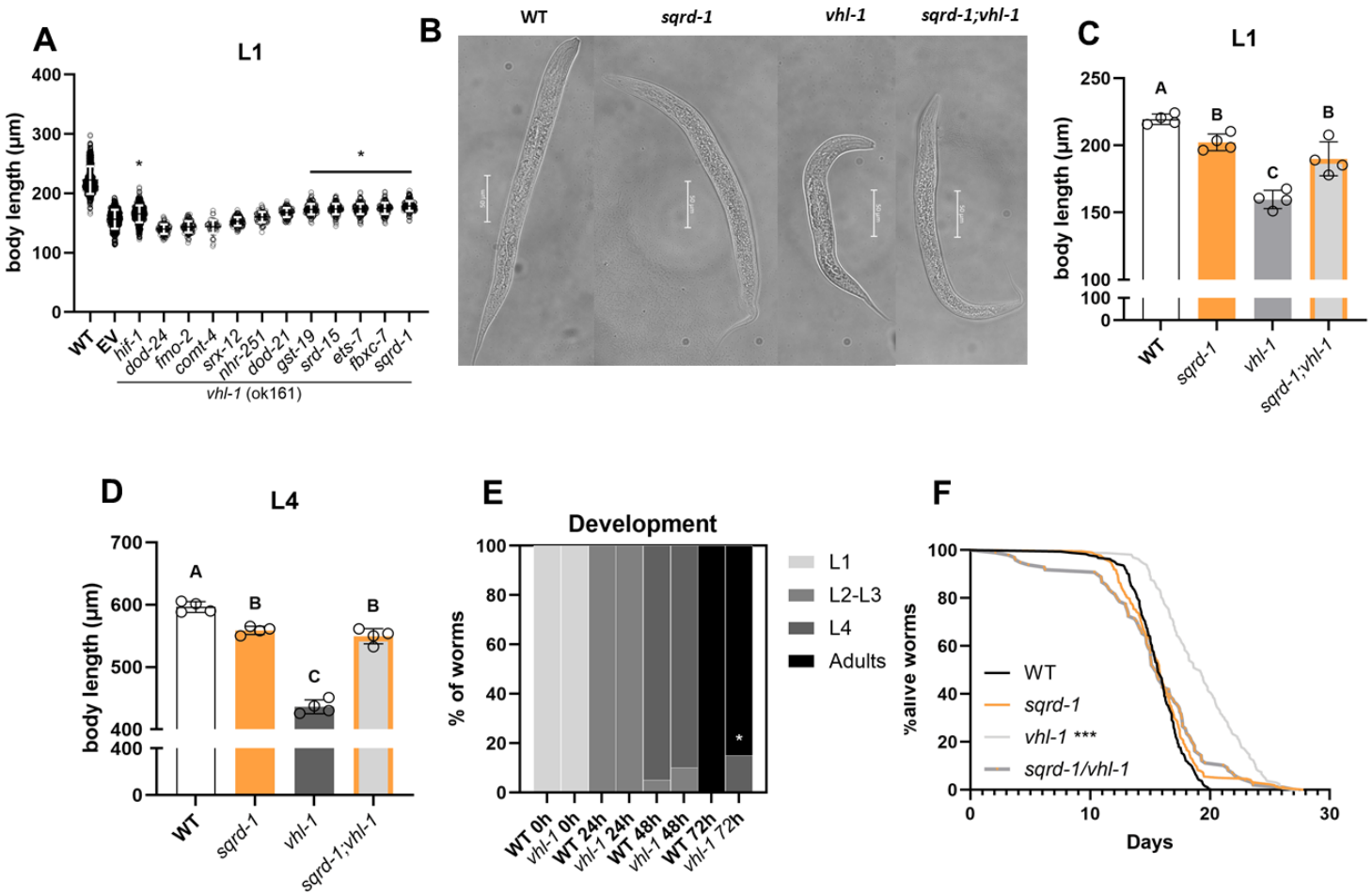

Figure 7. Loss of function of the sulfide quinone oxidoreductase *sqrd-1(mr28)* largely restores the shortened body size of *vhl-1(ok161) C. elegans* mutants and completely abrogates their extended lifespan.

A) RNAi screen for body length regulation using the available top gene candidates based on the RNAseq data; B) Representative images of L1 stage worms; C) Body length measurement of L1 stage worms; D) Body length measurement of L4 stage worms; E) Developmental stages over time (percentage of worms in the designated larval stage at that timepoint); F) Lifespan curve. Number of worms per group across 4 biological replicates: n worms per group WT=378, *sqrd-1*=434, *vhl-1*=326, *sqrd-1;vhl-1*=296. Groups that are distinct ($p<0.05$ in a One-Way ANOVA followed by Tukey's post-hoc test) are highlighted by different letters on their top in figures 5C and 5D. Similar letters denote no statistically appreciable difference. * and *** denotes a $p<0.05$ and $p<0.0001$, respectively, according to One-Way ANOVA followed by Tukey's post-hoc test for body size (5A) and development (5E), or according to Kaplan-Meier analysis and Logrank test for lifespan (5F).

4.2. *Sqrd-1* knockout counteracts *hif-1* target regulation in *vhl-1* mutants

To unveil the molecular basis to the role of *sqrd-1* in *hif-1* signaling, we performed a proteome analysis at 3 different timepoints (Day 1, Day 6, Day 15 of age – D1, D6, D15). PCAs of these datasets reveal, that PC1 primarily separate *vhl-1* mutant worms from all other genotypes (**Figure 8A-C**). Loss-of-function of *sqrd-1* in the *vhl-1* mutant background reverts the proteome of these worms to a global state much more similar to WT, implying that *sqrd-1* largely contributes to the *hif-1* dependent protein expression changes.

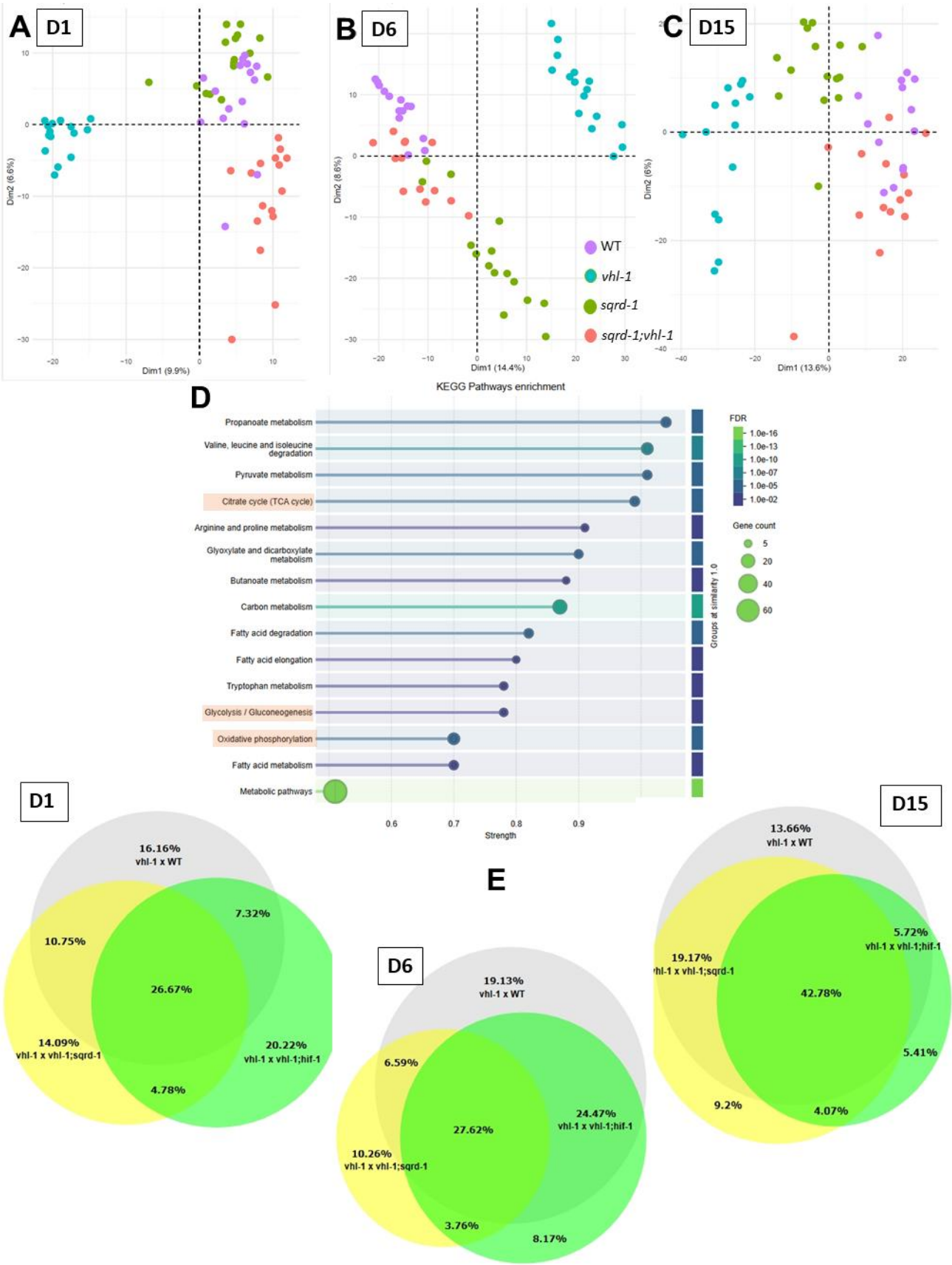

Figure 8. *sqrd-1* mutation reverses HIF-1 related changes in the proteome of *vhl-1 C. elegans* mutants.

continued on next page

A) PCA representative of all regulated proteins at D1 (2nd day after reproduction onset) of age. B) PCA representative of all regulated proteins at D6 (7th day after reproduction onset) of age; C) PCA representative of all regulated proteins at D15 (16th day after reproduction onset) of age. Each dot in the PCAs is representative of one worm out of 16 collected independently over two different experiments (n=2); D) KEGG pathway enrichment analysis of the top 15 up- and down-regulated pathways across days 1, 6, and 15 in *vhl-1* mutants, highlighting changes that occur in an *sqrd-1*–dependent manner. Terms are ordered by FDR, where the x-axis indicates strength and the y-axis indicates term similarity, while the circle size indicates the number of proteins included in each term; E) Venn diagrams representative of all proteins regulated (up and down) in *vhl-1* x WT (gray), *vhl-1* x *vhl-1;hif-1* (green), and *vhl-1* x *sqrd-1;vhl-1* (yellow) across all three timepoints.

To further characterize our proteomic data, KEGG pathway enrichment analysis was conducted with all regulated (up and down) proteins in *vhl-1* mutants ($p<0.05$ in comparison to WT) that were also *sqrd-1* dependent (not regulated in *sqrd-1;vhl-1* double mutants). Classical hypoxia related pathways were identified in the top 15 terms, such as the citric acid cycle, glycolysis, and oxidative phosphorylation (**Figure 8D**). To assess if the changes in the proteome of *vhl-1* mutants caused by the *sqrd-1* mutation affect classic *hif-1*/hypoxia pathway targets, we tested whether *vhl-1* regulated proteins that were *hif-1*-dependent could also be *sqrd-1* dependent. We observed an overlap of 26% at D1, 27% at D6, and up to 43% at D15 of age between proteins regulated in *vhl-1* that were dependent on both *hif-1* and *sqrd-1* (**Figure 8E,** central overlap between all colours). If we consider all proteins regulated in *vhl-1* mutants both dependent and independently from *hif-1,* an even larger portion is *sqrd-1* dependent: 37% for D1, 34% for D6, and 62% for D15.

To gain further insight into which pathways were changed and in which direction at determined timepoints, we again employed KEGG pathway enrichment analysis, however now looking individually at only up or downregulated proteins across the different days. We observed that among the *sqrd-1* dependent downregulated proteins in *vhl-1* mutants, at all three timepoints, classical hypoxia induced (upregulated) metabolic pathways were overrepresented (**Figure 9**, left panels), such as glycolysis, TCA cycle, and oxidative phosphorylation. Among the *sqrd-1* dependent upregulated proteins in *vhl-1* mutants, terms such as ‘’sulfur metabolism’’ and ‘’cysteine metabolism’’ were overrepresented at D1 of age, while many terms regarding RNA metabolism were present in the later timepoints (**Figure 9**, right panels).

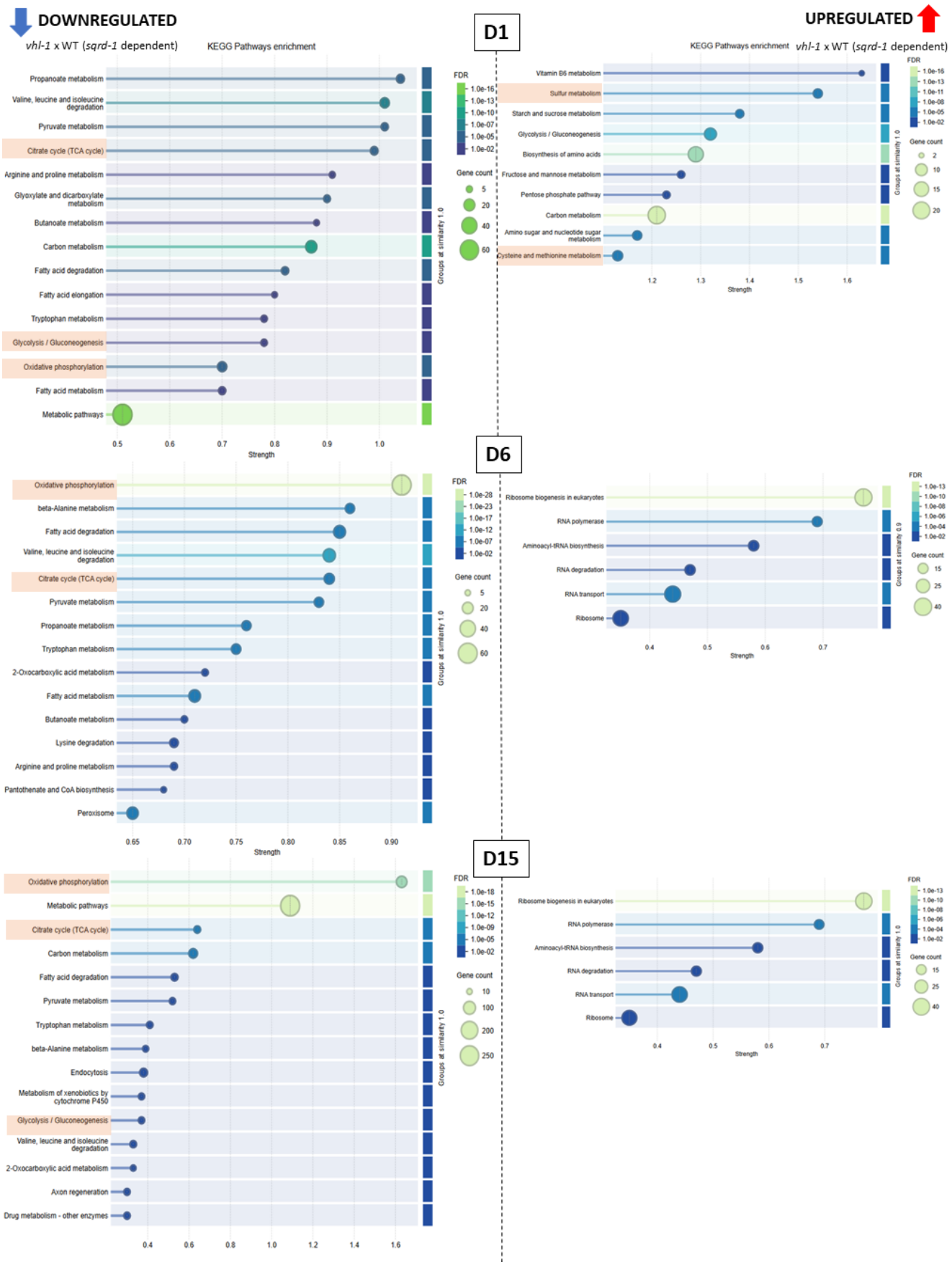

***9. KEGG pathway enrichment analysis of* sqrd-1*-dependent proteins regulated in* vhl-1 *mutants at day 1, 6, and 15 of age in* C. elegans.**

continued on next page

Left panels include only downregulated proteins in *vhl-1* mutants (in comparison to WT) that show a changed pattern of regulation in *sqrd-1;vhl-1* double mutants at day 1, 6, and 15 of age (D1, D6, D15). Right panels include only upregulated proteins in *vhl-1* mutants that show a changed pattern of regulation in *sqrd-1;vhl-1* double mutants at D1, D6, and D15 of age. Terms are ordered by FDR, where the x-axis indicates strength and the y-axis indicates term similarity, while the circle size indicates the number of proteins included in each term.

4.3. Altered mitochondrial function and increased hydrogen sulfide metabolism are *sqrd-1* dependent changes in *vhl-1* mutants

We were surprised to find that among the *sqrd-1*–dependent upregulated proteins in *vhl-1* mutants, sulfur metabolism–related proteins were only represented at the first day of adulthood according to our KEGG pathway enrichment analysis (**Figure 9**, right panel). To investigate this further, we manually examined all known enzymes involved in H_2S synthesis and catabolism in our proteomic dataset. Contrary to what the KEGG pathway analysis initially suggested, both H_2S production and degradation were altered overall in *vhl-1* mutants (**Figure 10A**). Given that SQRD-1 is a mitochondrial enzyme catalyzing the rate-limiting step of H_2S oxidation, we focused on changes in mitochondrial H_2S catabolism and found it to be consistently upregulated across all time points compared to wild type. In contrast, cytosolic enzymes involved in H_2S synthesis, such as CTH-1 and CBS-1, showed little change (**Figure 10A**). Mitochondrial resident proteins such as SQRD-1, ETHE-1, SUOX-1, and shuttling proteins such as MPST-3 are, generally, regulated throughout all timepoints (**Figure 10A** and **Table 22**). Notably, SQRD-1 and MPST-3 appear among the most consistently (on all timepoints) upregulated proteins in the *vhl-1* mutants proteome overall, with fold changes as large as 11 and 6 times, respectively (**Table 22**). SUOX-1 seems to follow an inversed pattern to the other mitochondrial proteins responsible for catabolizing H_2S, going from downregulated at the first two timepoints (D1 and D6), to being upregulated at the latest (D15), at the same time that ETHE-1 and MPST-3 decrease their expression (**Figure 10A** and **Table 22**). All of the changes mentioned were *sqrd-1* dependent. We also measured H_2S and related metabolites on D1 of age and observed an increase in H_2S, cysteine, glutathione, and their related persulfides (cysteine persulfide and glutathione persulfide/GSSH), while no changes in cystathionine were detected (**Table 22**).

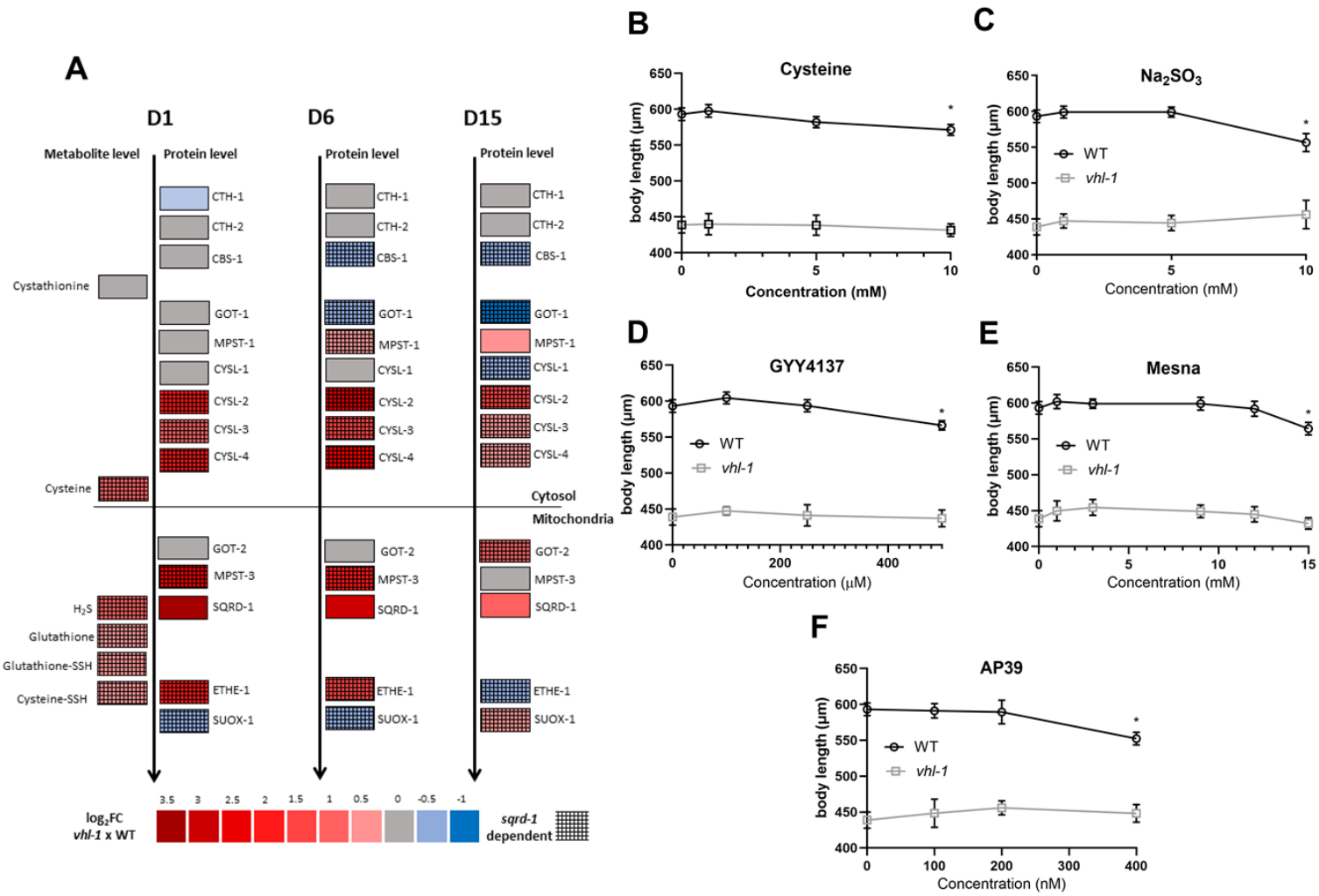

Figure 10. Increased H_2S and sulfide metabolism related proteins can induce *C. elegans* body shortening.

A) Transulfuration pathway proteins (D1, D6, and D15), mitochondrial catabolism proteins (D1, D6, D15), and related metabolites (D1) measurement in *vhl-1* mutants. From top to bottom the direction in that the pathway generally (but not exclusively) goes is represented by the arrows. Top portion represents cytosolic proteins, while bottom half represents mitochondrial proteins. Each vertical segment represents one timepoint (D1, D6, D15). Mesh filling pattern indicates changes in expression are lost in double *sqrd-1;vhl-1* mutants compared to single *vhl-1* mutants. Values are displayed as a Log2 fold change. All colored boxes, except for gray, display changes that are statistically significant ($p<0.05$); **B-E**) Body length measurement of *C. elegans* exposed to different H_2S donors from eggs till L4 larval stage: B) L-cysteine; C) Na_2SO_3; D) GYY4137; E) Mesna; F) AP39; * denotes a $p<0.05$ according to a One-Way ANOVA followed by a Tukey‘s post-hoc of the same values plotted as a bar graph.

Having observed that H_2S and sulfide-related metabolites are elevated alongside dysregulation of mitochondrial sulfide-oxidizing enzymes in *vhl-1* mutants, we hypothesized that increased H_2S levels might be sufficient to induce the body length shortening observed in these animals. To test this, we supplemented worms from the L1 to L4 larval stages (48h) with different H_2S donors. All tested donors significantly reduced body length in wild-type animals but failed to do so in *vhl-1* mutants (**Figure 10B–F**). Notably, mitochondrial-targeted delivery of H_2S via AP39 also shortened body length in wild-type worms but had no effect in *vhl-1* mutants (**Figure 10F**), indicating that mitochondrial H_2S elevation alone is sufficient to induce this phenotype — except in *vhl-1* mutants, where H_2S levels are already elevated.

We also tested Mesna, a drug commonly used in nephrology and known to interact with endogenous thiol pools such as glutathione (GSH) and cysteine [265266]. Although Mesna is not a classical H_2S donor, it similarly reduced body length in wild-type animals but required considerably higher concentrations than conventional donors to achieve this effect (**Figure 10D–E**). In contrast, *vhl-1* mutants remained unaffected by Mesna treatment, reinforcing the idea that elevated basal H_2S in these animals renders them insensitive to further increases.

Protein	Age			p<0.05?		
	D1	D6	D15	D1	D6	D15
CTH-1	0.684916	0.834509	1.083726	yes	no	no
CTH-2	0.824734	0.82245	1	no	no	no
CBS-1	1.011853	0.852635	0.707597	no	yes	yes
GOT-1	1.062896	0.812816	0.560972	no	no	yes
MPST-1	0.948684	1.297739	1.487614	no	yes	yes
CYSL-1	1.290562	1.180993	0.72951	yes	yes	yes
CYSL-2	3.768525	7.43844	2.460583	yes	yes	yes
CYSL-3	1.836552	3.033535	1.448942	yes	yes	yes
CYSL-4	3.567714	4.694593	1.654047	yes	yes	yes
SQRD-1	11.0196	7.422988	2.16295	yes	yes	yes
ETHE-1	3.572663	2.408275	0.856188	yes	yes	yes
GOT-2	0.775393	1.278099	2.156961	no	yes	yes
MPST-3	6.516061	4.248637	1.153486	yes	yes	yes
SUOX-1	0.801625	0.651574	0.60794	yes	yes	yes

Metabolite	Age	p<0.05?
	D1	
H_2S	1.93	yes
Cystathionine	1.22	no
Cysteine	2.15	yes
Glutathione	1.96	yes
Glutathione-SSH	2.05	yes
Cysteine-SSH	1.74	yes

Table 22. Fold change of H_2S metabolism proteins and related metabolites altered in *vhl-1* mutant worms.

Differential expression of proteins related to H_2S metabolism in *vhl-1* mutants compared to WT**.** Values for protein expression are presented in fold change. Values highlighted in blue indicate downregulation, while values highlighted in red indicate upregulation. All colored values indicate statistically different values in the comparison *vhl-1* x WT ($p<0.05$). Values for metabolites concentration are presented in percentage of WT levels.

A focused analysis of all mitochondrial proteins detected in our dataset, reveals two clusters when comparing WT, *vhl-1*, and *sqrd-1;vhl-1* animals (**Figure 11A**): cluster 1 is heterogeneous, but is mostly composed of proteins upregulated in *vhl-1* mutants compared to WT. Cluster 2 is composed of proteins downregulated in *vhl-1* mutants compared to WT in a *sqrd-1* dependent manner. In order to explore the impact these changes in the proteome may have in mitochondrial physiology, we employed MONARCH enrichment analysis (*C. elegans* phenotypes) to analyze each cluster separately. MONARCH identifies which known *C. elegans* phenotypes are statistically overrepresented, linking gene expression to observable traits. Both clusters enriched

for mitochondrial phenotypes related to mitochondrial composition, oxygen consumption, ATP levels, and differential stress resistance, phenotypes already known to us, such as those related to pace of development and hypoxia resistance, were also enriched (**Figure 11B-C**). We also performed a subcellular localization enrichment analysis (COMPARTMENTS) to have a better idea if one or more mitochondrial complexes would be changed in *vhl-1* mutants. COMPARTMENTS can determine where the encoded proteins are likely to act within the cell. Cluster 1 showed an enrichment of the L-cysteine desulfurase complex, which is important to Fe-S cluster formation and sulfur availability (**Figure 11D**). Complex I (NADH dehydrogenase) and complex IV (cytochrome C oxidase) were enriched in cluster 2 (**Figure 11E**), meaning proteins belonging to these mitochondrial respiratory complexes were downregulated in *vhl-1* mutants in a *sqrd-1* dependent manner.

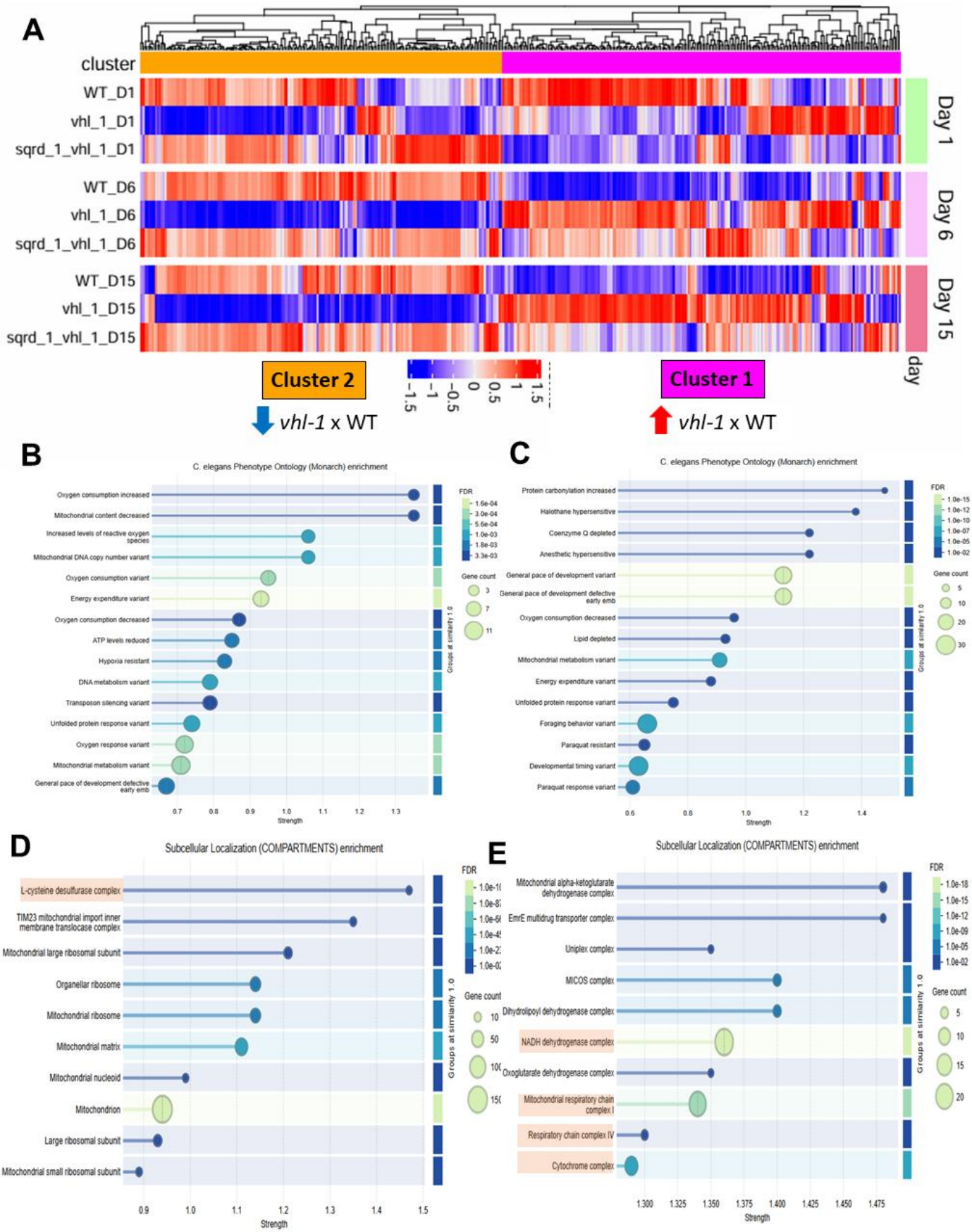

Figure 11. Loss of *vhl-1* impacts mitochondrial proteome in a *sqrd-1* dependent manner.

A) Heatmap with clustering for all regulated mitochondrial proteins detected in the proteome when comparing *vhl-1* mutants x WT in all three different timepoints.

continued on next page

Cluster 1 encompasses mostly upregulated proteins (red arrow up) in *vhl-1* mutants compared to WT that are not *sqrd-1* dependent. Cluster 2 encompasses mostly downregulated proteins (blue arrow down) in *vhl-1* mutants compared to WT that are *sqrd-1* dependent; B) MONARCH enrichment analysis (*C. elegans* phenotypes) for Cluster 1 proteins regulated at any of the three timepoints; C) Monarch pathway enrichment analysis (*C. elegans* phenotypes) for Cluster 2 proteins regulated at any of the three timepoints; D) COMPARTMENTS enrichment analysis for Cluster 1 proteins regulated across any of the three timepoints. H_2S related term is highlighted; E) COMPARTMENTS enrichment analysis for Cluster 2 proteins regulated across any of the three timepoints. Mitochondrial function related terms are highlighted. All enrichment analysis were done on STRING, and the terms presented are the top for each analysis ordered by FDR (statistical strength), where the x-axis indicates strength and the y-axis indicates term similarity, while the circle size indicates the number of proteins included in each term.

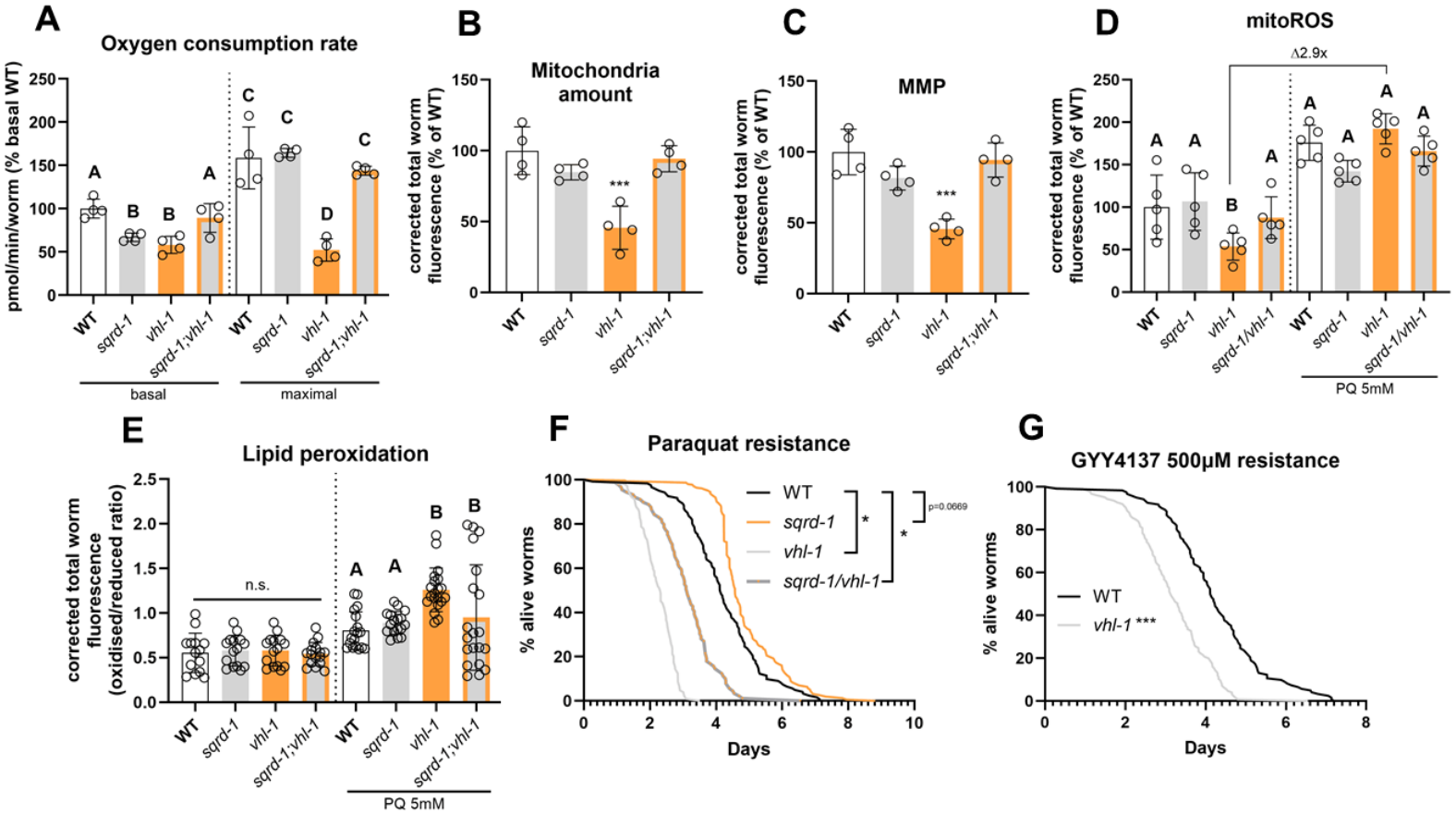

Figure 12. The *vhl-1(ok161)* mutation reduces mitochondrial function and *C. elegans* sensitivity to oxidative stress and excessive H_2S in a *sqrd-1* dependent manner.

A) Oxygen consumption rate at basal (left) or maximal (right) levels for D1 adult worms (20-30 worms measured concurrently per biological replicate, n=5); B) Mitochondrial amounts (Mitotracker fluorescence) measurement for D1 adult worms (15 worms per biological replicate, n=4); C) Mitochondrial membrane potential (MMP) (TMRE fluorescence normalised by mitotracker fluorescence) measurement for D1 adult worms (average fluorescence of 10-15 worms per biological replicate, n=4); D) Mitochondrial reactive oxygen species (mitoSOX fluorescence) measurement for D1 adult worms. Δ; denotes fold change between the indicated groups (average fluorescence of 10-15 worms per biological replicate, n=5); E) Lipid peroxidation (BODIPY C11 green/red fluorescence ratio) measurement for basal (left) and stressed (right, paraquat 5mM added at D0 timepoint) D1 adult worms (5-8 worms per biological replicate, n=4); F) Survival on paraquat (5mM) was measured from D0 of age onward. Number of worms per group across 3 biological replicates: WT=244, *sqrd-1*=312, *vhl-1*=208, *sqrd-1;vhl-1*=178; G) Survival on GYY4137 (500µM) from D0 of age and on. Number of worms per group across 2 biological replicates: WT=268, *vhl-1*=250; For figures A to E groups that are distinct ($p<0.05$, One-Way ANOVA, Tukey's post-hoc test) are highlighted by different letters on their top. Similar letters denote no statistically appreciable difference. For figured F and G *, *** denotes a $p<0.05$, and $p<0.0001$, respectively, according to Kaplan-Meier analysis and Logrank test.

Since our proteome enrichment analysis pointed to possible mitochondrial phenotypes, we proceeded to check whether *vhl-1* mutants would present general changes in mitochondrial function. To that we first measured oxygen consumption of D1 worms and indeed *vhl-1* mutants displayed reduced basal and maximal oxygen consumption (**Figure 12A**), a change that was dependent on *sqrd-1*, as the *sqrd-1;vhl-1* mutants were indistinguishable from WT animals in both basal and maximal respiration. We also identified that *vhl-1* mutants possess a reduced mitochondrial mass indicated by the fluorescent dye mitotracker (**Figure 12B**), a phenotype that is also *sqrd-1* dependent. Mitochondrial membrane potential (MMP), which was normalised by mitochondrial mass, was also reduced in *vhl-1* mutants in a *sqrd-1* dependent fashion (**Figure 12C**). Under basal conditions (non-stressed), D1 old mutant *vhl-1* worms show decreased amounts of mitochondrial reactive oxygen species in a *sqrd-1* dependent manner (**Figure 12D**, left). However, after paraquat stimulation, a known inducer of mitochondrial ROS, *vhl-1* mutant ROS levels were indistinguishable from those measured in WT animals and in *sqrd-1;vhl-1* double mutants (**Figure 12D**, right). When assessing ROS related damage, we observed that *vhl-1* mutants are not significantly different from WT animals under basal conditions regarding lipid peroxidation (**Figure 12E**, left), whereas under stress conditions vhl-1 and *sqrd-1;vhl-1* both display increased damage compared to WT animals (**Figure 12E**, right). In agreement to that, survival under paraquat was reduced for both *vhl-1* mutants and *sqrd-1;vhl-1* double mutants compared to WT, with *vhl-1* being the most sensitive to this stressor (**Figure 12F**). Interestingly, the loss of *sqrd-1* in the *vhl-1* background seemed to be more deleterious than the loss of *sqrd-1* in WT background (**Figure 12F**). Finally, we checked whether *vhl-1* would be differentially sensitive to mortality induced by high concentrations of H_2S, as H2S levels are already higher at baseline in this strain (**Table 22***)*. For that we exposed animals to 500μM of GYY4137 continuously, and indeed *vhl-1* mutants showed higher sensitivity than WT animals (**Figure 12G**).

4.4. Identification of downstream targets of *sqrd-1* that modulate lifespan and size in *vhl-1* mutants

In order to identify which downstream effectors of *sqrd-1* responsible for the modulation of lifespan and size in the *vhl-1* mutant background, we selected all proteins that were differentially regulated in *vhl-1* mutants compared to WT at all timepoints (D1, D6, and D15) always in a *sqrd-1* dependent manner. For that we focused on groups of proteins belonging to categories relevant to metabolic adaptation to hypoxia: Complex I and complex II (OXPHOS) and glycolysis; the H_2S mitochondrial catabolism; all glutathione-s-transferases and peroxidases detected in the our proteomic data, which are important cytoprotective agents and crucial against oxidative stress; and finally collagens and collagen modifiers (prolyl hydroxilases), which should play a role in body development, size, and structure (**Figure 13**). These proteins were selected based on literature available on such pathways (e.g. papers describing the specific processes here mentioned, such as H_2S catabolism and glycolysis [240,267], as well as on their listed names common to all proteins belonging to that class (e.g. *gst*-x for almost all described glutathione-s-transferases and *col*-x for the vast majority of the described collagen-encoding genes) as it is listed in their PDB entries, which are therefore directly searchable in our proteomic data tables. After separating all proteins into “regulated at least once (D1 or D6 or D15) and “regulated at all times” (D1, D6, and D15), we further filtered them by *sqrd-1*-dependent regulation (no difference between *vhl-1* and vhl-1;*sqrd-1* mutants) and obtained **Table 23**. In general, the proteins encoding for the complex I (e.g. NUO-4 and NUO-5), as well collagens (e.g. COL-8 and COL-149), were downregulated (**Table 23**). Most of the H_2S pathway (e.g. SQRD-1 and MPST-3), glycolysis (e.g. PCK-1 and LDH-1), glutathiones (e.g. GST-19, and GST-38) prolyl hydroxylases (e.g. PHY-2 and DPY-18) were upregulated. Regarding their regulation throughout the different timepoints, over half of all proteins belonging to the synthesis and catabolism of H_2S were regulated in every timepoint (**Figure 13**), with most being overexpressed except for SUOX-1 (**Table 22** and **Table 23**). Over 1/3 of all proteins detected that encode for a subunit of the mitochondrial complex 1 were also regulated at all timepoints, always downregulated (**Figure 13** and **Table 23**), with specially strong regulation at late timepoints (e.g. D6 and D15).

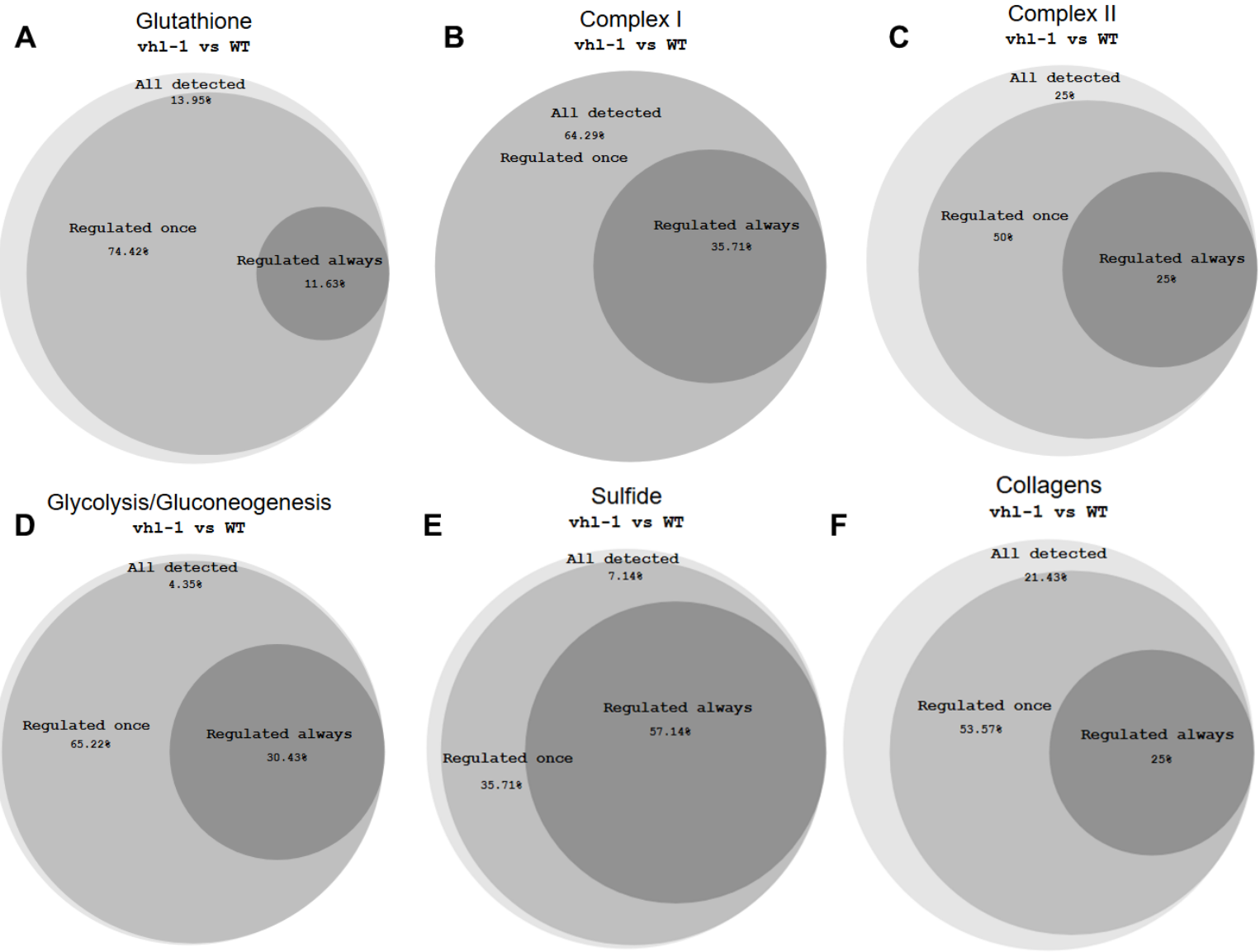

Figure 13. A considerable fraction of proteins from key pathways/groups critical for hypoxia adaptation are regulated in *vhl-1* mutants.

Venn diagrams for all groups of proteins display the intersection between: All proteins detected belonging to the category indicated above (outermost, light gray); The percentage of those proteins in that group that were regulated in at least one timepoint (D1 or D6 or D15) in *vhl-1* vs WT (center, gray); The percentage of those proteins that were regulated in all timepoints (D1, D6, and D15) in *vhl-1* vs WT (innermost, dark gray); “Complex 1” consisted of 28 proteins, “Complex II” consisted of 9 proteins, “Glycolysis” consisted of 23 proteins, “Glutathione” consisted of 43 proteins, “Collagens” consisted of 28 proteins.

	Protein	Age		
		D1	D6	D15
Complex I	NUO-2	0.957935	0.592546	0.604159
	NUO-4	0.933033	0.568803	0.590906
	NUO-1	0.920826	0.564091	0.588046
	NDUF-5	0.911301	0.562139	0.602904
	NUO-5	0.90125	0.590906	0.538867
Collagen	COL-138	0.410655	0.647521	0.347239
	COL-124	0.394747	0.199436	0.13453
	COL-149	0.425432	0.290176	0.196554
	COL-8	0.432568	0.314907	0.167473
	COL-140	1.66094	0.485654	0.153467
Complex II	SDHB-1	1.213354	1.149495	0.925946
	SDHA-1	1.310393	1.17121	0.892547
	SUCL-1	0.855002	0.695923	0.516557
Sulfide	SQRD-1	11.0196	7.422988	2.16295
	MPST-3	6.516061	4.248637	1.153486
	SUOX-1	0.801625	0.651574	0.60794
Glycolysis	PCK-1	4.106758	3.228804	5.950455
	LDH-1	1.702907	1.462057	1.126619
	ALDO-1	1.45599	1.540074	1.098854
	GPI-1	1.164734	1.133669	1.108032
	PYK-1	0.871154	0.89131	0.777546
Glutathione	GST-19	24.86423	20.82147	1.345367
	GST-38	2.812786	1.864773	0.837406
	GST-6	1.443929	1.499	0.853818
	GST-16	1.373636	1.806253	0.836826
	GST-7	1.22264	1.479388	1.233707
PHD	EGL-9	1.860899	1.777685	1.175276
	PHY-2	3.213176	2.426707	1.480413
	DPY-18	1.943962	2.2253	1.358486

Table 23. Regulated proteins in *vhl-1* mutants across all three timepoints in a *sqrd-1* dependent manner.

Top regulated proteins across all timepoints in *vhl-1* x WT and reversed in the double *sqrd-1;vhl-1* mutant (altered in the same direction in *vhl-1* x WT and *vhl-1* x *sqrd-1;vhl-1*) in key categories for hypoxia protection and according to our enrichment analysis. Values are presented as fold change relative to WT animals.

After checking for their availability in the Ahringer RNAi library, and based on the literature available, we selected the candidates of each category that were most likely to modulate lifespan and/or size in our screen. Compared to their respective L4440 RNAi control group, both *nuo-4* and *nuo-5* knockdowns induced lifespan increase in all genotypes but *vhl-1* mutants (**Table 24**). The knockdown of the same genes also induced body length decrease in all genotypes, except for *vhl-1* mutants (**Table 25**), which is in line with the fact that these proteins are already downregulated in *vhl-1* mutants. Meanwhile, the knockdown of *mpst-3, ldh-1, pck-1,* and *phy-2* all decreased

lifespan of *vhl-1* mutants and increased their body size (**Table 24** and **Table 25**). *mpst-3* can produce H_2S, *ldh-1* and *pck-1* are part of the glycolytic pathway, and *phy-2* is an important collagen modifier. *gst-19* knockdown shortened lifespan without affecting body length. *gst-19* encodes a glutathione S-transferase (**Table 24** and **Table 25**). The knockdown of such genes promoting lifespan decrease specifically in *vhl-1* is in line with the fact that these genes were all strongly upregulated throughout *vhl-1* life cycle according to our proteomic data (**Table 23**). Notably, single knockout of both *col-8* and *col-149*, as well as their double knockdown was able to shorten *vhl-1* mutants.

	Mean lifespan (days)										
RNAi	L4440	*nuo-4*	*nuo-5*	*col-8*	*col-149*	*sdha-1*	*mpst-3*	*ldh-1*	*pck-1*	*gst-19*	*phy-2*
GENOTYPE											
WT	16.1	**18.2***	**18***	16.2	16.5	16.5	16	15.5	15	16.3	16.4
sqrd-1	15.9	**17.6***	**17.8***	16.1	15.8	15.7	15.7	16	15.2	15.8	15.5
vhl-1	19.2	19.4	18.9	18.7	19	18.6	**15.5***	**17.1***	**14.1***	**17***	**17.6***
sqrd-1;vhl-1	16.3	**18***	**18.2***	16.5	16.5	16.1	15.8	15.9	15.6	16.6	16

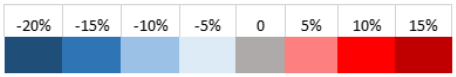

Table 24. RNAi screen for *sqrd-1*-dependent *vhl-1* lifespan regulators in *C. elegans* identifies the downregulation of *nuo-4* and *nuo-5* as potential downstream effectors.

Mean lifespan expresses the average survival in days for the displayed genotypes in specific RNAi clones targeting the specified genes. Red and its shades indicate positive lifespan regulation, while blue and its shades indicate a negative lifespan regulation. * indicates a $p<0.05$, at least, for the comparison between the indicated group and its respective L4440 control, according to the Kaplan-Meier analysis and Logrank test.

	Mean body length (µm)											
RNAi	L4440	*nuo-4*	*nuo-5*	*col-8*	*col-149*	*sdha-1*	*mpst-3*	*ldh-1*	*pck-1*	*gst-19*	*phy-2*	*col-8+col-149*
GENOTYPE												
WT	251±5	**224±6***	**230±3***	244±2	248±5	248±6	231±6	244±1	241±3	225±2	248±12	239±9
sqrd-1	213±4	**197±5***	**199±1***	209±3	204±5	215±3	205±7	220±9	210±8	208±6	211±7	210±7
vhl-1	165±6	168±2*	161±3*	162±3	169±4	170±6	**188±6***	**180±2***	**184±3***	168±4	**190±7***	161±2
sqrd-1;vhl-1	207±10	**189±6***	**191±3***	**188±2***	**182±4***	210±4	208±3	205±9	208±5	209±2	205±11	**172±8***

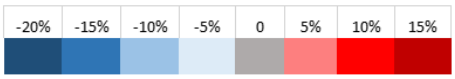

Table 25. RNAi screen for *sqrd-1*-dependent *vhl-1* body length regulators in *C. elegans* identifies the downregulation of *nuo-4* and *nuo-5* as potential downstream effectors.

Mean body length of L1 larval stage worms is displayed in µm for the indicated genotypes grown (P0 was fed on RNAi, measurement is carried in F1 L1 larvae) in different RNAi clones targeting the specified genes. Red and its shades indicate positive lifespan regulation, while blue and its shades indicate a negative lifespan regulation. * indicates a $p<0.05$, at least, for the comparison between the indicated group and its respective L4440 control, according to a One-way ANOVA followed by a Tukey post-hoc.

4.5. Characterization of Mesna, a lifespan and stress resistance inducer, as a potential new H_2S modulator

Aiming to identify promising chemical modulators of H_2S/sulfide metabolism, we tested three different sulfur-containing molecules, which – due to their natural origin or their status as approved drugs – appeared promising for future therapeutic use. Two of these had been studied before as H_2S donors (DATS and DADS), while the third, Mesna, was expected based on literature reports to influence H_2S metabolism. Different concentrations of these compounds were initially tested for their capacity to induce lifespan extension (data not shown), which allowed us to define a range in which continuous exposure caused no mortality. Wild-type nematodes show delayed development when grown under hypoxia, which is evident from their later progression to the reproductive adult stage. We observed no impact on this phenotype in WT worms treated with DATS or DADS, whereas Mesna led to a slight but significant developmental acceleration (**Figure 14A**).

To further investigate the effects of Mesna on hypoxia adaptation, we examined protein homeostasis, another phenotype strongly influenced by oxygen availability and redox status. Hypoxia and associated metabolic changes can impair protein folding and clearance, leading to increased aggregation of misfolded proteins [268]; thus, polyglutamine (polyQ) aggregation is a well-established readout of cellular stress resistance under low oxygen conditions [269]. Using *unc-54*::Q35::YFP transgenic animals, we found that 600µM and 1.2 mM Mesna significantly reduced the number of YFP foci under 0.1% O_2 (**Figure 14B**). Furthermore, animals preconditioned with 6mM Mesna survived longer under oxidative stress induced by paraquat (**Figure 14C**), and prolonged exposure to 6 mM Mesna extended *C. elegans* lifespan (**Figure 14D**).

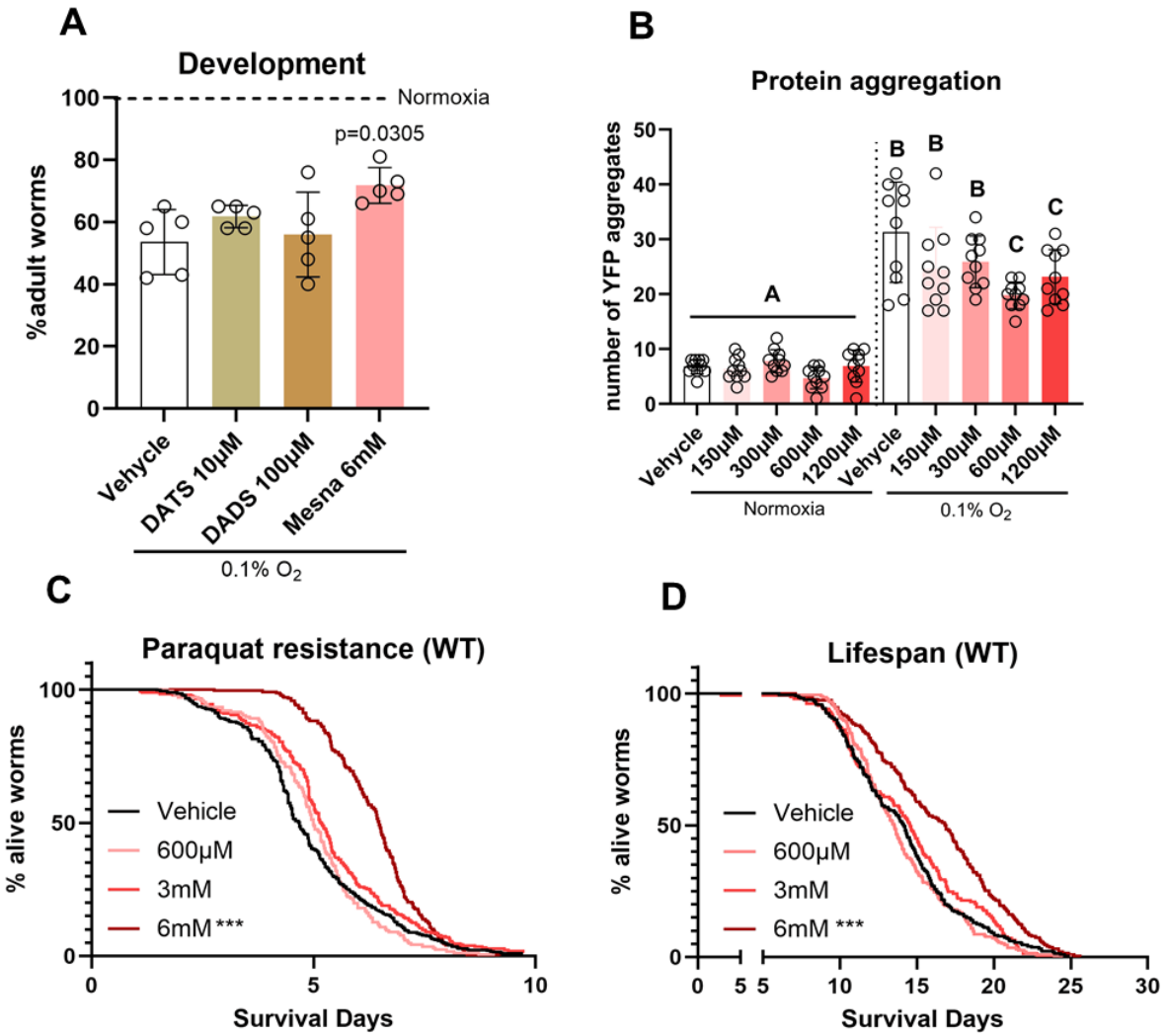

Figure 14. Mesna protects *C. elegans* against hypoxia related damage, oxidative stress, and extends its lifespan.

A) Development is shown as the percentage of worms reaching adulthood (presence of discernible eggs in the uterus) while growing under 0.1% O_2 for 24h from L4 larval stage, at the time where 100% of animals grown under normoxia reached adulthood; B) PolyQ (*unc-54p*::Q35::YFP) aggregation in the muscle of *C. elegans* grown under under 0.1% O_2 for 24h from L4 larval stage; C) Survival of WT worms pre-exposed to Mesna and then kept on paraquat (5mM) from day 0 onward. Number of worms per group across 4 biological replicates: Vehicle=391, 600µM=166, 3mM=251, 6mM=238; D) Lifespan curve of WT worms lifelong exposed to Mesna. Number of worms per group across 2 biological replicates: Vehicle=213, 600µM=194, 3mM=153, 6mM=190. ** and *** indicate a $p<0.01$, and $p<0.001$, respectively, according to a One-way ANOVA followed by a Tukey post-hoc for Figures A and B, or the Kaplan-Meier analysis and Logrank test for Figures C and D, all when comparing each group to its Vehicle control group.

Since lifespan extension by HIF-1 activation was dependent on the sulfide-quinone oxidoreductase *sqrd-1*, we went on to address the question whether Mesna and *sqrd-1* would interact regarding this phenotype. While protection against paraquat induced death by Mesna was not mediated by *sqrd-1*, the dose-response curve indicates that the loss of *sqrd-1* instead further potentiates the protective effect of Mesna (**Figure 13A**). While this was the case in a short-term damage setting, prolonged exposure to 6mM Mesna shortens lifespan in *sqrd-1* mutants (**Figure 15B**). Indeed, *sqrd-1* mutants are more sensitive to Mesna in comparison to WT, which is displayed by their increased mortality when acutely (24h) exposed to high concentrations of Mesna (**Figure 15C**).

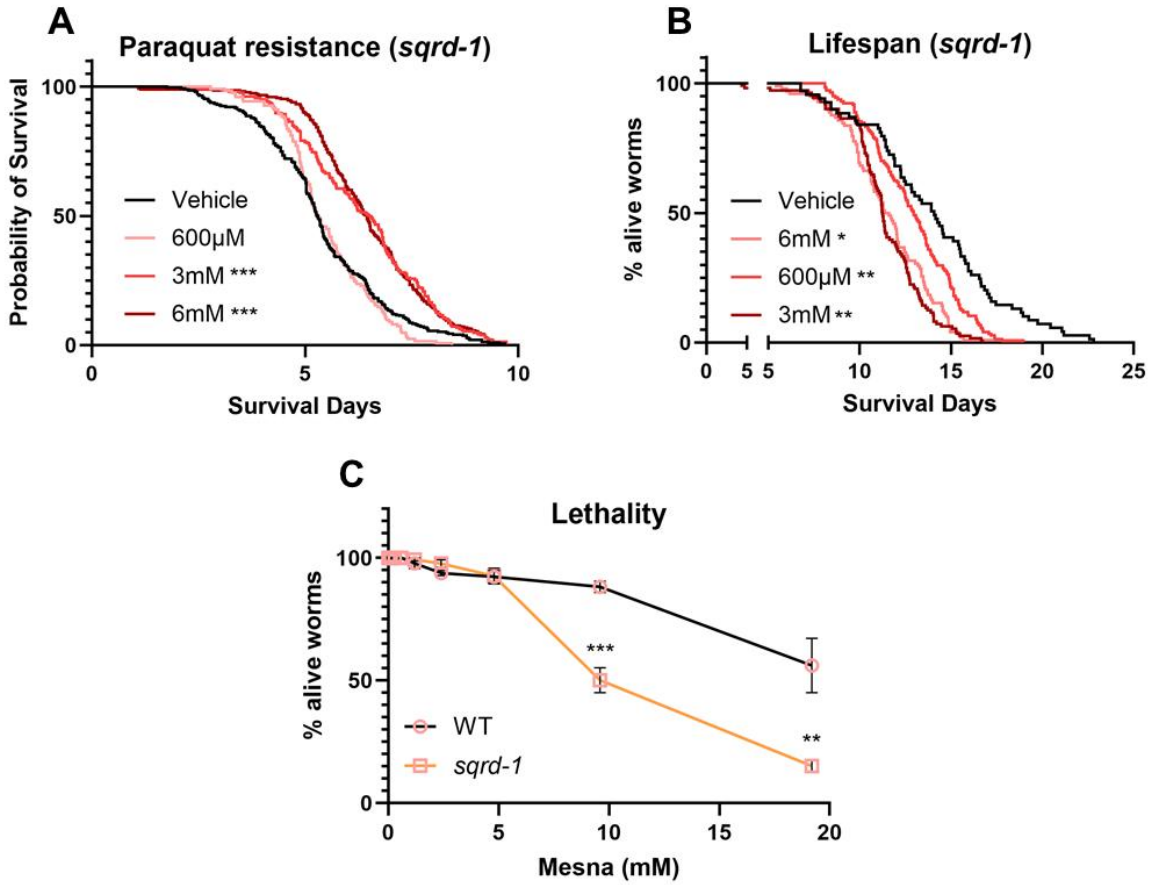

Figure 15. *sqrd-1(mr28)* mutation enhances protection against paraquat induced by Mesna but makes long-term exposure to it toxic.

A) Survival of *sqrd-1* mutants pre-exposed to Mesna and then kept on paraquat (5mM) from D0 of age onward. Number of worms per group across 3 biological replicates: Vehicle=288, 600µM=122, 3mM=205, 6mM=278; B) Lifespan curve of *sqrd-1(mr28)* mutants worms lifelong exposed to Mesna. Number of worms per group across 2 biological replicates: Vehicle=138, 600µM=288, 3mM=222, 6mM=196; C) Mortality curve following 24h exposure to growing concentrations of Mesna in both WT and *sqrd-1(mr28)* mutant worms. *, ** and *** indicate a $p<0.05$, $p<0.01$, and $p<0.001$, respectively, according to the Kaplan-Meier analysis and Logrank test for survival/lifespan when comparing each group to its own non-Mesna exposed control, or a T-student test matching equal concentrations for both *sqrd-1* and WT worms for the lethality.

Knowing *sqrd-1(mr28)* mutation modified Mesna's effect over stress resistance and lifespan, we tested whether its expression could be modulated by Mesna. We observed that mRNA levels of *sqrd-1*, as well as its protein levels were increased after L4 animals were exposed for 24h to Mesna (**Figure 16A-C**). We then went on to measure H_2S and sulfide related metabolites in WT and *sqrd-1* (mutants) after 24h of exposure to Mesna. While H_2S was increased after Mesna exposure (**Figure 16D**), neither GSH nor GSSH were changed (**Figure 16E** and **F**). Interestingly, *sqrd-1* mutants displayed high H_2S levels under basal conditions with no further increase after Mesna exposure (**Figure 16D**). Besides, in contrast to WT, GSH and GSSH were increased upon Mesna (**Figure 16E** and **F**). Finally, in order to obtain an insight regarding their antioxidative capacity, we assessed the ratio between reduced (GSH) and oxidized (GSSG) glutathione. *sqrd-1* mutants showed a decreased GSH/GSSG ratio that was increased by Mesna and the same change was induced by Mesna in wildtype worms (**Figure 16G**).

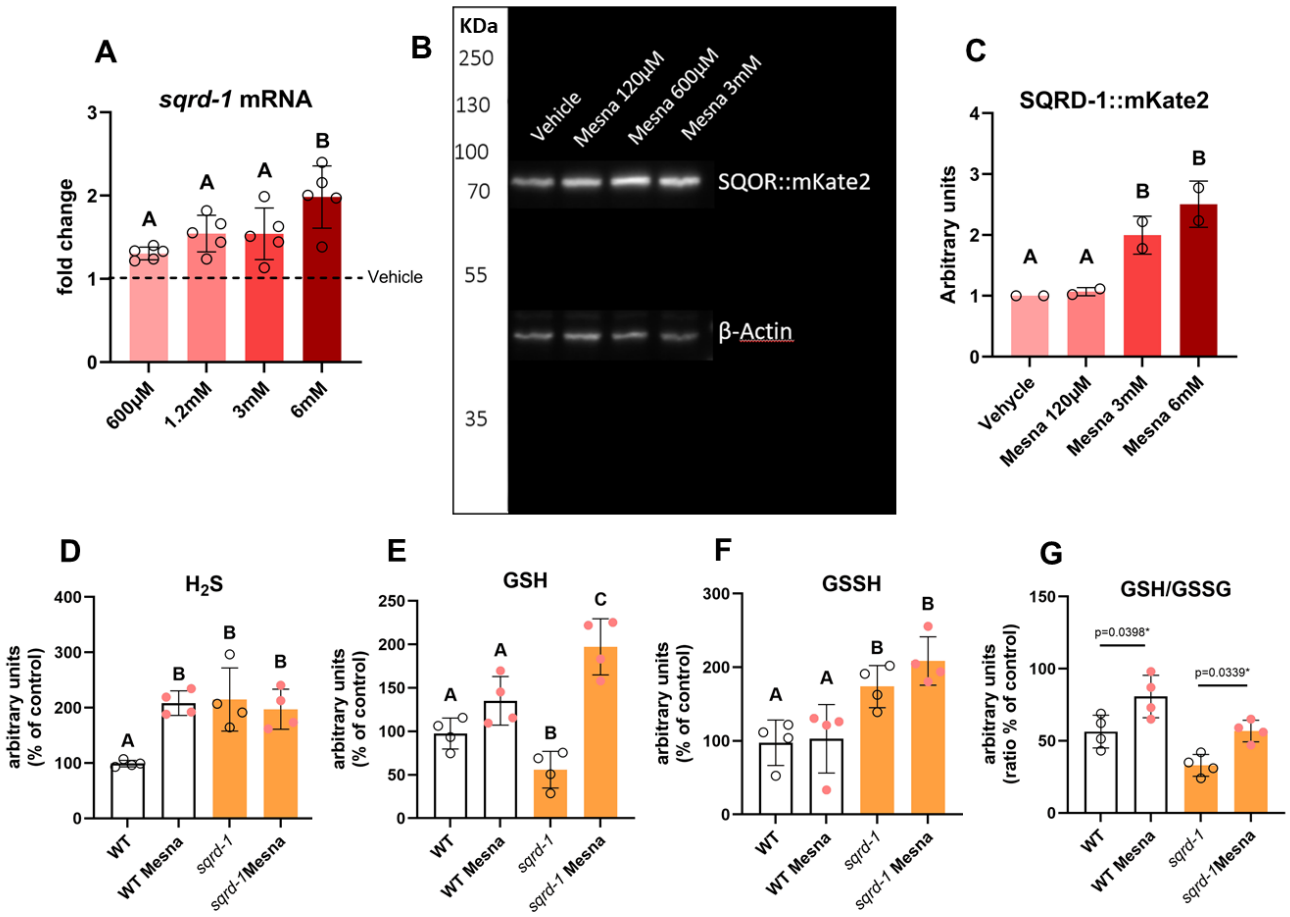

Figure 16. Mesna induces the expression of SQRD-1 and increases H_2S and sulfide-related metabolites in D1 old adult *C. elegans*

continued on next page

A) qPCR for *sqrd-1* mRNA measurement after 24h of Mesna exposure; B) Representative blotting of endogenous SQRD-1 tagged with mKate2 via CRISPR/Cas9 after 24h of Mesna exposure. SQRD-1::mKate2 fusion protein is approximately 79kDa; C) Densiometry measurement of SQRD-1::mKate blotting; D-F) H_2S, glutathione, glutathione persulfide, and glutathione/oxidized glutathione ratio measurement, respectively, in both WT and *sqrd-1(mr28)* mutants exposed to 6mM of Mesna for 24h. Values are presented in arbitrary units normalised by its own WT control (vehicle). * indicates a $p<0.05$ according to a One-way ANOVA followed by a Tukey post-hoc for *sqrd-1* mRNA expression measurement. For sulfide-related metabolites measurement, groups that are distinct (at least $p<0.05$, One-Way ANOVA, Tukey's post-hoc test) are highlighted by different letters on their top. On the other hand, similar letters denote no statistical difference.

Next, we tried to identify genes involved in the protective effect of Mesna against paraquat induced mortality in *C. elegans.* To this end, we handpicked other H_2S related mutants based on the literature [228,239,270,271] and tested whether they would display a different response to Mesna than those observed in WT and in *sqrd-1.* We were able to identify one negative regulator of Mesna protective effect against paraquat-induced death: *mpst-1* (**Figure 17D**). This gene encodes mercaptopyruvate sulfotransferase predicted to be involved in the synthesis of H_2S. This mutant was unresponsive to Mesna, dying regardless of any preconditioning concentration they were exposed to, while not showing any signs of reduced basal stress resistance.

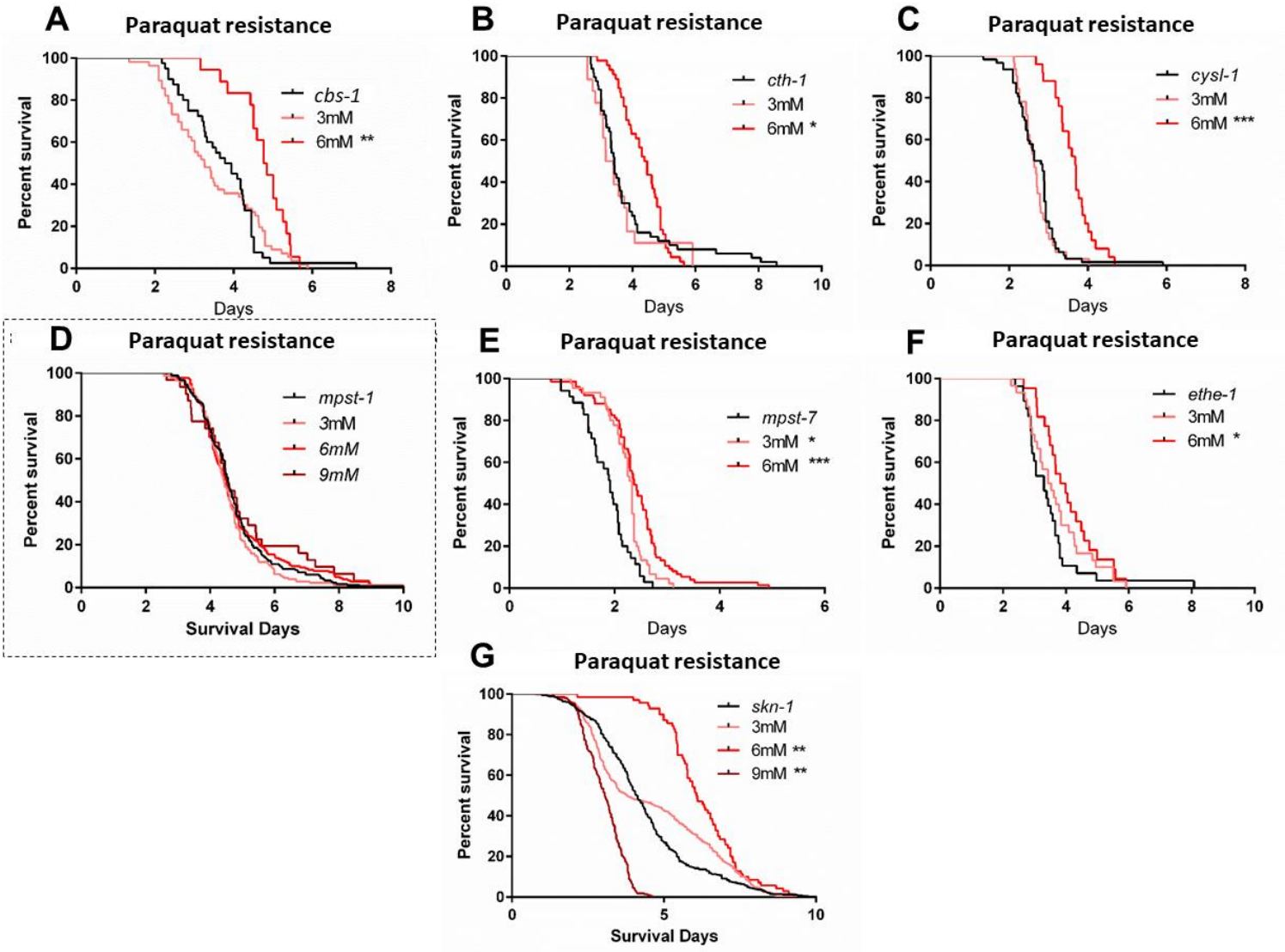

Figure 17. Screen identifies *mpst-1* as a regulator of oxidative stress resistance induced by Mesna exposure in *C. elegans*.

A-G) Lifespan curve of *cbs-1(gk5787), cth-1(ok3319), cysl-1(ok762), mpst-1(ok2040), mpst-7(gk514674), ethe-1(ok3755), skn-1(zu67)* mutants pre-exposed to 6mM Mesna and then kept on 5mM paraquat. *cbs-1, cth-1, cysl-1, mpst-7*, and *ethe-1* mutants were assessed over two biological replicates with at least n≥60 worms per replicate per group. *mpst-1* and *skn-1* mutants were accessed over three biological replicates with at least n≥60 worms per replicate per group. *, **, and *** indicate a $p<0.05$, $p<0.01$, and $p<0.001$, respectively, according to the Kaplan-Meier analysis and Logrank test for survival/lifespan when comparing each group to its own non-Mesna exposed control.

4.6. Mitochondrial respiration is a target for Mesna preconditioning against paraquat

To further elucidate mechanisms by which Mesna modulates stress resistance in *C. elegans,* we analyzed the proteome of worms preconditioned with Mesna 6mM for 24h,

washed with M9 1:10 volume 3x (1000 times dilution), and then exposed to paraquat for 48h (D2 of age). We chose the timepoint at which most animals were still alive, but already showed paraquat-induced changes in mortality (**Figure 14C**). Principal component analysis (PCA) of the proteomic (**Figure 18A**) data shows a clear separation of samples according to genotype and reveals the effect of Mesna treatment: WT, sqrd-1, and *mpst-1* cluster distinctly under PQ-only exposure, while Mesna addition creates different patterns of clustering among the strains. Upon Mesna exposure, all genotypes shift in a similar direction in the PCA space, suggesting that Mesna induces a consistent transcriptional response across genetic backgrounds. However, *sqrd-1* mutants shift more over dimension 1(Dim1) than WT and *mpst-1* mutant animals, consistent with the strength of the protective effect offered by Mesna to these different strains (*sqrd-1*>WT>*mpst-1*). When we selected all proteins that were differentially regulated only in the most protective conditions in comparison with paraquat only (WT and *sqrd-1* mutants treated with Mesna 6mM and exposed to paraquat vs only paraquat exposed animals of the same genotypes) we observed a molecular function enrichment of cytochrome C oxidase (Complex IV) proteins (**Figure 18B**). When we made that selection even more stringent and required these proteins to be regulated also under Mesna 3mM exposure against paraquat and excluded all proteins regulated in the only non-protective setting (*mpst-1* mutants under both Mesna concentrations and paraquat), we ended up with only 4 proteins, all subunits of the mitochondrial complex IV (**Table 23**).

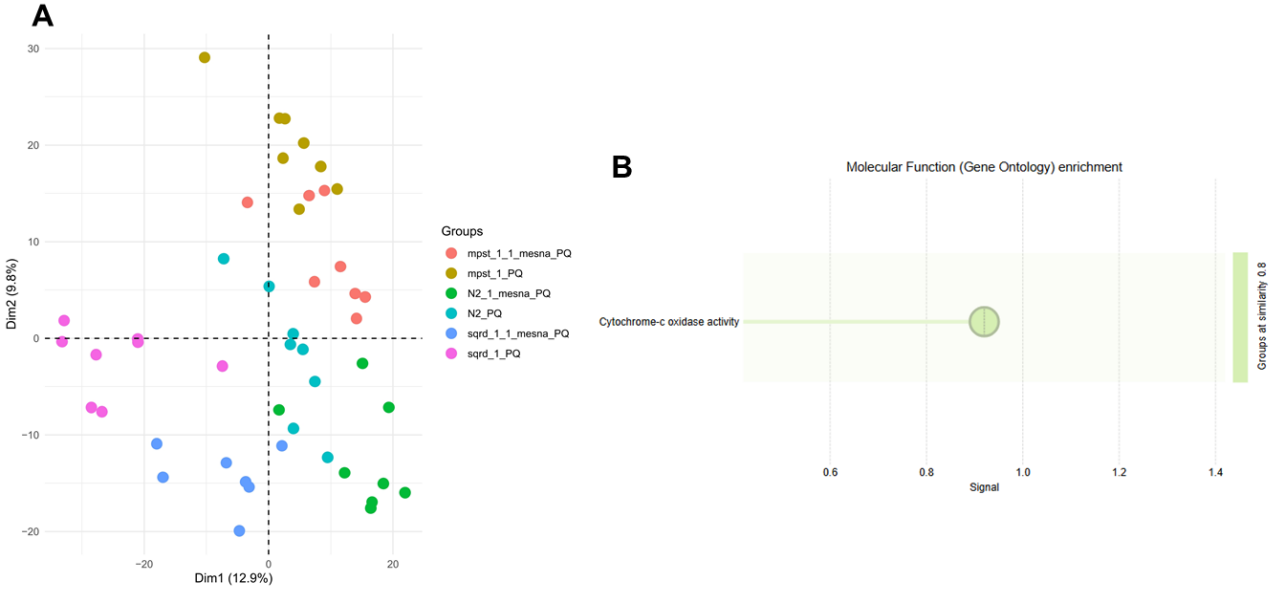

Figure 18. Analysis of the proteome of Mesna preconditioned WT, *sqrd-1*, and *mpst-1* mutant animals.

continued on next page

A) Principal component analysis of WT, *sqrd-1* and *mpst-1* mutants exposed only to 5mM of paraquat for 2 days (control) or the same genotypes preconditioned with Mesna 6mM and then exposed to 5mM of paraquat for 2 days; B) Molecular function enrichment analysis of all proteins regulated in the most protective conditions: Mesna 6mM preconditioning followed by paraquat in WT and *sqrd-1* mutants.

PROTEIN	WT M6 PQ vs WT PQ	WT M3 PQ vs WT PQ	SQ M6 PQ vs SQ PQ	SQ M3 PQ vs SQ PQ	MP M6 PQ vs MP PQ
COX-6B	1.222343769	1.019438631	1.64944173	1.475677563	1.084660716
COX-6C	1.265531917	1.133848997	1.453596143	1.426115945	1.080622614
COX-4	1.25237354	1.056546885	1.425891579	1.462641897	1.105954417
CTC-2	1.186569405	1.036943758	1.437139156	1.415880207	1.050732561
	*	-	*	*	-

Table 26. Cytochrome C oxidase (Complex IV) subunits are consistently upregulated where Mesna is able to induce protection.

Table 26 displays the four proteins that are regulated in all the cases where protection is afforded by Mesna preconditioning: 6mM in WT, 3mM and 6mM in *sqrd-1* mutants, and not regulated in *mpst-1* mutants after Mesna. Values are displayed as fold change. ‘’*”stands for significantly upregulated, while ‘’-‘’ stands for not regulated.

Having observed that the mode of regulation of different proteins belonging to the mitochondrial respiratory complex IV matched the observed phenotypes of the respective strains (**Figures 14C** for WT, **15A** for *sqrd-1*, and **17D** for *mpst-1*), we followed up on investigating whether mitochondrial function would be changed upon Mesna treatment. Indeed, matching our observation regarding downregulation of complex IV, mitochondrial membrane potential was severely reduced upon paraquat exposure, an effect that was in part prevented by Mesna 6mM preconditioning (**Figure 19A and B**). In the same direction, basal oxygen consumption rate was largely reduced by paraquat, something that Mesna 6mM preconditioning was partially able to prevent (**Figure 19C**).

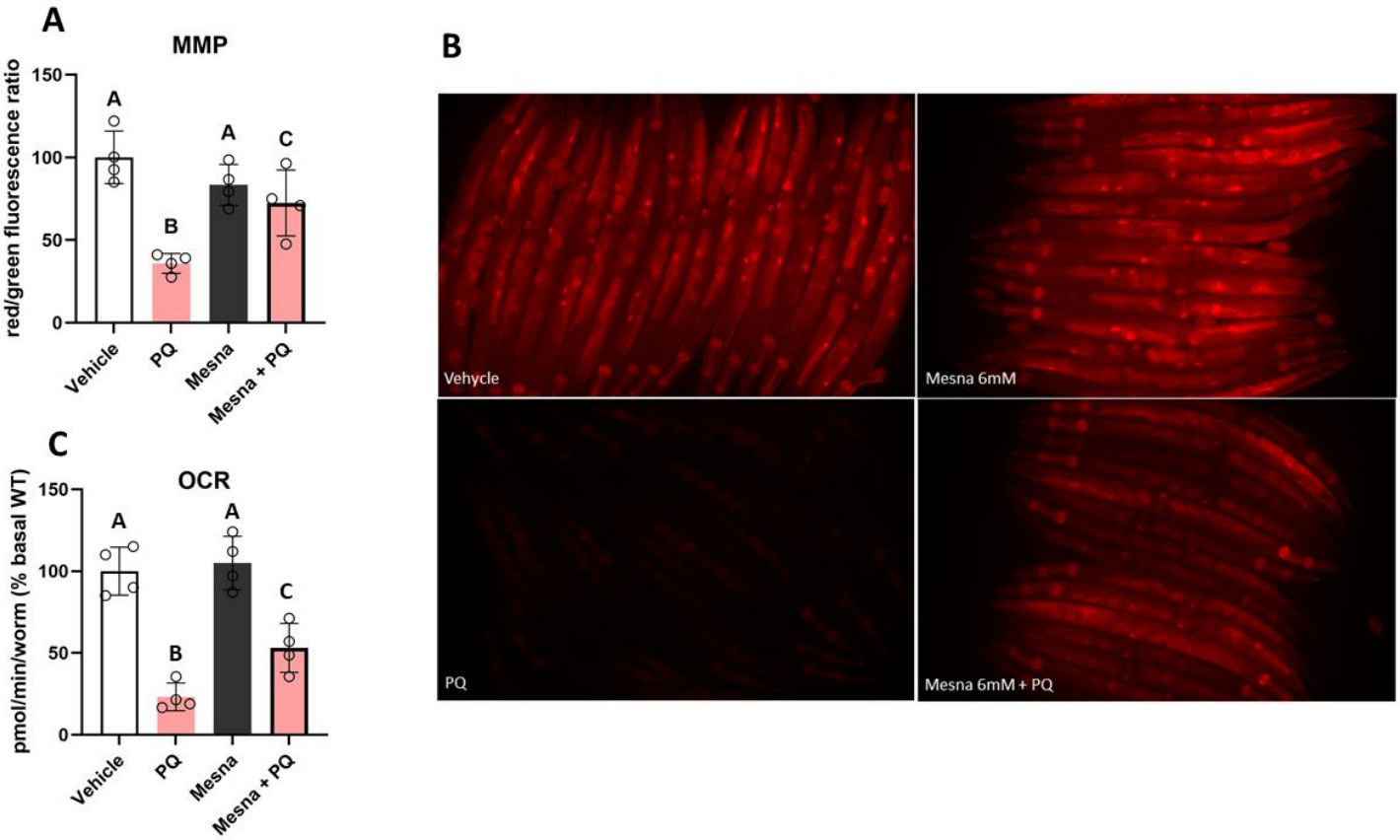

Figure 19. Mesna improves mitochondrial dysfunction induced by paraquat.

A) Mitochondrial membrane potential (MMP) after Mesna preconditioning followed by 48h of paraquat exposure. Each biological replicate consists of the average fluorescence of 10-15 animals (n=4); B) Representative images of TMRE staining; C) Basal oxygen consumption rate (OCR) after Mesna preconditioning followed by 48h of paraquat exposure. Each biological replicate consists of 20-30 animals that had their respiration measured concurrently, n=4) Groups that are distinct ($p<0.05$, One-Way ANOVA, Tukey's post-hoc test) are highlighted by different letters on their top. On the other hand, identical letters denote no statistically significant difference.

4.7. Characterization of Mesna's protective effect in kidney mIMCD3 cells

To assess whether Mesna could also protect mammalian kidney cells, we chose mIMCD3 cells as a model, once these cells are a stablished model to study the effects of IRI in the kidney [272]. We tested both preconditioning and postconditioning (**data not shown**) protocols with different concentrations of Mesna followed or preceded by 5mM of paraquat. Our group and others have shown that paraquat induces cellular death mainly via ferroptosis [273,274], which is highly relevant for IRI in the kidney [275]. mIMCD3 cells. Cell death was measured by exposing the cells to the membrane impermeable

dye DiYO-1, which becomes green once inside the cells. We settled for 600μM of Mesna in a preconditioning setting, where Mesna was added to the cell culture media and incubated with the cells for 24h, washed out with cell media, to then proceed with incubation with 5mM of paraquat. Preconditioning with 600μM of Mesna was enough to protect from cell death induced by paraquat (**Figure 20A** and **B**). Paraquat-induced mitochondrial ROS were also decreased by Mesna preconditioning (**Figure 20C** and **D**), as well as ROS-associated damage in the form of oxidized lipids (**Figure 20E** and **F**). In order to check for an interaction with the H_2S pathway, we transfected mIMCD3 cells with siRNA targeting *Sqor*, the mammal homologue of *C. elegans sqrd-1*. siRNA mediated knockdown was effective in decreasing Sqor protein levels, which was observable by diminished signal on immunofluorescence (**Figure 20A**), and decreased mRNA levels via qPCR (**Figure 20B**).

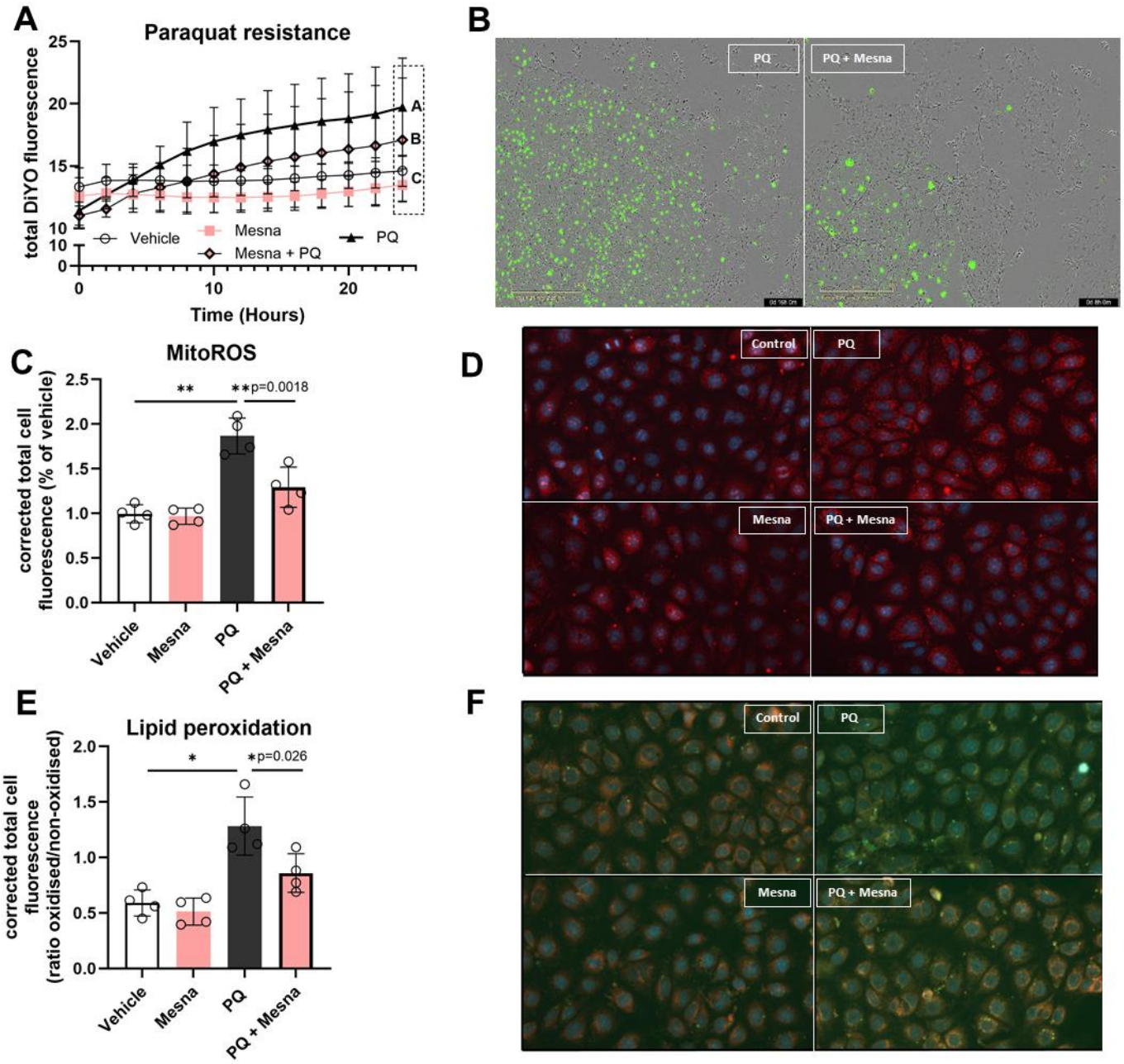

Figure 20. Mesna prevents paraquat induced oxidative damage and cell death in mIMCD3 cells.

A) Cell death after 24h of Mesna 600µM preconditioning followed by paraquat exposure for another 24h. Membrane impermeable dye DiYO-1 becomes fluorescent inside dying cells. At 24h timepoint statistical difference is represented by different letters; B) 8h timepoint representative image of mIMCD3 cells upon PQ only or PQ after Mesna preconditioning. Green fluorescence indicates cell death; C) Mitochondrial ROS (mitoSOX) measurement. Total cytosolic fluorescence (nuclear DAPI images are not included in the measurement) is normalised by area and background is subtracted; D) Representative image of mitoSOX stained mIMCD3 cells 8h after the beginning of paraquat exposure; E) Lipid peroxidation (BODIPY C11) measurement 8h after beginning of paraquat exposure. Total cytosolic fluorescence (nuclear DAPI images are not included in the measurement) is obtained through the ratio between green (oxidized) and red (non-oxidized) fluorescence, normalized by the area and subtracted from the background; F) Representative images of BODIPY C11 stained mIMCD3 cells; For paraquat resistance, groups that are distinct (at least $p<0.05$, One-Way ANOVA, Tukey's post-hoc test) are highlighted by different letters on their top. On the other hand, similar letters denote no statistically appreciable difference. * and ** indicate a $p<0.05$, and $p<0.01$, respectively, according to a One-way ANOVA followed by a Tukey post-hoc.

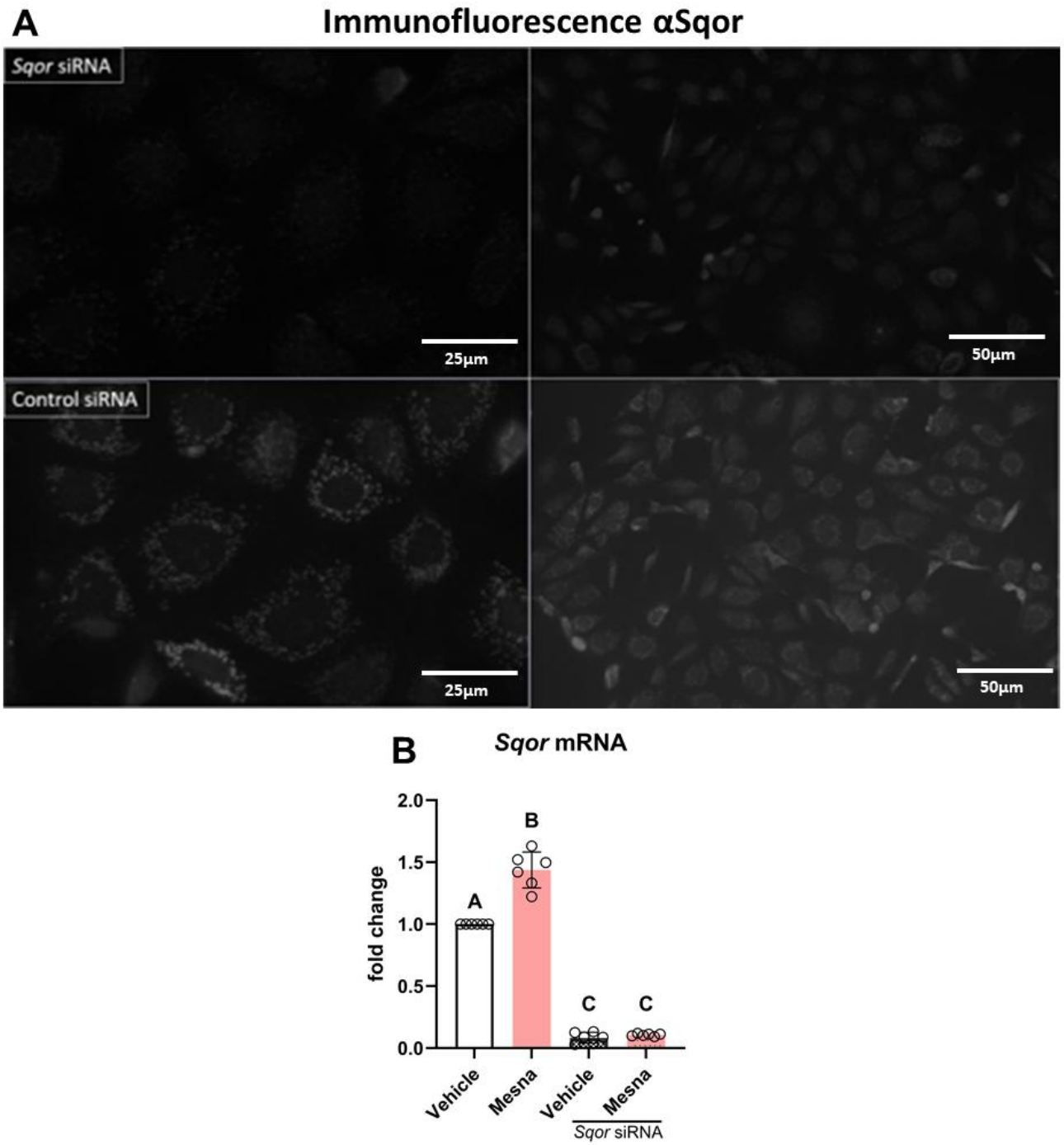

Figure 21. siRNA effectively knocks down *Sqor* in mIMCD3 cells.

A) Representative immunofluorescence of *Sqor* in mIMCD3 cells after 48 days of siRNA transfection. Top figures represent cells transfected with *Sqor* siRNA, while bottom figures represent cells that were transfected with control siRNA. Left images were obtained with an objective of 10x, while right images were done at 20x; B) *Sqor* mRNA expression measured by qPCR after 48h of transfection with *Sqor* siRNA or control siRNA followed by 24h of Mesna 600µM exposure; *** indicates a $p<0.001$, according to a One-way ANOVA followed by a Tukey post-hoc.

Knockdown of *Sqor* in mIMCD3 cells did not prevent Mesna from protecting mIMCD3 cells from paraquat-induced cell death, as Mesna + PQ group is similar to control under both control and *Sqor* siRNA transfected cells (**Figure 22A** and **B**). This is not entirely in line with our findings in *C. elegans*, where knockdown of *sqrd-1* induced further protection (**Figure 15A**). However, *Sqor* knockdown did sensitize mIMCD3 cells to higher concentrations of Mesna, as shown by increased cell death upon continuous exposure to 1.2mM and 2.5mM of it in comparison to cells transfected with control siRNA, where cell death induced by paraquat is higher in the *Sqor* siRNA transfected groups that were preconditioned with Mesna (**Figure 22C**). That is in line with our findings in *C. elegans*, where prolonged exposure to Mesna decreased lifespan in *sqrd-1* mutant animals compared to WT (**Figure 15B**). When we checked whether H_2S and persulfides would be changed after Mesna exposure, we saw an increase induced by Mesna in both H_2S and persulfide levels when compared to cells that were not preconditioned with Mesna (**Figure 22D** and **E**). Such effect persisted in paraquat exposed groups, even though no alteration was induced by paraquat itself when compared to control (**Figure 22D** and **E**). *Sqor* knockdown induced an increase in H_2S and persulfides by itself independently of Mesna and/or paraquat (**Figure 22D** and **E**) when compared to control siRNA transfected cells.

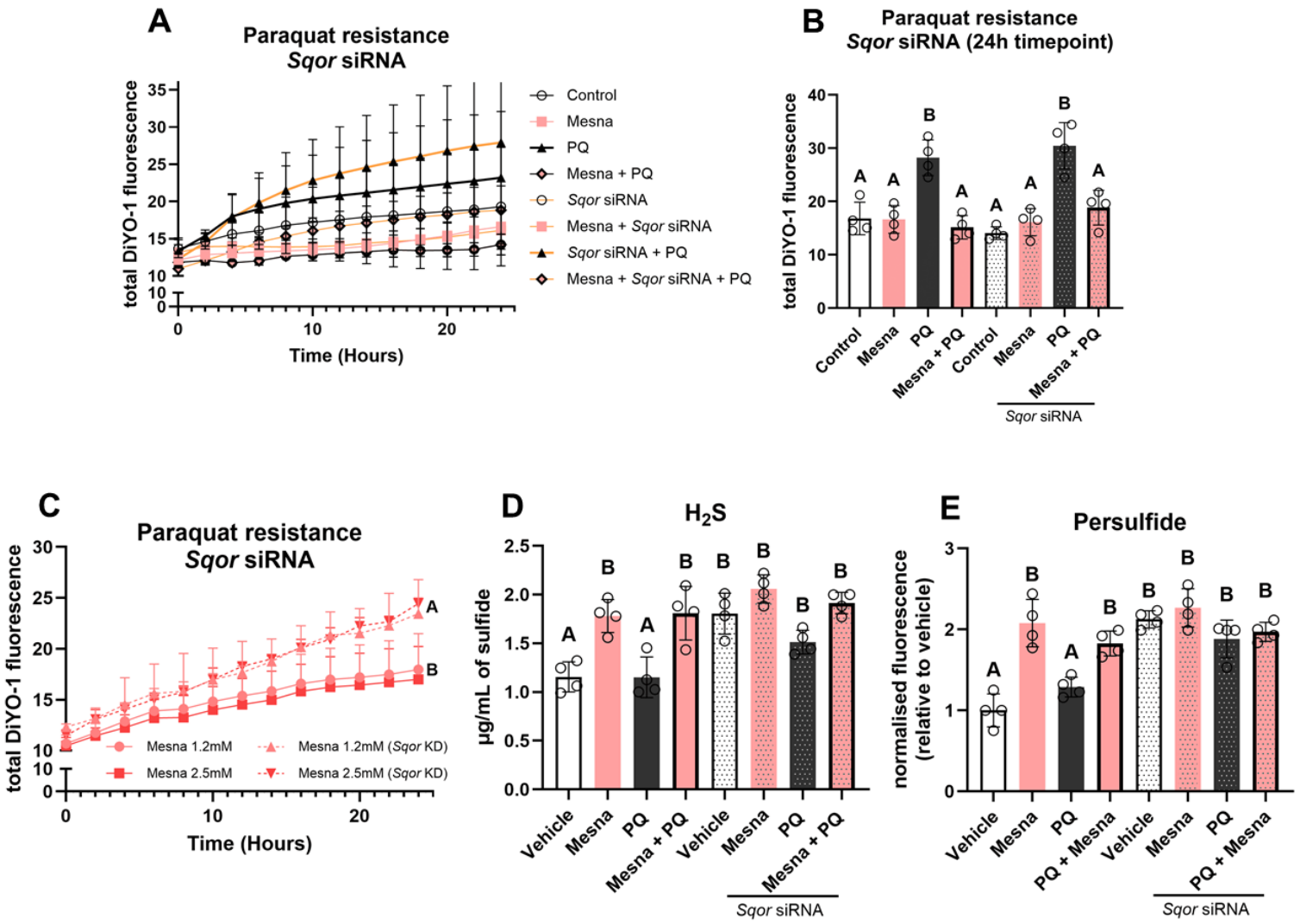

22. *Sqor* knockout does not impair Mesna protective effect or its capacity to induce sulfide and persulfide accumulation, but makes it more toxic in higher concentrations for mIMCD3 cells.

A) Cell death after Mesna 600µM preconditioning for 24h followed by 5mM paraquat exposure for another 24h in mIMCD3 cells transfected with either control siRNA or *Sqor* siRNA. Membrane impearmeable dye DiYO becomes fluorescent inside dying cells; B) 24h timepoint extracted from A; C) Cell death measured by DiYO-1 fluorescence after Mesna 1.2mM or 2.5mM for 24h followed by 5mM paraquat exposure for another 24h; D) H_2S measurement through fluorescent sulfide scavenging probe HSip-1 after 24h of Mesna 600µM preconditioning and 8h of paraquat exposure in mIMCD3 cells transfected with either control siRNA or *Sqor* siRNA; E) Persulfide measurement through fluorescent persulfide scavenging probe SSP4 after Mesna 600µM preconditioning and 8h of paraquat exposure in mIMCD3 cells transfected with either control siRNA or *Sqor* siRNA; Groups that are distinct (at least $p<0.05$, One-Way ANOVA, Tukey's post-hoc test) are highlighted by different letters on their top. On the other hand, similar letters denote no statistically appreciable difference according to a One-way ANOVA followed by a Tukey post-hoc.

To check if the protection induced by Mesna was impinging on reversing mitochondrial function alterations induced by paraquat-induced oxidative stress, we measured the mitochondrial membrane potential and ADP/ATP ratio. While Mesna preconditioning alone induced an increase in MMP in comparison to non-Mesna exposed control

(**Figure 23A**), Mesna preconditioning could not protect from the paraquat-induced MMP decrease, as Mesna plus PQ group is equal to the PQ-only group (**Figure 23A**). Important to notice is that FCCP, a known mitochondrial uncoupler and a positive control for apoptosis-induced cell death, lead to membrane potential decrease, just like paraquat did. MMP increase induced by Mesna preconditioning was dependent on Sqor, as its increase was prevented by *Sqor* knockdown (**Figure 23A**). These findings were not in line with those in *C. elegans*, where Mesna did not change MMP by itself but did reverse PQ-induced reduction in MMP (**Figure 19A** and **B**). Ultimately, while Mesna induced Sqor-dependent increase in MMP might be related to some of the other phenotypes we observed (e.g. increased H_2S and persulfide – **Figures 22D** and **E** [276]), an increase in mitochondrial membrane potential seems to not be pivotal to the protection Mesna affords against paraquat-induced cell death.

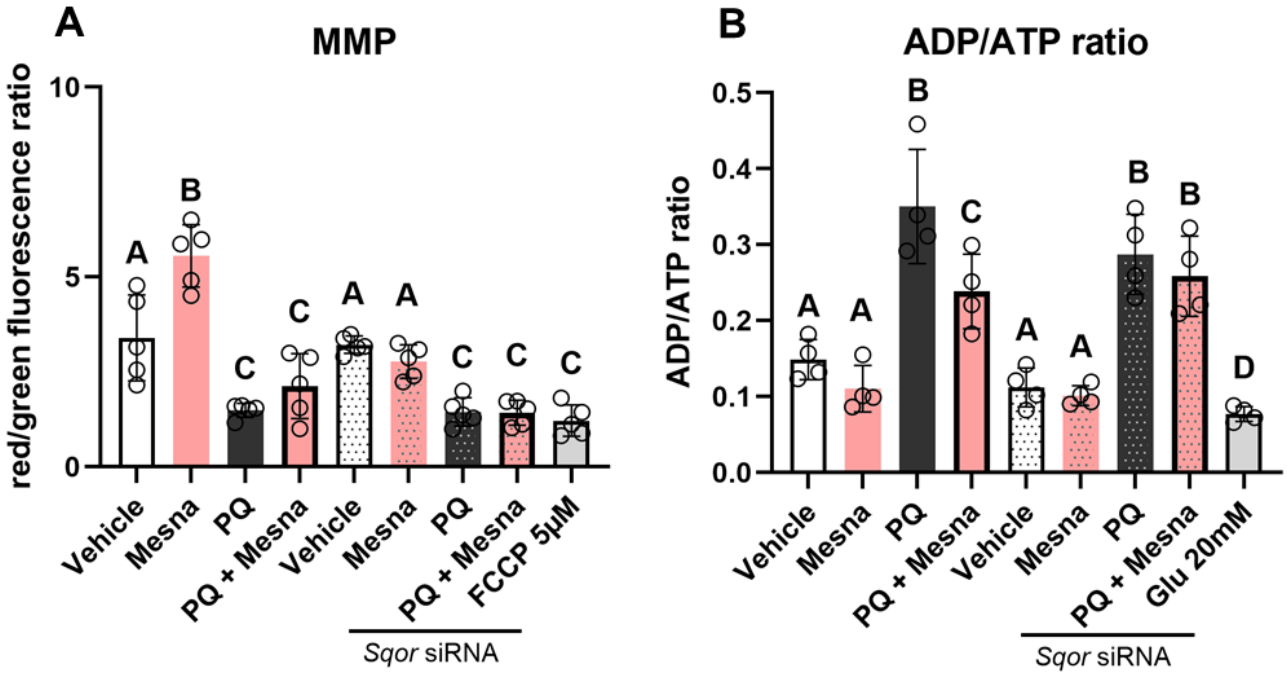

Figure 23. Mesna impacts mitochondrial function and interacts with Sqor in the setup of paraquat induced damage in mIMCD3 cells.

A) Mitochondrial membrane potential measurement measured by fluorescent JC-1 probe, which accumulates in its charged state inside polarized mitochondria, after Mesna 600μM preconditioning and 8h of paraquat 5mM exposure (before massive cell death starts to happen) in mIMCD3 cells transfected with either control siRNA or *Sqor* siRNA; B) ADP/ATP ratio measured after Mesna 600μM preconditioning for 24h followed by 8h of paraquat 5mM exposure in mIMCD3 cells transfected with either control siRNA or *Sqor* siRNA; Groups that are distinct (at least $p<0.05$, One-Way ANOVA, Tukey's post-hoc test) are highlighted by different letters on their top. On the other hand, similar letters denote no statistically appreciable difference.

Regarding the ratio ADP/ATP, which is closely tied to the mitochondrial membrane potential [277], supplementation of the media with 20mM of glucose served as a positive control for ratio decrease. Mesna did not induce any change by itself when compared to non-Mesna exposed control, but it was able to reverse paraquat-induced increase in ADP/ATP ratio, an effect that was *Sqor* dependent, since no change was observed in the cells where Sqor had been knocked out (**Figure 23B**). Overall, this suggests that while ATP and MMP increasing after Mesna preconditioning are Sqor dependent, but they do not count towards the protection against paraquat-induced cell death afforded by Mesna preconditioning. We concluded that from the lack of dependence on Sqor for survival (Figure 22A), and the dependence on Sqor for both MMP increase and ADP/ATP ratio decrease after Mesna preconditioning (**Figures 23A** and **B**).

5. Discussion

5.1. Identification of *sqrd-1* as a body length and lifespan regulator in *vhl-1(ok161)* mutants

Our previous data had characterized a reported phenotype of *vhl-1(ok161)* mutants as *hif-1* dependent (**Figure 6A-C**), besides showing that *vhl-1;hif-1* double mutants (salmon) replicates clustered in between WT (pink), revealing their bigger similarity wild-type animals than to single *vhl-1* (yellow) or *hif-1* (green) mutants regarding the way their transcriptomic data clusters (**Figure 6D**). This matches not only our data on body length, but also previously published data on *vhl-1* extended lifespan and its dependency on *hif-1* [223]. While oxygen availability has been described to regulate body size [278,279], *vhl-1* mutants grown under normoxia are short. At the same time, *egl-9* mutants, which also induces HIF-1 activation/nuclear localization, have not been reported to induce any changes in body size or development, which suggests body length change to be somewhat specific to *vhl-1* knockout. Curiously, HIF-1 overactivation can also lead to enlarged liver and spleen size [280], and obesity [281], an effect that was accompanied by decreased mitochondrial content and respiration.

While aiming to characterize an unexpected phenotype, short body length, we selected a number of genes that were regulated in *vhl-1* mutants in a *hif-1* dependent manner (**Table 21**). We observed the biggest size increase in *vhl-1* mutants upon *sqrd-1* knockdown (EV 156µm x *sqrd-1* 178µm, **Figure 7A**). *sqrd-1* encodes for the sulfide quinone oxidoreductase, a mitochondrial protein essential for the oxidation of H_2S into persulfides (mostly glutathione persulfide) [282]. While described before for being a target for HIF-1 induced transcriptional activation upon H_2S exposure, *sqrd-1* had never been reported for regulating *C. elegans'* body length. Our data was further substantiated by crossing *vhl-1* mutants with *sqrd-1(mr28)* mutants, which had been previously characterized for its increased sensitivity to H_2S [240], yielding equally longer *sqrd-1;vhl-1* double mutants (**Figure 7C** and **D**). *sqrd-1(mr28)* allele is the result of a C>T substitution, yielding hypomorphic mutants that, likely, retain some SQRD-1 activity. These mutants are only less sensitive to H_2S-induced mortality, whereas the null *sqrd-1(tm3378)* allele is almost completely non-resistant to H_2S [240], with a mortality close to 100% at high H_2S levels. We chose to work with the *mr28* allele because when crossing *vhl-1(ok161)* worms with *sqrd-1(tm3378)* worms we observed a drastic reduction in fertility/hatching in the resulting double mutants, what would compromise further experiments (**Data not shown**).

An important consideration when evaluating body length in *C. elegans*, is development in itself, meaning how long it takes for the animals to reach each of its larval stages (L1, L2, L3, and L4), as well as its adult form. Even though we did observe delayed development in *vhl-1* mutant worms (**Figure 7E**), that was only statistically significant for the number of worms reaching adulthood by 72h of life. We did not see a distinguishable change on the number of worms reaching neither L2/L3 stages by 24h, nor the L4 larval stage by 48h (**Figure 7E**). On top of that, we confirmed that size difference persists in equally staged adult worms (**Figure 7F**), something that had been observed before by another study [233]. This further reinforces the notion that developmental timing is not confounding our observations regarding body length.

Literature reporting the involvement of H_2S and/or enzymes involved in its synthesis or catabolism with body size regulation are scarce and divergent: while two studies on *Poecilia mexicana* and *Poecilia sulphuraria* (Poeciliidae) grown on naturally occurring sulfidic springs were smaller than its counterparts grown on normal non-sulfidic waters [283284], another study in *Bombyx mori* (silkworm) showed the opposite, with increased

weight and body size after exposure to 7,5µM of NaHS [285]. For the studies that observed reduced body size, another factor in play was the very hypoxic nature of such springs, which often correlates to H_2S concentration in water environments [283]. This suggests that hypoxia itself, independent of sulfide, can drive the selection or induction of smaller body size as an adaptive mechanism to reduce metabolic demand under limited oxygen availability. Overall, both studies that found reduced body size proposed that high H_2S could favor the lower metabolic demand associated with a smaller body size, but also pointed out that hypoxia alone can have the same effect.

Body size and lifespan have been previously linked, to varying degrees, in *C. elegans* [286287], as well as in other species such as dogs and mice [288,289,290], and even in humans, where a weak but significant negative correlation has been reported between height and mean lifespan [291]. In *C. elegans*, some lifespan extending mutations also cause marked shortening of the body, such as feeding defective *eat-2* and *pha-2* [287]. Because of that, we considered the extended lifespan phenotype of *vhl-1* could be linked to its shortened body length, and, potentially, changed in the *sqrd-1;vhl-1* double mutant. Indeed, *sqrd-1* mutation completely ablated lifespan extension induced by the *vhl-1* mutation (**Figure 7F**). Besides *hif-1*, which is the major downstream effector of *vhl-1* mutation [223], only *egl-9(sa307)* and *rhy-1(ok1402)* mutations/knockdown had been shown to suppress lifespan extension in this mutant [228]. Conversely, *sqrd-1* had also never been shown to regulate lifespan neither by itself nor in another genetic background.

5.2. Proteomic analysis depicts stark differences between *vhl-1* mutants and *sqrd-1;vhl-1* double mutants

In an initial analysis, we observed a clear separation between *vhl-1* mutants and all the other phenotypes for D1 and D6 (**Figure 8A** and **B**), and a less noticeable similar pattern for D15 (**Figure 8C**). Interestingly, *sqrd-1;vhl-1* double mutants clustered closer to WT than to *sqrd-1* or *vhl-1* single mutants across all ages (**Figure 8A-C**), which is compatible with their observed lifespan being undistinguishable from WT, as well as their size being fairly close to WT worms during earlier larval stages (**Figure 7C** and **D**).

5.2.1. A number of *hif-1*/hypoxia related changes in the proteome of *vhl-1* mutants are reversed by *sqrd-1* mutation

KEGG pathway enrichment of *sqrd-1*–dependent proteins differentially regulated in *vhl-1* mutants compared to wild type highlighted several metabolic pathways central to hypoxia adaptation, including the tricarboxylic acid (TCA) cycle, glycolysis, and oxidative phosphorylation [292,293,195]. These processes reflect the metabolic shift from aerobic oxidative phosphorylation to anaerobic glycolysis that typically accompanies hypoxic responses. Notably, a substantial proportion of proteins regulated downstream of HIF-1 also depended on *sqrd-1*, indicating that sulfide oxidation influences a significant fraction of the HIF-1–mediated proteomic changes in *vhl-1* mutants — a relationship not previously described. Although *vhl-1* mutants were maintained under normoxic conditions, a clear HIF-1 activation signature was present, and fewer than half of the differentially regulated proteins were strictly HIF-1–dependent. This observation suggests that secondary metabolic adaptations occur downstream of HIF-1 activation and that *vhl-1* deletion also elicits HIF-1–independent effects. Among the known functions of pVHL/VHL-1 unrelated to HIF regulation is its ability to directly interact with hydroxylated collagen IV, a role that contributes to proper extracellular matrix (ECM) deposition [294,295]. Loss of this function may explain, at least in part, the reduced body size observed in *vhl-1(ok161)* mutants. (**Figure 6A-C**).

5.3. Altered mitochondrial function and increased hydrogen sulfide metabolism are *sqrd-1* dependent changes in *vhl-1* mutants

Analysis of *sqrd-1*–dependent proteins in *vhl-1* mutants revealed strong enrichment of metabolic pathways associated with hypoxia adaptation, including the tricarboxylic acid (TCA) cycle, glycolysis, oxidative phosphorylation, and fatty acid metabolism [296]. These results indicate that *sqrd-1* influences mitochondrial remodeling downstream of HIF-1 activation. Interestingly, sulfur metabolism–related proteins were enriched predominantly at early adulthood, suggesting that modulation of sulfide oxidation is an early and transient component of this response. Additionally, the upregulation of ribosomal and RNA metabolism proteins aligns with the increased translational demand associated with hypoxic stress [190,297].

5.3.1. Mitochondrial hydrogen sulfide detoxification is upregulated

HIF-1 activation reduced oxidative phosphorylation, which likely promoted H_2S accumulation by limiting mitochondrial sulfide oxidation, as SQOR/SQRD-1 required oxidized ubiquinone as its electron acceptor [52]. SQOR/SQRD-1, MPST-3, and ETHE-1 were upregulated as a compensatory response to increased H_2S, whereas SUOX-1 was downregulated (**Table 22**), suggesting that sulfite (SO_3^{2-}) was preferentially converted to thiosulfate (SSO_3^{2-}) via MPST-3 rather than to sulfate (SO_4^{2-}) via SUOX-1. The co-upregulation of SQRD-1, ETHE-1, and MPST-3 in the context of elevated H_2S supported the idea that MPST-3 acted predominantly as a sulfotransferase (TST). Its presumed substrate, 3-mercaptopyruvate, was expected to derive from GOT-2, although their expression dynamics did not coincide. The increased persulfide levels we measured were consistent with a sulfur-buffering route (H_2S → SQRD-1 → GSSH → MPST-3 → SSO_3^{2-}) emerging from HIF-1 activation and reduced mitochondrial respiration. A complementary buffering mechanism could have involved the sustained overexpression of CYSL-2/3/4. While only CYSL-2 had been characterized in detail and was able to produce H_2S under cyanide exposure [240], these proteins were homologous to sulfotransferases and β-substituted amino acid synthases [298–300], suggesting that they could have redirected excess sulfur into alternative metabolites, acting as sulfur sinks.

In *vhl-1;sqrd-1* double mutants, impaired SQOR activity likely compromised persulfide formation, as shown by GSSH and cysteine persulfide elevation in *vhl-1* mutants being *sqrd-1* dependent (**Figure 10A**), and was associated with the absence of MPST-3 upregulation, pushing cells toward a low-production, low-clearance state. In addition, cytosolic H_2S production appeared globally reduced and declined with age (GOT-1 and CBS-1 decreased), whereas mitochondrial capacity increased with age (GOT-2 increased). These age- and compartment-specific shifts were *sqrd-1* dependent, as they were not observed in the *vhl-1;sqrd-1* double mutants.

5.3.2. Exogenous H_2S is enough to induce body length shortening in WT worms

We believe our findings here point to *vhl-1* mutants having an established mechanism to detoxify H_2S that makes them insensitive to the acute to this 48h exposure to a

number of donors. This would likely include SQRD-1, ETHE-1, and possibly MPST-3 too (**Figure 10A**). Finally, this is somewhat in line with a previously mentioned study in that fish grown in sulfidic springs adapt to it by becoming shorter [283284], and another study that found out that mutation in the H_2S producing enzyme *cth-2*, arrests the development of worms grown in Actinobacteria, while exogenous H_2S was able to restore their rate of growth [301].

5.3.3. *vhl-1* mutation promotes changes in mitochondrial proteome and function

Our proteomic analyses indicated that *vhl-1* mutation altered multiple mitochondrial metabolic pathways and upregulated sulfide detoxification over time, prompting us to examine mitochondrial function more closely. Hierarchical clustering of all mitochondrial proteins revealed two major clusters (**Figure 11A**): Cluster 1 included proteins upregulated in *vhl-1* mutants but not in the *vhl-1;sqrd-1* double mutants, while Cluster 2 contained proteins downregulated in *vhl-1* and restored to wild-type levels in the double mutants. Phenotype enrichment for these clusters predicted alterations in oxygen consumption, mitochondrial content, ROS levels, ATP production, paraquat sensitivity, and coenzyme Q amounts (**Figure 11B, C**).

Because SQRD-1 activity is linked to electron flow through the respiratory chain and depends on the redox state of the CoQ pool [302], we further examined subcellular enrichment patterns. Cluster 1 was enriched for the L-cysteine desulfurase complex, which synthesizes Fe–S clusters for mitochondrial proteins such as succinate dehydrogenase (Complex II) [303] (**Figure 11D**), while Cluster 2 was enriched for NADH dehydrogenase (Complex I) and cytochrome c oxidase (Complex IV) (**Figure 11E**). HIF-1 activation is known to downregulate Complexes I and IV, the main oxygen consumers, whereas Complex II upregulation may reflect a compensatory mechanism under elevated H_2S oxidation. In such conditions, the CoQ pool becomes more reduced (ubiquinol, $CoQH_2$), decreasing SQRD-1 activity; Complex II operating in reverse could regenerate CoQ by reducing fumarate to succinate [304].

Consistent with these predictions, *vhl-1* mutants showed significantly lower basal and maximal oxygen consumption rates (OCR) compared to wild type, while *vhl-1;sqrd-1* double mutants exhibited OCR comparable to wild type (**Figure 12A**). *sqrd-1* mutants

also showed reduced basal OCR but normal maximal respiration. MitoTracker staining revealed a reduced mitochondrial content in *vhl-1* mutants (**Figure 12B**), and TMRE measurements indicated a decreased mitochondrial membrane potential (MMP), which was restored in the double mutants (**Figure 12C**). Because MMP was calculated relative to mitochondrial mass, its reduction was likely even greater than the raw signal indicated. These findings suggested that *vhl-1* mutation reduced both mitochondrial abundance and function, consistent with known outcomes of HIF-1 activation. H_2S accumulation might further contribute to these effects, as it potently inhibits Complex IV and suppresses respiration [305].

Given the strong link between mitochondrial function, ROS, and longevity [306,307,308], we next examined mitochondrial ROS (mitoROS). Basal mitoROS levels were lower in *vhl-1* mutants than in wild type or double mutants, but paraquat treatment eliminated this difference, and *vhl-1* mutants showed an almost threefold increase in mitoROS upon stimulation (**Figure 12D**), indicating heightened sensitivity to oxidative stress. Lipid peroxidation assays confirmed this: while no differences were observed under basal conditions, paraquat exposure caused greater lipid peroxidation in *vhl-1* and *vhl-1;sqrd-1* mutants than in wild type (**Figure 12E**). In line with this, *vhl-1* mutants were more sensitive to paraquat-induced mortality than wild type or double mutants (**Figure 12F**). These findings challenge the assumption that HIF-1 activation universally enhances stress resistance. Although *vhl-1(ok161)* mutants are heat-shock resistant [309], a previous study with the same strain has shown that indeed *vhl-1(ok161)* mutants are more prone to die under continuous exposure to 1 and 4mM of paraquat [310], mirroring our findings.

We hypothesize that impaired mitochondrial function contributes to this heightened sensitivity, as paraquat toxicity relies on mitochondrial superoxide production via Complex I and depletion of CoQ [311,312]. H_2S accumulation may further exacerbate stress by stalling electron transport. Indeed, while short-term H_2S exposure reduced body size only in wild type (**Figure 10B–F**), continuous exposure to GYY4137 caused *vhl-1* mutants to die ~25% earlier than wild type (**Figure 12G**). Mutation of *sqrd-1* restored most mitochondrial parameters in the *vhl-1* background, including paraquat survival, likely by reducing sulfide oxidation capacity and downregulating H_2S-producing enzymes such as MPST-3 and CYSLs (**Figure 10A**, **Table 22**). This

adaptation restored mitochondrial function, as seen in OCR and MMP, but at the cost of reduced lifespan (**Figure 7F**).

5.4. Downstream targets of *sqrd-1* link mitochondrial metabolism to lifespan and body size in *vhl-1* mutants

The *sqrd-1(mr28)* mutation markedly altered the phenotype of *vhl-1(ok161)* mutants, restoring lifespan, body size, mitochondrial function, and proteomic profiles to near wild-type levels. To understand this broad effect, we examined proteins from pathways relevant to these traits, including mitochondrial complexes I and II, sulfide metabolism, glycolysis, glutathione metabolism, and collagen synthesis (**Figure 13**). Most proteins in these categories were regulated at least once, and a subset was consistently altered across all time points in a *sqrd-1*–dependent manner (**Table 23**). These proteins reflected major phenotypes of *vhl-1* mutants, such as complex I downregulation, mitochondrial sulfide detoxification upregulation (with SUOX-1 as an exception), enhanced glycolysis, increased glutathione S-transferases, higher levels of prolyl hydroxylases (including EGL-9), and reduced collagen expression, consistent with their shorter body size.

To test functional contributions to size and lifespan, we performed RNAi knockdowns of ten candidate genes (*nuo-4*, *nuo-5*, *col-8*, *col-149*, *sdha-1*, *mpst-3*, *ldh-1*, *pck-1*, *gst-19*, and *phy-2*). Several knockdowns (*mpst-3*, *ldh-1*, *pck-1*, *phy-2*) shortened lifespan while increasing body size (**Table 24** and **25**). Knockdown of complex I components *nuo-4* and *nuo-5* extended lifespan in all genotypes except *vhl-1* mutants and reduced body size (**Table 24** and **25**). This agrees with previous findings that loss of *nuo-4* or *nuo-5* extends lifespan [313,314] and induces reduced body size and slower development [314,315], and with broader evidence that partial complex I inhibition increases lifespan. Broader evidence also shows that partial inhibition of mitochondrial respiratory complexes — particularly complex I — extends lifespan in *C. elegans* [316] , and complex I abundance correlates with longevity in calorie-restricted mice [317]. However, heterozygous deletion of *Ndufs2* did not extend lifespan or reduce sensitivity to complex I inhibition in mice, likely due to unaltered complex I activity [318]. Our results suggest that *nuo-4* and *nuo-5* act downstream of *sqrd-1*, as no additive effects were observed in *vhl-1* mutants, and effects in *sqrd-1;vhl-1* double mutants bypassed the

requirement for *sqrd-1*. Restoration of complex I function likely contributes to mitochondrial recovery, with transcript reduction alone partially extending lifespan but not to the extent seen in *vhl-1* mutants. This link between complex I, lifespan, and body size appears specific to this context, indicating that lifespan-regulating pathways act upstream of size determination in *vhl-1* mutants.

Knockdown of glycolysis/gluconeogenesis enzymes *pck-1* (PEPCK-C) and *ldh-1* also shortened lifespan while increasing body size (**Table 24** and **25**). Previous work showed that *pck-1* overexpression shortens lifespan and knockdown reduces it in both wild type and long-lived *eat-2* mutants [319]. Although significant effects were limited to *vhl-1*, wild-type animals showed a similar non-significant trend. *pck-1* is highly upregulated in *egl-9(sa307)* mutants, and *pck-1(ok2098);egl-9(sa307)* animals phenocopy *hif-1* mutants in hypoxia and oxidative stress resistance without suppressing lifespan extension [226]. These findings highlight the importance of the metabolic shift from respiration to glycolysis under hypoxia or HIF-1 activation, particularly for stress resistance. Moreover, paraquat resistance in *egl-9* mutants depends on *pck-1* and can be restored by phosphoenolpyruvate supplementation, suggesting distinct regulatory outcomes for *egl-9* and *vhl-1*. The absence of size phenotypes in *egl-9* mutants further supports HIF-1–independent functions of VHL-1.

Although no previous study has linked MPST-3 to lifespan, its knockdown shortened *vhl-1* mutant lifespan (Table 24, 25), consistent with reports that *mpst-1(ok2040)* deletion reduces lifespan, reversible by H_2S donors including AP39 [320,249]. Expression dynamics suggest MPST-3 acts mainly as a sulfotransferase, converting sulfite to thiosulfate rather than producing H_2S, supported by its co-expression with SQRD-1 and ETHE-1 and opposite regulation to SUOX-1. No MPST isoform has been linked to body size regulation.

Knockdown of *phy-2*, encoding a prolyl-4-hydroxylase required for collagen maturation [321], reduced lifespan and increased body size (Table 24, 25). While *phy-2* deletion alone produces no phenotype due to redundancy with *dpy-18*, deletion of both is lethal [321]. We observed *dpy-18* overexpression in *vhl-1* mutants in a *sqrd-1*–dependent manner (Table 13). Given the broad downregulation of collagens, the lifespan reduction caused by *phy-2* knockdown underscores the importance of collagen synthesis in this context.

GST-19 was among the most upregulated proteins in *vhl-1* mutants (up to 24-fold at day 1) and selectively reduced lifespan without affecting body size (Table 24, 25). Although GST-19 has not been linked to longevity, other GSTs have: *daf-2(e1370)* mutants upregulate GSTs [322] , GST-10 overexpression extends lifespan [323], while knockdown of *gst-5* or *gst-10* shortens it [329]. Conversely, *gst-14* knockdown more than doubles the lifespan of *gas-1(fc21)* (complex I) mutants [324], highlighting the diverse roles of GSTs in lifespan regulation.

Double knockdown of *col-8* and *col-149* caused the strongest size reduction, specifically in *sqrd-1;vhl-1* double mutants. These collagens likely act redundantly to regulate body size in this context. *vhl-1* mutation alone reduced their expression, which *sqrd-1* mutation restored, contributing to the increased size of double mutants. However, this did not affect lifespan, suggesting collagen changes are more a consequence than a driver of *vhl-1* phenotypes. Components of the TGF-β pathway, such as DPY-23, are known to regulate collagens including *col-149* [325].

Overall, these findings reveal that *sqrd-1* influences lifespan and body size in *vhl-1* mutants through multiple downstream targets, particularly complex I subunits. Restoration of mitochondrial function by *sqrd-1* mutation links complex I to both lifespan and size, whereas other regulators act primarily on lifespan. This highlights mitochondrial remodeling and metabolic rewiring downstream of sulfide oxidation as central drivers of *vhl-1* phenotypes.

5.5. Characterizing Mesna, a lifespan and stress resistance inducer, as a potential new H_2S modulator

Mesna (2-mercaptoethanesulfonic acid, CoM) is a clinically used thiol compound known to replenish glutathione (GSH) and scavenge free radicals [174,175]. Its sulfhydryl group can potentially support GSH synthesis and facilitate H_2S-to-persulfide conversions [326,327], processes central to oxidative stress defense and mitochondrial protection during ischemia–reperfusion injury (IRI). H_2S itself enhances GSH synthesis and mitochondrial localization, providing protection during IRI [328,126], yet no H_2S donor has been clinically approved. Since Mesna is already in clinical use, repurposing it as

an IRI prophylactic may be safer and faster than developing novel donors, but this requires a deeper understanding of its mechanisms.

We first tested Mesna's ability to prevent hypoxia-associated damage, a common driver of IRI [329]. *C. elegans* typically tolerates moderate hypoxia, showing deleterious effects like delayed development or protein aggregation only under severe oxygen deprivation [330]. Preconditioning wild-type worms from egg to L4 stage with Mesna, DATS, or DADS revealed that 6 mM Mesna accelerated development under 0.1% O_2, with more animals reaching adulthood within 72 h (**Figure 14A**). We next examined protein aggregation using a PolyQ transgenic model (*unc-54p::Q35::YFP*), where 0.6mM and 1.2mM Mesna preconditioning reduced aggregate formation after 24 h of hypoxia (**Figure 14B**).

Given Mesna's antioxidant properties, we tested its ability to protect against paraquat-induced toxicity. Paraquat induces ferroptosis via ROS and lipid peroxides in kidney cells [273,331], making it a relevant oxidative stress model. A 24h exposure of L4-stage worms to 6mM Mesna increased survival by ~40% under paraquat challenge (**Figure 14C**). Because enhanced stress resistance often correlates with lifespan [332,333], we exposed worms continuously to 6mM Mesna from L4 through adulthood, observing a 15% lifespan extension compared with controls (**Figure 14D**). While Mesna's antioxidant activity is well known [334], its effect on lifespan had not been previously reported. In rats, lifelong Mesna treatment did not extend survival under ochratoxin A toxicity [335], but a regulatory toxicology report from ECHA described a significant lifespan increase in preclinical studies [336] , suggesting broader biological potential beyond its uroprotective role. While the report in question does not provide detailed experimental conditions or a peer-reviewed publication, it suggests that Mesna may exert biological effects relevant to aging.

Mesna's free thiol group can modulate antioxidant systems, particularly GSH [266,326], and might regenerate GSSH or enhance H_2S-to-persulfide conversion during oxidative stress. To test whether its protective effects depended on SQRD-1, a key enzyme producing GSSH from GSH, we exposed *sqrd-1(mr28)* mutants to paraquat. Surprisingly, these mutants were more responsive to Mesna and showed protection even at 3mM (**Figure 15A**). Although counterintuitive, several factors may explain this: impaired H_2S oxidation in *sqrd-1* mutants could disrupt H_2S and persulfide turnover, which Mesna might partially restore; reduced basal mitochondrial respiration in *sqrd-1*

mutants (**Figure 12A**) may lower paraquat's damaging potential, as it relies on complex I redox cycling [312]; and a trend toward higher paraquat resistance in *sqrd-1* mutants (**Figure 12F**) supports a link between impaired H_2S oxidation, paraquat sensitivity, and Mesna's modulatory effects.

However, continuous Mesna exposure throughout life did not extend lifespan in *sqrd-1* mutants and instead shortened it at higher concentrations, including those protective against paraquat (**Figure 15B**). This suggests that a disrupted sulfur/redox environment in these mutants is differentially affected by Mesna: potentially improved under acute stress but detrimental with chronic exposure. Differences between aging-related stress and acute oxidative insults may contribute to this dichotomy. Further evidence of *sqrd-1* mutants' Mesna sensitivity came from acute exposure to increasing concentrations, which revealed heightened susceptibility to Mesna-induced lethality (**Figure 15C**).

Overall, our findings demonstrate that Mesna confers hypoxia and oxidative stress resistance, extends lifespan in wild-type animals, and modulates redox balance potentially through interactions with GSH and H_2S pathways. Its paradoxical effects in *sqrd-1* mutants suggest that sulfur metabolism context critically shapes Mesna's actions. These results highlight Mesna's potential as a clinically relevant H_2S modulator and provide a foundation for exploring its therapeutic role in IRI and redox-related pathologies.

5.6. Mesna modulates SQRD-1 expression and H_2S-related metabolites

To better understand Mesna's effects in *C. elegans* and its differential impact in *sqrd-1* mutants, we examined whether it influenced *sqrd-1* expression. Exposure to 6mM Mesna significantly increased *sqrd-1* mRNA levels (**Figure 16A**) and SQRD-1::mKate2 protein abundance (**Figure 16B** and **C**). Combined with Mesna's phenotypic effects in *sqrd-1* mutants, these results suggested that H_2S and related metabolites might be altered following treatment.

Indeed, Mesna induced H_2S accumulation in day 1 wild-type animals (**Figure 16D**). Although it did not significantly change total GSH (**Figure 16E**) or GSSH (**Figure 16F**),

it increased the GSH/GSSG ratio (**Figure 16G**), indicating a shift toward a more reduced cellular redox state. At baseline, *sqrd-1* mutants exhibited elevated H_2S and persulfide levels, but reduced GSH (**Figure 16D** and **E**). Mesna exposure did not further increase sulfide levels in these mutants but restored their depleted GSH (**Figure 16E**) and enhanced the GSH/GSSG ratio (**Figure 16G**), again without increasing GSSH (**Figure 16F**).

These results suggest that Mesna protects wild-type animals at least partly by improving the overall redox balance, shifting glutathione toward its reduced form. In *sqrd-1* mutants, Mesna's capacity to restore low GSH levels amplified this shift, potentially contributing to its stronger effects. Based on these findings, we hypothesized that Mesna may promote persulfide formation indirectly by causing H_2S accumulation and sparing GSH through non-enzymatic reactions with H_2S. Formation of a Mesna-persulfide intermediate in the presence of excess H_2S could help maintain GSSH levels by reducing GSH consumption.

5.7. Screening the hydrogen sulfide metabolism related proteins reveals a negative regulator of Mesna protective effect

Our data strongly indicated that Mesna's protective effects relied on modulating H_2S and related metabolites. To deepen our understanding and identify negative regulators of this protection, we screened mutants deficient in key enzymes of H_2S synthesis (*cbs-1*, *cth-1*, *mpst-1*, *mpst-7*), detoxification (*ethe-1*), and signaling (*cysl-1*, *skn-1*). Among them, *mpst-1(ok2040)* mutants failed to acquire additional resistance to paraquat-induced death following Mesna preconditioning (**Figure 17D**). *skn-1(zu67)* mutants produced inconsistent results—likely due to heterozygosity in one replicate—and were excluded from further interpretation.

The consistent absence of Mesna-induced protection in *mpst-1* mutants suggests a crucial role for MPST-1 in mediating Mesna's effects. These mutants have been reported to exhibit a ~15% shorter lifespan [248], and ~20% lower stress resistance (**Figure 17C** and **D**), alongside reduced healthspan markers such as accelerated decline in pharyngeal pumping and motility [270]. Although more susceptible to paraquat-induced oxidative stress, *mpst-1* mutants recover normal lifespan, healthspan, and

ROS levels upon treatment with the H_2S donor GYY4137 [248]. Their endogenous H_2S production is ~43% lower than wild type, underscoring MPST-1's importance in maintaining sulfide homeostasis. These findings suggest that impaired H_2S production underlies their shortened lifespan and reduced stress resistance and that exogenous H_2S can reverse these phenotypes.

However, the inability of Mesna to protect *mpst-1* mutants, despite its H_2S-elevating effects in wild-type animals, suggests that H_2S increase alone does not account for Mesna's protective action. Instead, modulation of GSH and GSSH levels may be central in our experimental context. Supporting this, 3-MST knockout mice show a 50% reduction in total persulfidated species, including GSSH, in the brain [337] Conversely, a more recent study proposed that 3-MST, CBS, and CSE are not the primary sources of persulfides, implicating cysteinyl-tRNA synthetase (CARS) as the major enzyme responsible for producing small persulfides like GSSH [338]. Together, these findings indicate that MPST-1 is essential for Mesna's protective effects and highlight the importance of persulfide regulation beyond H_2S production alone.

5.8. Mitochondrial respiration is a target for Mesna preconditioning against paraquat

After identifying two mutants with distinct responses to Mesna preconditioning compared with wild type, we investigated proteomic changes underlying these differences. Animals were preconditioned with 3 or 6mM Mesna and exposed to paraquat for 48 hours, reaching day 2 of adulthood — the earliest timepoint when mortality begins (**Figure 14C**). This allowed us to capture Mesna-induced changes before severe paraquat damage skewed the proteomic profile. Principal component analysis revealed clear clustering and indicated that *sqrd-1* mutants were more responsive to Mesna preconditioning than wild-type or *mpst-1* mutants (**Figure 18A**).

To identify pathways altered by Mesna under protective conditions, we focused on proteins regulated in the strongest response scenario — 6 mM Mesna treatment in wild-type and *sqrd-1* animals. Molecular function enrichment highlighted a single significant term: cytochrome *c* oxidase (Complex IV) (**Figure 18B**). Complex IV is the terminal enzyme of the mitochondrial electron transport chain, catalyzing oxygen

reduction to water while pumping protons to support ATP synthesis [339]. t is inhibited by H_2S, which binds the heme-a_3/Cu^b binuclear center in a noncompetitive manner, blocking electron flow and ATP generation [340]. At lower concentrations, however, H_2S can serve as a substrate for Complex IV, being oxidized at the same active site and forming intermediate persulfides [340]. Disruption of Complex IV activity by H_2S can cause electron accumulation, mitochondrial membrane depolarization, and elevated reactive oxygen species (ROS), worsening oxidative stress [341].

These findings suggest that Mesna's protective effects against paraquat are closely linked to mitochondrial respiration and Complex IV activity, likely through modulation of H_2S interactions with the electron transport chain.

5.9. Complex IV subunit regulation by Mesna may protect mitochondrial function from paraquat-induced damage

When we included all proteins regulated by 3mM Mesna preconditioning against paraquat in *sqrd-1* mutants and excluded those regulated under non-protective conditions in *mpst-1* mutants, only four proteins remained — all subunits of cytochrome *c* oxidase (Complex IV) (**Table 26**). This pointed to a positive regulation of Complex IV in Mesna-preconditioned samples compared with paraquat-only controls. Supporting this, overexpression of COX5A in smooth muscle cells was shown to reduce ROS, enhance oxygen consumption, and improve ATP production under stress [342]. Similarly, studies in *Arabidopsis thaliana* and *Saccharomyces cerevisiae* demonstrated that while COX11 overexpression enhances stress resistance, its knockdown reduces ROS, suggesting protective roles beyond its function in the electron transport chain [343].

To assess whether Mesna modulates mitochondrial function to counteract paraquat-induced damage, we measured mitochondrial membrane potential (MMP) and observed significant recovery with Mesna preconditioning (**Figure 19A** and **B**). Oxygen consumption, which declined markedly after paraquat exposure, was also partially restored by Mesna (**Figure 19C**). These results support the idea that induction of cytochrome *c* oxidase links Mesna's protective effect to improved mitochondrial function.

We propose that Mesna exerts a hormetic effect on Complex IV subunit expression by elevating cellular H_2S and persulfide (notably GSSH) levels. At moderate concentrations, reactive sulfur species can trigger mild mitochondrial stress or redox signaling that upregulates protective components of the electron transport chain, enhancing respiration and reducing ROS [340,344]. This protective mechanism appears amplified in *sqrd-1(mr28)* mutants, which accumulate H_2S and persulfides to beneficial levels, but is absent in *mpst-1(ok2040)* mutants, where H_2S levels are reduced [249]. Thus, sulfide and persulfide signaling likely play essential roles in activating Complex IV expression and mediating resistance to paraquat-induced oxidative stress.

5.10. Characterization of the protective effect of Mesna in kidney mIMCD3 cells

To test whether our findings extended to the kidney, we used mIMCD3 cells, derived from the mouse inner medullary collecting duct. These cells provide a physiologically relevant model for studying renal epithelial stress responses [345], as the inner medulla naturally experiences high osmolarity, low oxygen, and elevated ROS [346]. mIMCD3 cells are therefore ideal for assessing how Mesna preconditioning enhances redox resilience and mitochondrial function in renal epithelia, processes central to nephrotoxic injury [347].

Live-cell imaging revealed that 24-hour Mesna preconditioning strongly protected mIMCD3 cells from paraquat-induced mortality, with survival levels approaching those of untreated controls, as measured by the membrane-impermeable dye DiYO-1 (**Figure 20A** and **B**). Furthermore, Mesna preconditioning significantly reduced mitochondrial ROS and lipid peroxidation compared to paraquat-only treatment (**Figure 20C–F**). These results mirror our findings in *C. elegans* (**Figure 13**) and support a conserved protective mechanism in renal cells involving redox modulation and mitochondrial protection.

5.11. Mesna improves mitochondrial function in mIMCD3 cells under paraquat-induced stress

To assess this, we measured mitochondrial membrane potential (MMP), which decreased after paraquat exposure. Mesna alone modestly increased MMP, but did not prevent paraquat-induced loss (**Figure 23A**). Persulfide accumulation may contribute to this increase, as treatment of Hepa1c1c7 cells with cystine or glutathione trisulfide (GSSSG) elevated persulfide levels and lowered the ADP/ATP ratio, an effect abolished by SQOR knockdown [348]. However, in our model, SQOR silencing did not prevent the Mesna-induced MMP rise. Because MMP fluctuations do not always parallel ATP levels during mitochondrial dynamics or stress [349], we also measured the ADP/ATP ratio. Paraquat significantly increased this ratio, indicating mitochondrial dysfunction and impaired ATP synthesis [311], whereas Mesna preconditioning prevented this increase (**Figure 23B**). This effect was lost after SQOR knockdown, suggesting SQOR-dependent persulfide formation is necessary for Mesna to preserve ATP production.

These findings align with recent evidence that persulfide formation is essential for mitochondrial function [276]. SQOR is required for cystine- and GSSSG-driven ATP synthesis, and Cars2 has been identified as another key persulfide-producing enzyme [276]. However, the persistence of Mesna's protective effect against paraquat-induced death despite SQOR knockdown (**Figure 22A** and **B**) indicates that ATP preservation alone does not explain improved survival. Mesna likely orchestrates broader mitochondrial and possibly cytosolic responses, extending beyond sulfur metabolism modulation. Our observations of Complex IV subunit regulation in *C. elegans* suggest a similar mechanism may contribute to Mesna's protective effects in mIMCD3 cells, although regulatory pathways could differ between species.

5.12. Study limitations and outlook

While this study advances our understanding of how sulfide metabolism, mitochondrial remodeling, and SQRD-1 activity shape hypoxia adaptation and phenotype determination in *C. elegans*, as well as how the thiol drug Mesna modulates these processes, several important limitations must be acknowledged. These limitations

span methodological constraints, biological uncertainties, and interpretative gaps, and they also point to promising directions for future research.

A key limitation of this work lies in the primarily descriptive nature of the proteomic and transcriptomic analyses. While large-scale datasets revealed broad changes in metabolic pathways, mitochondrial processes, and sulfur metabolism, they do not directly establish enzyme activity, substrate flux, or causal relationships. For example, our conclusions about increased mitochondrial sulfide oxidation and persulfide buffering are based on protein abundance and metabolite levels (only at 1 timepoint), but we did not directly measure enzymatic rates, substrate turnover, or real-time metabolic flux. Similarly, although we observed changes in proteins associated with oxidative phosphorylation and the tricarboxylic acid cycle, these do not necessarily reflect functional changes in respiration or ATP synthesis at the organelle level. Future studies employing stable enzymatic assays would allow a more mechanistic dissection of how metabolic reprogramming unfolds downstream of HIF-1 and SQRD-1.

Another important methodological limitation is the lack of direct measurement of protein persulfidation. Many of our hypotheses regarding sulfur buffering, redox regulation, and the interplay between GSH, GSSH, and H_2S rely on indirect evidence, such as metabolite ratios and protein expression profiles. Direct assessment of persulfidation on key mitochondrial and cytosolic proteins — for example, through mass spectrometry-based detection or selective persulfide probes — would provide stronger mechanistic insight into how these modifications influence metabolism, stress resistance, and lifespan. Furthermore, while we propose that MPST-3 may function predominantly as a sulfotransferase (TST) in the context of elevated H_2S, this remains speculative without direct enzymatic characterization. Future biochemical studies should aim to clarify MPST-3's catalytic preferences and substrate specificity under different redox and metabolic states.

The bulk nature of our proteomic analyses also introduces interpretative limitations. Because transcriptomic and proteomic profiling were performed on whole animals or whole tissues, cell-type-specific effects could not be resolved. This may be particularly relevant given that hypoxia responses, H_2S metabolism, and redox signaling can vary substantially between tissues and cell types, and has even been described to affect neuronal and intestinal cells differently in *C. elegans* regarding its interaction with H_2S [237]. Approaches such as single-cell RNA sequencing, spatial transcriptomics, or cell-

specific proteomics could help refine our understanding of how HIF-1 activation and sulfide metabolism reprogramming manifest in distinct cellular contexts.

Another limitation concerns the reliance on RNAi and genetic mutants to infer functional relationships. While effective, RNAi knockdown may not fully recapitulate complete loss-of-function phenotypes, and compensatory mechanisms could obscure the direct consequences of gene disruption. Additionally, while our genetic screens identified several candidate proteins influencing lifespan and body size, the precise molecular mechanisms linking their modulation to these phenotypes remain incompletely understood. Complementary approaches, such as CRISPR-based knockouts, inducible tissue-specific gene perturbations, and targeted rescue experiments, could help clarify causal relationships.

Our work also raises several biological questions that remain unresolved. The mechanisms by which Mesna modulates sulfide metabolism and mitochondrial function, for instance, are not fully elucidated. While Mesna increased *sqrd-1* expression and altered sulfide-related metabolites, the precise molecular targets and pathways mediating these effects are unknown. Moreover, the observation that Mesna's protective effect is lost in *mpst-1* mutants but retained in *sqrd-1* mutants suggests a complex interplay between sulfide oxidation, persulfide formation, and glutathione metabolism that warrants deeper investigation. Elucidating whether Mesna or its potential persulfide intermediates directly modify signaling proteins, mitochondrial enzymes, or transcription factors could reveal new layers of regulation.

Another unresolved question concerns the dual role of H_2S in mitochondrial function. While elevated H_2S can inhibit cytochrome c oxidase and suppress respiration, it may also act as a substrate and signaling molecule at lower concentrations. Disentangling the concentration-dependent effects of H_2S and persulfides on complex IV activity, ROS generation, and modulation of mitochondrial overall physiology remains a critical challenge. Combining genetic tools with precise, time-resolved sulfide delivery systems and/or mitochondrial functional assays will be essential to dissect these dynamics.

Finally, while our study revealed strong parallels between *C. elegans* and mIMCD3 cells in terms of Mesna's effects on redox state, mitochondrial function, and survival under oxidative stress, some observations — such as the partial dissociation between

mitochondrial membrane potential, ATP, and protection against paraquat — suggest that additional, possibly species-specific regulatory mechanisms are at play. Expanding comparative studies across different cell types and exploring how sulfide metabolism interfaces with broader stress response networks will help refine the translational relevance of these findings.

In summary, despite these limitations, our work establishes a framework for understanding how sulfide metabolism, mitochondrial adaptation, and thiol modulation intersect to shape hypoxia responses, stress resistance, and organismal phenotypes. Addressing the methodological gaps identified here — particularly through direct measurements of persulfidation, cell-type-resolved analyses, and deeper biochemical characterization of key enzymes — will sharpen our mechanistic understanding. Future studies should also explore the therapeutic potential of Mesna, clarifying how it modulates H_2S and persulfide signaling to preserve mitochondrial function and redox balance. Such work will not only deepen our understanding of sulfur metabolism in hypoxia but may also open new avenues for targeting metabolic and oxidative stress in disease.

6. Conclusion

This thesis set out to test the hypothesis that sulfide metabolism, modulated by the mitochondrial enzyme SQRD-1, is a central regulator of metabolic reprogramming and phenotype determination downstream of HIF-1 activation, and that pharmacological modulation of this pathway with Mesna can influence these processes.

We first demonstrated that genetic stabilization of HIF-1 through *vhl-1* deletion induces broad metabolic remodeling in *C. elegans*, accompanied by reduced body size, extended lifespan, and altered mitochondrial function. Comparison with *egl-9* mutants revealed that distinct modes of HIF-1 activation yield different phenotypic outcomes, underlining the importance of upstream regulation in shaping hypoxic responses. Transcriptomic and proteomic profiling showed that many—but not all—HIF-1-dependent changes also require SQRD-1, highlighting its role as a key downstream effector of HIF-1 signaling.

Consistent with our hypothesis, *vhl-1* mutants displayed upregulation of mitochondrial sulfide detoxification machinery, including SQRD-1, MPST-3, and ETHE-1, indicating enhanced capacity for sulfide oxidation and persulfide buffering. These changes occurred alongside downregulation of oxidative phosphorylation, mitochondrial content, and membrane potential, suggesting that elevated sulfide and impaired respiration are mechanistically linked. The shortened body size observed in *vhl-1* mutants was phenocopied by exogenous H_2S donors in wild-type animals but not in the mutants themselves, supporting the idea that H_2S accumulation contributes directly to this phenotype.

We also identified key downstream targets of SQRD-1 that influence lifespan and body size, including components of complex I, glycolytic enzymes, and prolyl hydroxylases. Knockdown of these proteins modulated both traits in *vhl-1* mutants, indicating that mitochondrial function and metabolic rewiring are central to the observed phenotypes.

Building on these findings, we explored whether Mesna, a clinically approved thiol compound, could modulate sulfide metabolism. Mesna preconditioning improved stress resistance, reduced protein aggregation, extended lifespan, and shifted the glutathione redox state toward a more reduced environment. It also increased *sqrd-1* expression and elevated H_2S levels. Importantly, Mesna's protective effect was abolished in *mpst-1* mutants, implicating persulfide metabolism rather than sulfide concentration alone in its mechanism of action.

Proteomic and functional analyses revealed that Mesna modulates components of mitochondrial complex IV, enhances membrane potential, and partially restores oxygen consumption after paraquat exposure. These protective effects extended to mammalian mIMCD3 cells, where Mesna reduced oxidative stress and preserved mitochondrial function. Although SQOR knockdown elevated sulfide and persulfide levels, Mesna's protective effects persisted, suggesting that its influence extends beyond metabolite modulation to include broader mitochondrial adaptations.

Together, these findings support our central hypothesis: sulfide metabolism, coordinated by SQRD-1, is a major determinant of metabolic and phenotypic responses downstream of HIF-1 activation, and pharmacological modulation of this pathway with Mesna can shape these outcomes. They also highlight new mechanistic

links between H_2S oxidation, mitochondrial remodeling, and stress resistance, revealing how altered sulfur metabolism contributes to organismal physiology.

Future studies should focus on directly quantifying persulfidation, characterizing MPST-3's enzymatic activity, and applying single-cell or tissue-specific approaches to resolve spatial aspects of these processes. Investigating how thiol modulators orchestrate complex IV regulation and mitochondrial signaling will further clarify their therapeutic potential. Ultimately, this work establishes a foundation for targeting sulfide metabolism and mitochondrial adaptation as strategies to mitigate hypoxia-related and oxidative stress–driven diseases.

7. References

1. Powell, C. R., Dillon, K. M. & Matson, J. B. A review of hydrogen sulfide (H2S) donors: Chemistry and potential therapeutic applications. *Biochem. Pharmacol.* **149**, 110–123 (2018).

2. Abe, K. & Kimura, H. The possible role of hydrogen sulfide as an endogenous neuromodulator. *J. Neurosci.* **16**, 1066–1071 (1996).

3. Mustafa, A. K., Gadalla, M. M. & Snyder, S. H. Signaling by Gasotransmitters. *Sci. Signal.* **2**, (2009).

4. Li, L., Rose, P. & Moore, P. K. Hydrogen Sulfide and Cell Signaling. *Annu. Rev. Pharmacol. Toxicol.* **51**, 169–187 (2011).

5. Wang, R. Two's company, three's a crowd: can H 2 S be the third endogenous gaseous transmitter? *FASEB J.* **16**, 1792–1798 (2002).

6. Xuan, W., Sheng, C., Cao, Y., He, W. & Wang, W. Fluorescent Probes for the Detection of Hydrogen Sulfide in Biological Systems. *Angew. Chemie Int. Ed.* **51**, 2282–2284 (2012).

7. Lin, V. S., Chen, W., Xian, M. & Chang, C. J. Chemical probes for molecular imaging and detection of hydrogen sulfide and reactive sulfur species in biological systems. *Chem. Soc. Rev.* **44**, 4596–4618 (2015).

8. Olas, B. Hydrogen sulfide in signaling pathways. *Clin. Chim. Acta* **439**, 212–218 (2015).

9. Liu, X.-Y., Qian, L.-L. & Wang, R.-X. Hydrogen Sulfide-Induced Vasodilation: The Involvement of Vascular Potassium Channels. *Front. Pharmacol.* **13**, 911704 (2022).

10. Kamoun, P. [H2S, a new neuromodulator]. *Med. Sci. (Paris).* **20**, 697–700 (2004).

11. Zanardo, R. C. O. *et al.* Hydrogen sulfide is an endogenous modulator of leukocyte-mediated inflammation. *FASEB J.* **20**, 2118–20 (2006).

12. Jennings, M. L. Transport of H 2 S and HS − across the human red blood cell membrane: rapid H 2 S diffusion and AE1-mediated Cl − /HS − exchange. *Am. J. Physiol. Physiol.* **305**, C941–C950 (2013).

13. Wang, R. Physiological Implications of Hydrogen Sulfide: A Whiff Exploration That Blossomed. *Physiol. Rev.* **92**, 791–896 (2012).

14. Li, Q. & Lancaster, J. R. Chemical foundations of hydrogen sulfide biology. *Nitric Oxide* **35**, 21–34 (2013).

15. Hughes, M. N., Centelles, M. N. & Moore, K. P. Making and working with

hydrogen sulfide. *Free Radic. Biol. Med.* **47**, 1346–1353 (2009).

16. DeLeon, E. R., Stoy, G. F. & Olson, K. R. Passive loss of hydrogen sulfide in biological experiments. *Anal. Biochem.* **421**, 203–207 (2012).

17. Kabil, O., Chemistry, R. B.-J. of B. & 2010, undefined. Redox biochemistry of hydrogen sulfide. *ASBMB*.

18. Kabil, O. & Banerjee, R. Enzymology of H2S biogenesis, decay and signaling. *Antioxidants Redox Signal.* **20**, 770–782 (2014).

19. Szabo, C. *et al.* Regulation of mitochondrial bioenergetic function by hydrogen sulfide. Part I. Biochemical and physiological mechanisms. *Br. J. Pharmacol.* **171**, 2099–122 (2014).

20. Banerjee, R. Catalytic promiscuity and heme-dependent redox regulation of H 2 S synthesis. *Curr. Opin. Chem. Biol.* **37**, 115–121 (2017).

21. Chiku, T. *et al.* H2S Biogenesis by Human Cystathionine γ-Lyase Leads to the Novel Sulfur Metabolites Lanthionine and Homolanthionine and Is Responsive to the Grade of Hyperhomocysteinemia. *J. Biol. Chem.* **284**, 11601–11612 (2009).

22. Singh, S., Padovani, D., Leslie, R. A., Chiku, T. & Banerjee, R. Relative Contributions of Cystathionine β-Synthase and γ-Cystathionase to H2S Biogenesis via Alternative Trans-sulfuration Reactions. *J. Biol. Chem.* **284**, 22457–22466 (2009).

23. Fu, M. *et al.* Hydrogen sulfide (H 2 S) metabolism in mitochondria and its regulatory role in energy production. *Proc. Natl. Acad. Sci.* **109**, 2943–2948 (2012).

24. Teng, H. *et al.* Oxygen-sensitive mitochondrial accumulation of cystathionine β-synthase mediated by Lon protease. *Proc. Natl. Acad. Sci.* **110**, 12679–12684 (2013).

25. Nagahara, N., Ito, T., Kitamura, H. & Nishino, T. Tissue and subcellular distribution of mercaptopyruvate sulfurtransferase in the rat: confocal laser fluorescence and immunoelectron microscopic studies combined with biochemical analysis. *Histochem. Cell Biol.* **110**, 243–250 (1998).

26. Abou-Hamdan, A. *et al.* Oxidation of H2S in Mammalian Cells and Mitochondria. in 201–228 (2015). doi:10.1016/bs.mie.2014.11.042.

27. Kimura, H. Hydrogen sulfide: its production, release and functions. *Amino Acids* **41**, 113–121 (2011).

28. Wang, B. *et al.* Hypoxia and chronic kidney disease. *EBioMedicine* **77**, 103942 (2022).

29. Busl, K. M. & Greer, D. M. Hypoxic-ischemic brain injury: pathophysiology, neuropathology and mechanisms. *NeuroRehabilitation* **26**, 5–13 (2010).

30. DeLeon, E. R., Gao, Y., Huang, E. & Olson, K. R. Garlic oil polysulfides: H2S- and O2-independent prooxidants in buffer and antioxidants in cells. *Am. J. Physiol. Regul. Integr. Comp. Physiol.* **310**, R1212-25 (2016).

31. Benavides, G. A. *et al.* Hydrogen sulfide mediates the vasoactivity of garlic. *Proc. Natl. Acad. Sci.* **104**, 17977–17982 (2007).

32. Olson, K. R. *et al.* Thiosulfate: a readily accessible source of hydrogen sulfide in oxygen sensing. *Am. J. Physiol. Integr. Comp. Physiol.* **305**, R592–R603 (2013).

33. Tangerman, A. Measurement and biological significance of the volatile sulfur compounds hydrogen sulfide, methanethiol and dimethyl sulfide in various biological matrices. *J. Chromatogr. B* **877**, 3366–3377 (2009).

34. Furne, J., Saeed, A. & Levitt, M. D. Whole tissue hydrogen sulfide concentrations are orders of magnitude lower than presently accepted values. *Am. J. Physiol. Integr. Comp. Physiol.* **295**, R1479–R1485 (2008).

35. Shaw, R. W., Hansen, R. E. & Beinert, H. Responses of the a3 component of cytochrome c oxidase to substrate and ligand addition. *Biochim. Biophys. Acta - Bioenerg.* **504**, 187–199 (1978).

36. Levitt, M. D., Abdel-Rehim, M. S. & Furne, J. Free and Acid-Labile Hydrogen Sulfide Concentrations in Mouse Tissues: Anomalously High Free Hydrogen Sulfide in Aortic Tissue. *Antioxid. Redox Signal.* **15**, 373–378 (2011).

37. Vitvitsky, V., Kabil, O. & Banerjee, R. High Turnover Rates for Hydrogen Sulfide Allow for Rapid Regulation of Its Tissue Concentrations. *Antioxid. Redox Signal.* **17**, 22–31 (2012).

38. Blackstone, E., Morrison, M. & Roth, M. B. H 2 S Induces a Suspended Animation-Like State in Mice. *Science (80-.).* **308**, 518–518 (2005).

39. Beauchamp, R. O. *et al.* A Critical Review of the Literature on Hydrogen Sulfide Toxicity. *CRC Crit. Rev. Toxicol.* **13**, 25–97 (1984).

40. Hildebrandt, T. M. & Grieshaber, M. K. Three enzymatic activities catalyze the oxidation of sulfide to thiosulfate in mammalian and invertebrate mitochondria. *FEBS J.* **275**, 3352–3361 (2008).

41. Olson, K. R. A theoretical examination of hydrogen sulfide metabolism and its potential in autocrine/paracrine oxygen sensing. *Respir. Physiol. Neurobiol.* **186**, 173–179 (2013).

42. Libiad, M. *et al.* Hydrogen sulfide perturbs mitochondrial bioenergetics and triggers metabolic reprogramming in colon cells. *J. Biol. Chem.* **294**, 12077–12090 (2019).

43. Hildebrandt, T. M. & Grieshaber, M. K. Three enzymatic activities catalyze the oxidation of sulfide to thiosulfate in mammalian and invertebrate mitochondria. *FEBS J.* **275**, 3352–61 (2008).

44. Goubern, M., Andriamihaja, M., Nübel, T., Blachier, F. & Bouillaud, F. Sulfide,

the first inorganic substrate for human cells. *Wiley Online Libr.* **21**, 1699–1706 (2007).

45. Mishanina, T. V., Yadav, P. K., Ballou, D. P. & Banerjee, R. Transient Kinetic Analysis of Hydrogen Sulfide Oxidation Catalyzed by Human Sulfide Quinone Oxidoreductase. *J. Biol. Chem.* **290**, 25072–25080 (2015).

46. Landry, A. P., Ballou, D. P. & Banerjee, R. H2S oxidation by nanodisc-embedded human sulfide quinone oxidoreductase. *J. Biol. Chem.* **292**, 11641–11649 (2017).

47. Dawson, P. A. Sulfate in fetal development. *Semin. Cell Dev. Biol.* **22**, 653–9 (2011).

48. Kappler, U. & Enemark, J. H. Sulfite-oxidizing enzymes. *JBIC J. Biol. Inorg. Chem.* **20**, 253–264 (2015).

49. Feng, C., Tollin, G. & Enemark, J. H. Sulfite oxidizing enzymes. *Biochim. Biophys. Acta - Proteins Proteomics* **1774**, 527–539 (2007).

50. Rajapakshe, A., Tollin, G. & Enemark, J. H. Kinetic and Thermodynamic Effects of Mutations of Human Sulfite Oxidase. *Chem. Biodivers.* **9**, 1621–1634 (2012).

51. Landry, A. P., Ballou, D. P. & Banerjee, R. Hydrogen Sulfide Oxidation by Sulfide Quinone Oxidoreductase. *ChemBioChem* **22**, 949–960 (2021).

52. Jackson, M. R., Melideo, S. L. & Jorns, M. S. Human Sulfide:Quinone Oxidoreductase Catalyzes the First Step in Hydrogen Sulfide Metabolism and Produces a Sulfane Sulfur Metabolite. *Biochemistry* **51**, 6804–6815 (2012).

53. Landry, A. P., Ballou, D. P. & Banerjee, R. H2S oxidation by nanodisc-embedded human sulfide quinone oxidoreductase. *J. Biol. Chem.* **292**, 11641–11649 (2017).

54. Cole, D. E. & Evrovski, J. Screening for sulfite oxidase deficiency with urinary thiosulfate/sulfate ratios determined by anion chromatography. *Clin. Chem.* **42**, 654–5 (1996).

55. Cole, D. E. C., Evrovski, J. & Pirone, R. Urinary thiosulfate determined by suppressed ion chromatography with conductimetric detection. *J. Chromatogr. B Biomed. Sci. Appl.* **672**, 149–154 (1995).

56. Cole, D. E. . & Evrovski, J. Quantitation of sulfate and thiosulfate in clinical samples by ion chromatography. *J. Chromatogr. A* **789**, 221–232 (1997).

57. Landry, A. P., Ballou, D. P. & Banerjee, R. Modulation of Catalytic Promiscuity during Hydrogen Sulfide Oxidation. *ACS Chem. Biol.* **13**, 1651–1658 (2018).

58. TOGAWA, T. *et al.* High Performance Liquid Chromatographic Determination of Bound Sulfide and Sulfite and Thiosulfate at Their Low Levels in Human Serum by Pre-column Fluorescence Derivatization with Monobromobimane. *Chem. Pharm. Bull.* **40**, 3000–3004 (1992).

59. Ji, A. J., Savon, S. R. & Jacobsen, D. W. Determination of total serum sulfite by HPLC with fluorescence detection. *Clin. Chem.* **41**, 897–903 (1995).

60. Shih, V. E. *et al.* Sulfite Oxidase Deficiency. *N. Engl. J. Med.* **297**, 1022–1028 (1977).

61. Vincent, A. S. *et al.* Sulfite-mediated oxidative stress in kidney cells. *Kidney Int.* **65**, 393–402 (2004).

62. Iatropoulos, A. *et al.* Changes of volatile sulphur compounds during therapy of a case series of patients with chronic periodontitis and halitosis. *J. Clin. Periodontol.* **43**, 359–365 (2016).

63. Meister, A. Glutathione metabolism and its selective modification. *J. Biol. Chem.* **263**, 17205–8 (1988).

64. Benchoam, D. *et al.* Acidity and nucleophilic reactivity of glutathione persulfide. *J. Biol. Chem.* **295**, 15466–15481 (2020).

65. Cai, F. *et al.* Sulfide:quinone oxidoreductase alleviates ferroptosis in acute kidney injury via ameliorating mitochondrial dysfunction of renal tubular epithelial cells. *Redox Biol.* **69**, 102973 (2024).

66. Marutani, E. *et al.* Sulfide catabolism ameliorates hypoxic brain injury. *Nat. Commun.* **12**, 3108 (2021).

67. Marutani, E. *et al.* Sulfide catabolism ameliorates hypoxic brain injury. *Nat. Commun.* **12**, 3108 (2021).

68. Xie, Z.-Z., Liu, Y. & Bian, J.-S. Hydrogen Sulfide and Cellular Redox Homeostasis. *Oxid. Med. Cell. Longev.* **2016**, (2016).

69. Pietri, R., Román-Morales, E. & López-Garriga, J. Hydrogen Sulfide and Hemeproteins: Knowledge and Mysteries. *Antioxid. Redox Signal.* **15**, 393–404 (2011).

70. Guo, S., Zhang, Y., Lian, J., Su, C. & Wang, H. The role of hydrogen sulfide in the regulation of necroptosis across various pathological processes. *Mol. Cell. Biochem.* **480**, 1999–2013 (2025).

71. Zhang, Y. *et al.* The role of hydrogen sulfide regulation of pyroptosis in different pathological processes. *Eur. J. Med. Chem.* **268**, 116254 (2024).

72. Lian, J., Chen, Y., Zhang, Y., Guo, S. & Wang, H. The role of hydrogen sulfide regulation of ferroptosis in different diseases. *Apoptosis* **29**, 1377–1392 (2024).

73. Mustafa, A. K. *et al.* H 2 S Signals Through Protein S-Sulfhydration. *Sci. Signal.* **2**, (2009).

74. Austgen, J. R., Hermann, G. E., Dantzler, H. A., Rogers, R. C. & Kline, D. D. Hydrogen sulfide augments synaptic neurotransmission in the nucleus of the solitary tract. *J. Neurophysiol.* **106**, 1822–32 (2011).

75. Altaany, Z., Ju, Y., Yang, G. & Wang, R. The coordination of S-sulfhydration, S-nitrosylation, and phosphorylation of endothelial nitric oxide synthase by hydrogen sulfide. *Sci. Signal.* **7**, (2014).

76. Dugbartey, G. J. Physiological role of hydrogen sulfide in the kidney and its therapeutic implications for kidney diseases. *Biomed. Pharmacother.* **166**, 115396 (2023).

77. Linden, D. R. Hydrogen Sulfide Signaling in the Gastrointestinal Tract. *Antioxid. Redox Signal.* **20**, 818–830 (2014).

78. Li, L. *et al.* Hydrogen sulfide is a novel mediator of lipopolysaccharide-induced inflammation in the mouse. *FASEB J.* **19**, 1196–1198 (2005).

79. Zivanovic, J. *et al.* Selective Persulfide Detection Reveals Evolutionarily Conserved Antiaging Effects of S-Sulfhydration. *Cell Metab.* **30**, 1152-1170.e13 (2019).

80. Warenycia, M. W. *et al.* Acute hydrogen sulfide poisoning. *Biochem. Pharmacol.* **38**, 973–981 (1989).

81. Linden, D. *et al.* Sulphide quinone reductase contributes to hydrogen sulphide metabolism in murine peripheral tissues but not in the CNS. *Br. J. Pharmacol.* **165**, 2178–2190 (2012).

82. Marutani, E. *et al.* Sulfide catabolism ameliorates hypoxic brain injury. *Nat. Commun.* **12**, (2021).

83. Yellen, G. Fueling thought: Management of glycolysis and oxidative phosphorylation in neuronal metabolism. *J. Cell Biol.* **217**, 2235–2246 (2018).

84. Lagoutte, E. *et al.* Oxidation of hydrogen sulfide remains a priority in mammalian cells and causes reverse electron transfer in colonocytes. *Biochim. Biophys. Acta* **1797**, 1500–1511 (2010).

85. Deng, G. *et al.* Protective Effect of Hydrogen Sulfide on Cerebral Ischemia–Reperfusion Injury. *Cell. Mol. Neurobiol.* **43**, 15–25 (2023).

86. Luo, Y. *et al.* Hydrogen sulfide prevents OGD/R-induced apoptosis via improving mitochondrial dysfunction and suppressing an ROS-mediated caspase-3 pathway in cortical neurons. *Neurochem. Int.* **63**, 826–831 (2013).

87. Yin, J. *et al.* Exogenous hydrogen sulfide protects against global cerebral ischemia/reperfusion injury via its anti-oxidative, anti-inflammatory and anti-apoptotic effects in rats. *Brain Res.* **1491**, 188–196 (2013).

88. Marutani, E. *et al.* Sulfide catabolism ameliorates hypoxic brain injury. *Nat. Commun. 2021 121* **12**, 1–19 (2021).

89. Garrett, R. M., Johnson, J. L., Graf, T. N., Feigenbaum, A. & Rajagopalan, K. V. Human sulfite oxidase R160Q: Identification of the mutation in a sulfite oxidase-deficient patient and expression and characterization of the mutant enzyme. *Proc. Natl. Acad. Sci.* **95**, 6394–6398 (1998).

90. Kanemaru, E. & Ichinose, F. Essential role of sulfide oxidation in brain health and neurological disorders. *Pharmacol. Ther.* **266**, 108787 (2025).

91. Misko, A., Mahtani, K., Abbott, J., Schwarz, G. & Atwal, P. *Molybdenum Cofactor Deficiency*. *GeneReviews*® (1993).

92. Panagaki, T., Randi, E. B., Augsburger, F. & Szabo, C. Overproduction of H 2 S, generated by CBS, inhibits mitochondrial Complex IV and suppresses oxidative phosphorylation in Down syndrome. *Proc. Natl. Acad. Sci.* **116**, 18769–18771 (2019).

93. Szabo, C. The re-emerging pathophysiological role of the cystathionine-β-synthase - hydrogen sulfide system in Down syndrome. *FEBS J.* **287**, 3150–3160 (2020).

94. Friederich, M. W. *et al.* Pathogenic variants in <scp> *SQOR* </scp> encoding sulfide:quinone oxidoreductase are a potentially treatable cause of Leigh disease. *J. Inherit. Metab. Dis.* **43**, 1024–1036 (2020).

95. Kanemaru, E. *et al.* Exclusion of sulfide:quinone oxidoreductase from mitochondria causes Leigh-like disease in mice by impairing sulfide metabolism. *J. Clin. Invest.* **134**, (2024).

96. Tiranti, V. *et al.* Loss of ETHE1, a mitochondrial dioxygenase, causes fatal sulfide toxicity in ethylmalonic encephalopathy. *Nat. Med.* **15**, 200–205 (2009).

97. Di Meo, I. *et al.* Chronic Exposure to Sulfide Causes Accelerated Degradation of Cytochrome c Oxidase in Ethylmalonic Encephalopathy. *Antioxid. Redox Signal.* **15**, 353–362 (2011).

98. Ersoy, M., Tiranti, V. & Zeviani, M. Ethylmalonic encephalopathy: Clinical course and therapy response in an uncommon mild case with a severe ETHE1 mutation. *Mol. Genet. Metab. Reports* **25**, 100641 (2020).

99. Stipanuk, M. H. & Beck, P. W. Characterization of the enzymic capacity for cysteine desulphhydration in liver and kidney of the rat. *Biochem. J.* **206**, 267–277 (1982).

100. Feliers, D., Lee, H. J. & Kasinath, B. S. Hydrogen Sulfide in Renal Physiology and Disease. *Antioxid. Redox Signal.* **25**, 720–731 (2016).

101. Bos, E. M. *et al.* Cystathionine γ-Lyase Protects against Renal Ischemia/Reperfusion by Modulating Oxidative Stress. *J. Am. Soc. Nephrol.* **24**, 759–770 (2013).

102. Lee, H. J. *et al.* Hydrogen Sulfide Inhibits High Glucose-induced Matrix Protein Synthesis by Activating AMP-activated Protein Kinase in Renal Epithelial Cells. *J. Biol. Chem.* **287**, 4451–4461 (2012).

103. Yuan, X. *et al.* Loss of the Protein Cystathionine β-Synthase During Kidney Injury Promotes Renal Tubulointerstitial Fibrosis. *Kidney Blood Press. Res.* **42**, 428–443 (2017).

104. Zhou, X., Feng, Y., Zhan, Z. & Chen, J. Hydrogen Sulfide Alleviates Diabetic Nephropathy in a Streptozotocin-induced Diabetic Rat Model. *J. Biol. Chem.* **289**, 28827–28834 (2014).

105. Schumann, U. & Subramani, S. Special delivery from mitochondria to peroxisomes. *Trends Cell Biol.* **18**, 253–256 (2008).

106. Shibuya, N. & Kimura, H. Production of hydrogen sulfide from d-cysteine and its therapeutic potential. *Front. Endocrinol. (Lausanne).* **4**, 87 (2013).

107. Fukasawa, Y. *et al.* Identification and Characterization of a Na+-independent Neutral Amino Acid Transporter That Associates with the 4F2 Heavy Chain and Exhibits Substrate Selectivity for Small Neutral d- and l-Amino Acids. *J. Biol. Chem.* **275**, 9690–9698 (2000).

108. Lee, G., Hosgood, S. A., Patel, M. S. & Nicholson, M. L. Hydrogen sulphide as a novel therapy to ameliorate cyclosporine nephrotoxicity. *J. Surg. Res.* **197**, 419–426 (2015).

109. Pushpakumar, S., Kundu, S. & Sen, U. Hydrogen Sulfide Protects Hyperhomocysteinemia-Induced Renal Damage by Modulation of Caveolin and eNOS Interaction. *Sci. Rep.* **9**, 2223 (2019).

110. Xia, M., Chen, L., Muh, R. W., Li, P.-L. & Li, N. Production and Actions of Hydrogen Sulfide, a Novel Gaseous Bioactive Substance, in the Kidneys. *J. Pharmacol. Exp. Ther.* **329**, 1056–1062 (2009).

111. Ge, S.-N. *et al.* Hydrogen Sulfide Targets EGFR Cys797/Cys798 Residues to Induce Na + /K + -ATPase Endocytosis and Inhibition in Renal Tubular Epithelial Cells and Increase Sodium Excretion in Chronic Salt-Loaded Rats. *Antioxid. Redox Signal.* **21**, 2061–2082 (2014).

112. Sun, X., Chen, W. D. & Wang, Y. D. DAF-16/FOXO transcription factor in aging and longevity. *Frontiers in Pharmacology* vol. 8 at https://doi.org/10.3389/fphar.2017.00548 (2017).

113. Kuang, Q. *et al.* Low Plasma Hydrogen Sulfide Is Associated with Impaired Renal Function and Cardiac Dysfunction. *Am. J. Nephrol.* **47**, 361–371 (2018).

114. Wang, R. *et al.* The role of H2S bioavailability in endothelial dysfunction. *Trends Pharmacol. Sci.* **36**, 568–578 (2015).

115. Yuan, G. *et al.* Protein kinase G–regulated production of H 2 S governs oxygen sensing. *Sci. Signal.* **8**, (2015).

116. Susantitaphong, P. *et al.* World Incidence of AKI: A Meta-Analysis. *Clin. J. Am. Soc. Nephrol.* **8**, 1482–1493 (2013).

117. Turgut, F., Awad, A. & Abdel-Rahman, E. Acute Kidney Injury: Medical Causes and Pathogenesis. *J. Clin. Med.* **12**, 375 (2023).

118. Emre Aydıngöz, S. *et al.* Effect of hydrogen sulfide on ischemia-reperfusion injury of kidney: A systematic review and meta-analysis of in vivo animal studies.

Eur. J. Pharmacol. **943**, 175564 (2023).

119. Ngowi, E. E. *et al.* Roles of Hydrogen Sulfide Donors in Common Kidney Diseases. *Front. Pharmacol.* **11**, (2020).

120. Hashmi, S. *et al.* Hydrogen Sulphide Treatment Prevents Renal Ischemia-Reperfusion Injury by Inhibiting the Expression of ICAM-1 and NF-kB Concentration in Normotensive and Hypertensive Rats. *Biomolecules* **11**, 1549 (2021).

121. Ahmad, A. *et al.* AP39, A Mitochondrially Targeted Hydrogen Sulfide Donor, Exerts Protective Effects in Renal Epithelial Cells Subjected to Oxidative Stress in Vitro and in Acute Renal Injury in Vivo. *Shock* **45**, 88–97 (2016).

122. Cao, X. & Bian, J.-S. The Role of Hydrogen Sulfide in Renal System. *Front. Pharmacol.* **7**, (2016).

123. Han, S. J., Kim, J. I., Park, J.-W. & Park, K. M. Hydrogen sulfide accelerates the recovery of kidney tubules after renal ischemia/reperfusion injury. *Nephrol. Dial. Transplant.* **30**, 1497–1506 (2015).

124. Bełtowski, J. Hypoxia in the Renal Medulla: Implications for Hydrogen Sulfide Signaling. *J. Pharmacol. Exp. Ther.* **334**, 358–363 (2010).

125. Feng, Q. *et al.* Ferroptosis and Acute Kidney Injury (AKI): Molecular Mechanisms and Therapeutic Potentials. *Front. Pharmacol.* **13**, 858676 (2022).

126. Sun, X. *et al.* Therapeutic Potential of Hydrogen Sulfide in Ischemia and Reperfusion Injury. *Biomolecules* **14**, 740 (2024).

127. Brodnitz, M. H., Pascale, J. V. & Van Derslice, L. Flavor components of garlic extract. *J. Agric. Food Chem.* **19**, 273–275 (1971).

128. Pan, L., Wang, X., Wang, X., Molecular, Y. Z.-I. J. of & 2014, undefined. Sodium hydrosulfide prevents myocardial dysfunction through modulation of extracellular matrix accumulation and vascular density. *mdpi.com* **15**, 15 (2014).

129. Zhao, W. The vasorelaxant effect of H2S as a novel endogenous gaseous KATP channel opener. *EMBO J.* **20**, 6008–6016 (2001).

130. Lee, Z. W. *et al.* The Slow-Releasing Hydrogen Sulfide Donor, GYY4137, Exhibits Novel Anti-Cancer Effects In Vitro and In Vivo. *PLoS One* **6**, e21077 (2011).

131. Szabó, C. Hydrogen sulphide and its therapeutic potential. *Nat. Rev. Drug Discov.* **6**, 917–935 (2007).

132. Szabo, C. & Papapetropoulos, A. International Union of Basic and Clinical Pharmacology. CII: Pharmacological Modulation of H2S Levels: H2S Donors and H2S Biosynthesis Inhibitors. *Pharmacol. Rev.* **69**, 497–564 (2017).

133. Han, S. J., Kim, J. I., Park, J.-W. & Park, K. M. Hydrogen sulfide accelerates the recovery of kidney tubules after renal ischemia/reperfusion injury. *Nephrol. Dial.*

Transplant **30**, 1497–506 (2015).

134. Jha, S., Calvert, J. W., Duranski, M. R., Ramachandran, A. & Lefer, D. J. Hydrogen sulfide attenuates hepatic ischemia-reperfusion injury: role of antioxidant and antiapoptotic signaling. *Am. J. Physiol. Circ. Physiol.* **295**, H801–H806 (2008).

135. Xie, L. *et al.* Hydrogen Sulfide Induces Keap1 S-sulfhydration and Suppresses Diabetes-Accelerated Atherosclerosis via Nrf2 Activation. *Diabetes* **65**, 3171–3184 (2016).

136. Liu, Z., Wang, X., Li, L., Wei, G. & Zhao, M. Hydrogen Sulfide Protects against Paraquat-Induced Acute Liver Injury in Rats by Regulating Oxidative Stress, Mitochondrial Function, and Inflammation. *Oxid. Med. Cell. Longev.* **2020**, 1–16 (2020).

137. Guo, C., Liang, F., Shah Masood, W. & Yan, X. Hydrogen sulfide protected gastric epithelial cell from ischemia/reperfusion injury by Keap1 s-sulfhydration, MAPK dependent anti-apoptosis and NF-κB dependent anti-inflammation pathway. *Eur. J. Pharmacol.* **725**, 70–78 (2014).

138. Huang, P. *et al.* Hydrogen Sulfide Inhibits High-Salt Diet-Induced Renal Oxidative Stress and Kidney Injury in Dahl Rats. *Oxid. Med. Cell. Longev.* **2016**, (2016).

139. Zhao, S. *et al.* Hydrogen Sulfide Alleviates Liver Injury Through the S-Sulfhydrated-Kelch-Like ECH-Associated Protein 1/Nuclear Erythroid 2–Related Factor 2/Low-Density Lipoprotein Receptor–Related Protein 1 Pathway. *Hepatology* **73**, 282–302 (2021).

140. Feng, J., Lu, X., Li, H. & Wang, S. The roles of hydrogen sulfide in renal physiology and disease states. *Ren. Fail.* **44**, 1290–1309 (2022).

141. Emre Aydıngöz, S., Teimoori, A., Orhan, H. G., Demirtaş, E. & Zeynalova, N. A meta-analysis of animal studies evaluating the effect of hydrogen sulfide on ischemic stroke: is the preclinical evidence sufficient to move forward? *Naunyn. Schmiedebergs. Arch. Pharmacol.* **397**, 9533–9548 (2024).

142. Roorda, M., Miljkovic, J. L., van Goor, H., Henning, R. H. & Bouma, H. R. Spatiotemporal regulation of hydrogen sulfide signaling in the kidney. *Redox Biol.* **43**, 101961 (2021).

143. Ikeda, K. *et al.* Mitochondria-targeted hydrogen sulfide donor AP39 improves neurological outcomes after cardiac arrest in mice. *Nitric Oxide* **49**, 90–96 (2015).

144. Liang, D., Wu, H., Wong, M. W. & Huang, D. Diallyl Trisulfide Is a Fast H 2 S Donor, but Diallyl Disulfide Is a Slow One: The Reaction Pathways and Intermediates of Glutathione with Polysulfides. *Org. Lett.* **17**, 4196–4199 (2015).

145. Gojon, G. & Morales, G. A. SG1002 and Catenated Divalent Organic Sulfur Compounds as Promising Hydrogen Sulfide Prodrugs. *Antioxid. Redox Signal.* **33**, 1010–1045 (2020).

146. Powolny, A. A., Singh, S. V., Melov, S., Hubbard, A. & Fisher, A. L. The garlic constituent diallyl trisulfide increases the lifespan of C. elegans via skn-1 activation. *Exp. Gerontol.* **46**, 441–452 (2011).

147. Petrovic, D. *et al.* Ergothioneine improves healthspan of aged animals by enhancing cGPDH activity through CSE-dependent persulfidation. *Cell Metab.* **37**, 542-556.e14 (2025).

148. Sprenger, H.-G. *et al.* Ergothioneine controls mitochondrial function and exercise performance via direct activation of MPST. *Cell Metab.* **37**, 857-869.e9 (2025).

149. Ng, L. T. *et al.* Lifespan and healthspan benefits of exogenous H2S in C. elegans are independent from effects downstream of eat-2 mutation. *npj Aging Mech. Dis. 2020 61* **6**, 1–14 (2020).

150. Qabazard, B. *et al.* C. elegans Aging Is Modulated by Hydrogen Sulfide and the sulfhydrylase/cysteine Synthase cysl-2. *PLoS One* **8**, e80135 (2013).

151. Vintila, A. R. *et al.* Mitochondrial sulfide promotes life span and health span through distinct mechanisms in developing versus adult treated Caenorhabditis elegans. *Proc. Natl. Acad. Sci. U. S. A.* **120**, e2216141120 (2023).

152. Wilkie, S. E., Borland, G., Carter, R. N., Morton, N. M. & Selman, C. Hydrogen sulfide in ageing, longevity and disease. *Biochem. J.* **478**, 3485–3504 (2021).

153. Sokolov, A. S., Nekrasov, P. V., Shaposhnikov, M. V. & Moskalev, A. A. Hydrogen sulfide in longevity and pathologies: Inconsistency is malodorous. *Ageing Res. Rev.* **67**, 101262 (2021).

154. Latorre, E., Torregrossa, R., Wood, M. E., Whiteman, M. & Harries, L. W. Mitochondria-targeted hydrogen sulfide attenuates endothelial senescence by selective induction of splicing factors HNRNPD and SRSF2. *Aging (Albany. NY).* **10**, 1666–1681 (2018).

155. Li, J. *et al.* Activatable and Self-Monitoring Hydrogen Sulfide-Based Molecular Senomorphics for Visualized Regulation of Cellular Senescence. *CCS Chem.* **5**, 2897–2909 (2023).

156. de la Torre, C. & Villamor, P. Chemically Assisted Dissection With Sodium 2-Mercaptoethanesulfonate (MESNA) in the Surgical Management of Pediatric Cholesteatoma. *Otol. Neurotol.* **40**, 645–650 (2019).

157. Vinknes, K. J. *et al.* Cysteine-lowering treatment with mesna against obesity: Proof of concept and results from a human phase I, dose-finding study. *Diabetes, Obes. Metab.* **25**, 3161–3170 (2023).

158. Philipp, T. M. *et al.* Mechanism of action and impact of thiol homeostasis on efficacy of an enzyme replacement therapy for classical homocystinuria. *Redox Biol.* **77**, 103383 (2024).

159. Cutler, M. J. *et al.* Enzymatic and non-enzymatic mechanisms of dimesna metabolism. *Amino Acids* **47**, 511–523 (2015).

160. Hristov, B. D. The Role of Glutathione Metabolism in Chronic Illness Development and Its Potential Use as a Novel Therapeutic Target. *Cureus* **14**, e29696 (2022).

161. Wolfe, R. S. & McBride, B. C. New coenzyme of methyl transfer, coenzyme M. *Biochemistry* **10**, 2317–2324 (1971).

162. Wu, H.-H. *et al.* The pathway for coenzyme M biosynthesis in bacteria. *Proc. Natl. Acad. Sci.* **119**, (2022).

163. Jaiswal, S. R. *et al.* Impact of extended infusional mesna prophylaxis on the incidence of BK viruria and hemorrhagic cystitis following post-transplantation cyclophosphamide and CTLA4Ig-based haploidentical transplantation. *Ann. Hematol.* **99**, 839–845 (2020).

164. Ismi, O., Karabulut, Y. Y., Bal, K. K., Vayisoglu, Y. & Unal, M. Single dose intratympanic mesna application inhibits propylene glycol induced cholesteatoma formation. *J. Laryngol. Otol.* **131**, 215–220 (2017).

165. Carassiti, M. *et al.* Failed back surgery syndrome: a new strategy by the epidural injection of MESNA. *Musculoskelet. Surg.* **102**, 179–184 (2018).

166. de la Torre, C. & Villamor, P. Chemically Assisted Dissection With Sodium 2-Mercaptoethanesulfonate (MESNA) in the Surgical Management of Pediatric Cholesteatoma. *Otol. Neurotol.* **40**, 645–650 (2019).

167. Tasar, P. & Ozen, Y. Effects of Recombinant Human Erythropoietin and 2-Mercaptoethane Sulfonate on Liver Ischemia-Reperfusion Injury in Rats. *Exp. Clin. Transplant.* **22**, 358–365 (2024).

168. Sener, G. *et al.* Protective Effect of MESNA (2-Mercaptoethane Sulfonate) Against Hepatic Ischemia/Reperfusion Injury in Rats. *Surg. Today* **35**, 575–580 (2005).

169. Cargnoni, A. *et al.* The effects of L-arginine mono(2-mercaptoethanesulfonate) on the ischemic and reperfused heart. *Cardioscience* **3**, 179–87 (1992).

170. Abd El-Baset, S. A., Abd El-haleem, M. R., Abdul-Maksoud, R. S. & Kattaia, A. A. A. Mesna ameliorates acute lung injury induced by intestinal ischemia–reperfusion in rats. *Sci. Rep.* **11**, 13356 (2021).

171. Ypsilantis, P. *et al.* Mesna Protects Intestinal Mucosa from Ischemia/Reperfusion Injury. *J. Surg. Res.* **134**, 278–284 (2006).

172. Dolgun, H. *et al.* Neuroprotective effect of mesna (2-mercaptoethane sulfonate) against spinal cord ischemia/reperfusion injury in rabbits. *J. Clin. Neurosci.* **17**, 486–489 (2010).

173. Moon, D., Padanilam, B. J., Jang, H.-S. & Kim, J. 2-Mercaptoethanol protects against DNA double-strand breaks after kidney ischemia and reperfusion injury through GPX4 upregulation. *Pharmacol. Reports* **74**, 1041–1053 (2022).

174. Mercan, M. *et al.* MESNA (2-Mercaptoethanesulfonate) Attenuates Brain, Heart,

and Lung Injury Induced by Carotid Ischemia-Reperfusion in Rats. *Niger. J. Clin. Pract.* **26**, 941–948 (2023).

175. Kabasakal, L. *et al.* Mesna (2-mercaptoethane sulfonate) prevents ischemia/reperfusion induced renal oxidative damage in rats. *Life Sci.* **75**, 2329–2340 (2004).

176. Mashiach, E. *et al.* Mesna: a novel renoprotective antioxidant in ischaemic acute renal failure. *Nephrol. Dial. Transplant.* **16**, 542–551 (2001).

177. Yiannakopoulou, E., Nikiteas, N., Perrea, D. & Tsigris, C. Pharmacological Modulation of Oxidative Stress Response in Minimally Invasive Surgery. *Surg. Laparosc. Endosc. Percutan. Tech.* **22**, 200–204 (2012).

178. Kabasakal, L. *et al.* Mesna (2-mercaptoethane sulfonate) prevents ischemia/reperfusion induced renal oxidative damage in rats. *Life Sci.* **75**, 2329–40 (2004).

179. Cutler, M. J. *et al.* Enzymatic and non-enzymatic mechanisms of dimesna metabolism. *Amino Acids* **47**, 511–523 (2015).

180. Kaelin, W. G. & Ratcliffe, P. J. Oxygen Sensing by Metazoans: The Central Role of the HIF Hydroxylase Pathway. *Mol. Cell* **30**, 393–402 (2008).

181. Semenza, G. L. Oxygen Sensing, Hypoxia-Inducible Factors, and Disease Pathophysiology. *Annu. Rev. Pathol. Mech. Dis.* **9**, 47–71 (2014).

182. Taylor, C. T. & Scholz, C. C. The effect of HIF on metabolism and immunity. *Nat. Rev. Nephrol.* **18**, 573–587 (2022).

183. Lu, G. & Shao, G. Hypoxic preconditioning: effect, mechanism and clinical implication (Part 1). *Zhongguo Ying Yong Sheng Li Xue Za Zhi* **30**, 489–501 (2014).

184. Scholz, H. *et al.* Kidney physiology and susceptibility to acute kidney injury: implications for renoprotection. *Nat. Rev. Nephrol.* **17**, 335–349 (2021).

185. Honda, T., Hirakawa, Y. & Nangaku, M. The role of oxidative stress and hypoxia in renal disease. *Kidney Res. Clin. Pract.* **38**, 414–426 (2019).

186. Suzuki, N., Gradin, K., Poellinger, L. & Yamamoto, M. Regulation of hypoxia-inducible gene expression after HIF activation. *Exp. Cell Res.* **356**, 182–186 (2017).

187. Maxwell, P. H. *et al.* The tumour suppressor protein VHL targets hypoxia-inducible factors for oxygen-dependent proteolysis. *Nature* **399**, 271–275 (1999).

188. Bishop, T. *et al.* Genetic Analysis of Pathways Regulated by the von Hippel-Lindau Tumor Suppressor in Caenorhabditis elegans. *PLOS Biol.* **2**, e289 (2004).

189. McNeill, L. A. *et al.* The use of dioxygen by HIF prolyl hydroxylase (PHD1).

Bioorg. Med. Chem. Lett. **12**, 1547–1550 (2002).

190. Semenza, G. L. Hypoxia-Inducible Factor 1 (HIF-1) Pathway. *Sci. STKE* **2007**, (2007).

191. Kunej, T. Integrative Map of HIF1A Regulatory Elements and Variations. *Genes (Basel).* **12**, 1526 (2021).

192. Webb, J. D., Coleman, M. L. & Pugh, C. W. Hypoxia, hypoxia-inducible factors (HIF), HIF hydroxylases and oxygen sensing. *Cell. Mol. Life Sci.* **66**, 3539–3554 (2009).

193. Xiao, W., Wang, R.-S., Handy, D. E. & Loscalzo, J. NAD(H) and NADP(H) Redox Couples and Cellular Energy Metabolism. *Antioxid. Redox Signal.* **28**, 251–272 (2018).

194. Guzy, R. D. *et al.* Mitochondrial complex III is required for hypoxia-induced ROS production and cellular oxygen sensing. *Cell Metab.* **1**, 401–8 (2005).

195. Papandreou, I., Cairns, R. A., Fontana, L., Lim, A. L. & Denko, N. C. HIF-1 mediates adaptation to hypoxia by actively downregulating mitochondrial oxygen consumption. *Cell Metab.* **3**, 187–197 (2006).

196. Kim, J., Tchernyshyov, I., Semenza, G. L. & Dang, C. V. HIF-1-mediated expression of pyruvate dehydrogenase kinase: A metabolic switch required for cellular adaptation to hypoxia. *Cell Metab.* **3**, 177–185 (2006).

197. Semenza, G. L. *et al.* Hypoxia Response Elements in the Aldolase A, Enolase 1, and Lactate Dehydrogenase A Gene Promoters Contain Essential Binding Sites for Hypoxia-inducible Factor 1. *J. Biol. Chem.* **271**, 32529–32537 (1996).

198. Samanta, D. & Semenza, G. L. Metabolic adaptation of cancer and immune cells mediated by hypoxia-inducible factors. *Biochim. Biophys. Acta - Rev. Cancer* **1870**, 15–22 (2018).

199. Zhang, H. *et al.* HIF-1 Inhibits Mitochondrial Biogenesis and Cellular Respiration in VHL-Deficient Renal Cell Carcinoma by Repression of C-MYC Activity. *Cancer Cell* **11**, 407–420 (2007).

200. Dominiak, K., Galganski, L., Budzinska, A. & Jarmuszkiewicz, W. Coenzyme Q deficiency in endothelial mitochondria caused by hypoxia; remodeling of the respiratory chain and sensitivity to anoxia/reoxygenation. *Free Radic. Biol. Med.* **214**, 158–170 (2024).

201. Acín-Pérez, R., Fernández-Silva, P., Peleato, M. L., Pérez-Martos, A. & Enriquez, J. A. Respiratory active mitochondrial supercomplexes. *Mol. Cell* **32**, 529–39 (2008).

202. Bellot, G. *et al.* Hypoxia-Induced Autophagy Is Mediated through Hypoxia-Inducible Factor Induction of BNIP3 and BNIP3L via Their BH3 Domains. *Mol. Cell. Biol.* **29**, 2570–2581 (2009).

203. Dzhalilova, D. S. & Makarova, O. V. The Role of Hypoxia-Inducible Factor in the

Mechanisms of Aging. *Biochemistry. (Mosc).* **87**, 995–1014 (2022).

204. Ahluwalia, A., Jones, M. K., Szabo, S. & Tarnawski, A. S. Aging impairs transcriptional regulation of vascular endothelial growth factor in human microvascular endothelial cells: implications for angiogenesis and cell survival. *J. Physiol. Pharmacol.* **65**, 209–15 (2014).

205. Yeo, E.-J. Hypoxia and aging. *Exp. Mol. Med.* **51**, 1–15 (2019).

206. Leiser, S. F. & Kaeberlein, M. The hypoxia-inducible factor HIF-1 functions as both a positive and negative modulator of aging. *Biol. Chem.* **391**, 1131–7 (2010).

207. Zhang, Y., Shao, Z., Zhai, Z., Shen, C. & Powell-Coffman, J. A. The HIF-1 hypoxia-inducible factor modulates lifespan in C. elegans. *PLoS One* **4**, e6348 (2009).

208. Vigne, P. & Frelin, C. A Low Protein Diet Increases the Hypoxic Tolerance in Drosophila. *PLoS One* **1**, e56 (2006).

209. Wang, R. *et al.* Hypoxic Training in Obese Mice Improves Metabolic Disorder. *Front. Endocrinol. (Lausanne).* **10**, 527 (2019).

210. Xiao, B. *et al.* HIF-1α contributes to hypoxia adaptation of the naked mole rat. *Oncotarget* **8**, 109941–109951 (2017).

211. Brenner, S. The genetics of Caenorhabditis elegans. *Genetics* **77**, 71–94 (1974).

212. Kaletta, T. & Hengartner, M. O. Finding function in novel targets: C. elegans as a model organism. *Nat. Rev. Drug Discov.* **5**, 387–399 (2006).

213. Sulston, J. E. & Horvitz, H. R. Post-embryonic cell lineages of the nematode, Caenorhabditis elegans. *Dev. Biol.* **56**, 110–56 (1977).

214. Sulston, J. E., Schierenberg, E., White, J. G. & Thomson, J. N. The embryonic cell lineage of the nematode Caenorhabditis elegans. *Dev. Biol.* **100**, 64–119 (1983).

215. Johnstone, I. L. The cuticle of the nematode Caenorhabditis elegans: a complex collagen structure. *Bioessays* **16**, 171–8 (1994).

216. Hill, K. L., Harfe, B. D., Dobbins, C. A. & L'Hernault, S. W. dpy-18 encodes an alpha-subunit of prolyl-4-hydroxylase in caenorhabditis elegans. *Genetics* **155**, 1139–48 (2000).

217. Cassada, R. C. & Russell, R. L. The dauerlarva, a post-embryonic developmental variant of the nematode Caenorhabditis elegans. *Dev. Biol.* **46**, 326–42 (1975).

218. Ward, S. & Carrel, J. S. Fertilization and sperm competition in the nematodeCaenorhabditis elegans. *Dev. Biol.* **73**, 304–321 (1979).

219. The C. elegans Sequencing Consortium. Genome Sequence of the Nematode

Caenorhabditis elegans: A Platform for Investigating Biology. *Science (80-.).* **282**, 2012–2018 (1998).

220. Lai, C. H., Chou, C. Y., Ch'ang, L. Y., Liu, C. S. & Lin, W. Identification of novel human genes evolutionarily conserved in Caenorhabditis elegans by comparative proteomics. *Genome Res.* **10**, 703–13 (2000).

221. Epstein, A. C. R. *et al.* C. elegans EGL-9 and Mammalian Homologs Define a Family of Dioxygenases that Regulate HIF by Prolyl Hydroxylation. *Cell* **107**, 43–54 (2001).

222. Jiang, H., Guo, R. & Powell-Coffman, J. A. The Caenorhabditis elegans hif-1 gene encodes a bHLH-PAS protein that is required for adaptation to hypoxia. *Proc. Natl. Acad. Sci. U. S. A.* **98**, 7916–21 (2001).

223. Mehta, R. *et al.* Proteasomal regulation of the hypoxic response modulates aging in C. elegans. *Science* **324**, 1196–8 (2009).

224. Müller, R. U. *et al.* The von Hippel Lindau tumor suppressor limits longevity. *J. Am. Soc. Nephrol.* **20**, 2513–2517 (2009).

225. Feng, D., Qu, L. & Powell-Coffman, J. A. Whole genome profiling of short-term hypoxia induced genes and identification of HIF-1 binding sites provide insights into HIF-1 function in Caenorhabditis elegans. *PLoS One* **19**, e0295094 (2024).

226. Vora, M. *et al.* The hypoxia response pathway promotes PEP carboxykinase and gluconeogenesis in C. elegans. *Nat. Commun.* **13**, 6168 (2022).

227. Luhachack, L. G. *et al.* EGL-9 controls C. elegans host defense specificity through prolyl hydroxylation-dependent and -independent HIF-1 pathways. *PLoS Pathog.* **8**, e1002798 (2012).

228. Kruempel, J. C. P. *et al.* Hypoxic response regulators RHY-1 and EGL-9/PHD promote longevity through a VHL-1-independent transcriptional response. *GeroScience* **42**, 1621–1633 (2020).

229. Horsman, J. W., Heinis, F. I. & Miller, D. L. A Novel Mechanism To Prevent H2S Toxicity in Caenorhabditis elegans. *Genetics* **213**, 481–490 (2019).

230. Shen, C., Nettleton, D., Jiang, M., Kim, S. K. & Powell-Coffman, J. A. Roles of the HIF-1 hypoxia-inducible factor during hypoxia response in Caenorhabditis elegans. *J. Biol. Chem.* **280**, 20580–8 (2005).

231. Shen, C., Shao, Z. & Powell-Coffman, J. A. The Caenorhabditis elegans rhy-1 gene inhibits HIF-1 hypoxia-inducible factor activity in a negative feedback loop that does not include vhl-1. *Genetics* **174**, 1205–1214 (2006).

232. Leiser, S. F., Begun, A. & Kaeberlein, M. HIF-1 modulates longevity and healthspan in a temperature-dependent manner. *Aging Cell* **10**, 318–326 (2011).

233. Wen, H., Yu, Y., Zhu, G., Jiang, L. & Qin, J. A droplet microchip with substance exchange capability for the developmental study of C. elegans. *Lab Chip* **15**, 1905–11 (2015).

234. Chen, R. *et al.* Reactive Oxygen Species Formation in the Brain at Different Oxygen Levels: The Role of Hypoxia Inducible Factors. *Front. Cell Dev. Biol.* **6**, (2018).

235. Pham, K., Parikh, K. & Heinrich, E. C. Hypoxia and Inflammation: Insights From High-Altitude Physiology. *Front. Physiol.* **12**, (2021).

236. Prabhakar, N. R., Peng, Y.-J., Yuan, G. & Nanduri, J. Reactive oxygen radicals and gaseous transmitters in carotid body activation by intermittent hypoxia. *Cell Tissue Res.* **372**, 427–431 (2018).

237. Wu, B. *et al.* Interaction of Hydrogen Sulfide with Oxygen Sensing under Hypoxia. *Oxid. Med. Cell. Longev.* **2015**, 758678 (2015).

238. Zhang, R., Shi, W., Wu, X., Yu, Q. & Xiao, Y. Application of hydrogen sulfide donor conjugates in different diseases. *Nitric oxide Biol. Chem.* **154**, 128–139 (2025).

239. Ma, D. K., Vozdek, R., Bhatla, N. & Horvitz, H. R. CYSL-1 Interacts with the O2-Sensing Hydroxylase EGL-9 to Promote H2S-Modulated Hypoxia-Induced Behavioral Plasticity in C. elegans. *Neuron* **73**, 925–940 (2012).

240. Budde, M. W. & Roth, M. B. The response of Caenorhabditis elegans to hydrogen sulfide and hydrogen cyanide. *Genetics* **189**, 521–32 (2011).

241. Budde, M. W. & Roth, M. B. Hydrogen sulfide increases hypoxia-inducible factor-1 activity independently of von Hippel-Lindau tumor suppressor-1 in C. elegans. *Mol. Biol. Cell* **21**, 212–217 (2010).

242. Budde, M. W. & Roth, M. B. Hydrogen sulfide increases hypoxia-inducible factor-1 activity independently of von Hippel-Lindau tumor suppressor-1 in C. elegans. *Mol. Biol. Cell* **21**, 212–217 (2010).

243. Forte, E. & Giuffrè, A. How bacteria breathe in hydrogen sulfide-rich environments. *Biochem. (Lond).* **38**, 8–11 (2016).

244. Filipovic, M. R., Zivanovic, J., Alvarez, B. & Banerjee, R. Chemical Biology of H 2 S Signaling through Persulfidation. *Chem. Rev.* **118**, 1253–1337 (2018).

245. Miller, D. L., Budde, M. W. & Roth, M. B. HIF-1 and SKN-1 Coordinate the Transcriptional Response to Hydrogen Sulfide in Caenorhabditis elegans. *PLoS One* **6**, e25476 (2011).

246. Miller, D. L., Budde, M. W. & Roth, M. B. HIF-1 and SKN-1 coordinate the transcriptional response to hydrogen sulfide in Caenorhabditis elegans. *PLoS One* **6**, (2011).

247. Miller, D. L. & Roth, M. B. Hydrogen sulfide increases thermotolerance and lifespan in Caenorhabditis elegans. *Proc. Natl. Acad. Sci.* **104**, 20618–20622 (2007).

248. Qabazard, B. *et al.* C. elegans aging is modulated by hydrogen sulfide and the sulfhydrylase/cysteine synthase cysl-2. *PLoS One* **8**, (2013).

249. Vintila, A. R. *et al.* Mitochondrial sulfide promotes life span and health span through distinct mechanisms in developing versus adult treated Caenorhabditis elegans. *Proc. Natl. Acad. Sci.* **120**, (2023).

250. Fox, B. C. *et al.* The mitochondria-targeted hydrogen sulfide donor AP39 improves health and mitochondrial function in a <scp> *C. elegans* </scp> primary mitochondrial disease model. *J. Inherit. Metab. Dis.* **44**, 367–375 (2021).

251. Hine, C. *et al.* Endogenous hydrogen sulfide production is essential for dietary restriction benefits. *Cell* **160**, 132–144 (2015).

252. Wei, Y. & Kenyon, C. Roles for ROS and hydrogen sulfide in the longevity response to germline loss in Caenorhabditis elegans. *Proc. Natl. Acad. Sci.* **113**, (2016).

253. Statzer, C. *et al.* ATF-4 and hydrogen sulfide signalling mediate longevity in response to inhibition of translation or mTORC1. *Nat. Commun.* **13**, 967 (2022).

254. Ng, L. T. *et al.* Lifespan and healthspan benefits of exogenous H2S in C. elegans are independent from effects downstream of eat-2 mutation. *npj Aging Mech. Dis.* **6**, 6 (2020).

255. Evans, R. G., Smith, D. W., Lee, C.-J., Ngo, J. P. & Gardiner, B. S. What Makes the Kidney Susceptible to Hypoxia? *Anat. Rec. (Hoboken).* **303**, 2544–2552 (2020).

256. Danese, S. *et al.* Randomised clinical trial: a phase 1b study of GB004, an oral HIF-1α stabiliser, for treatment of ulcerative colitis. *Aliment. Pharmacol. Ther.* **55**, 401–411 (2022).

257. Zhang, Q. *et al.* IL-27 regulates HIF-1α-mediated VEGFA response in macrophages of diabetic retinopathy patients and healthy individuals. *Cytokine* **113**, 238–247 (2019).

258. Chertow, G. M. *et al.* Vadadustat in Patients with Anemia and Non-Dialysis-Dependent CKD. *N. Engl. J. Med.* **384**, 1589–1600 (2021).

259. Duscher, D., Maan, Z. N., Hu, M. S. & Thor, D. A single-center blinded randomized clinical trial to evaluate the anti-aging effects of a novel HSF™-based skin care formulation. *J. Cosmet. Dermatol.* **19**, 2936–2945 (2020).

260. Timmons, L., Court, D. L. & Fire, A. Ingestion of bacterially expressed dsRNAs can produce specific and potent genetic interference in Caenorhabditis elegans. *Gene* **263**, 103–112 (2001).

261. Stroustrup, N. *et al.* The Caenorhabditis elegans Lifespan Machine. *Nat. Methods* **10**, 665–670 (2013).

262. Moore, B. T., Jordan, J. M. & Baugh, L. R. WormSizer: High-throughput Analysis of Nematode Size and Shape. *PLoS One* **8**, e57142 (2013).

263. Borbényi-Galambos, K. *et al.* Realigned transsulfuration drives BRAF-V600E-targeted therapy resistance in melanoma. *Cell Metab.* **37**, 1171-1188.e9 (2025).

264. Budde, M. W. & Roth, M. B. The Response of Caenorhabditis elegans to Hydrogen Sulfide and Hydrogen Cyanide. *Genetics* **189**, 521–532 (2011).

265. Smith, P. F., Booker, B. M., Creaven, P., Perez, R. & Pendyala, L. Pharmacokinetics and pharmacodynamics of mesna-mediated plasma cysteine depletion. *J. Clin. Pharmacol.* **43**, 1324–8 (2003).

266. Ali, S. A. *et al.* Comparision of uroprotective activity of reduced glutathione with mesna in ifosfamide induced hemorrhagic cystitis in rats. *Indian J. Pharmacol.* **46**, 105–8 (2014).

267. Vora, M. *et al.* The hypoxia response pathway promotes PEP carboxykinase and gluconeogenesis in C. elegans. *Nat. Commun.* **13**, 6168 (2022).

268. Fels, D. R. & Koumenis, C. The PERK/eIF2alpha/ATF4 module of the UPR in hypoxia resistance and tumor growth. *Cancer Biol. Ther.* **5**, 723–8 (2006).

269. Fawcett, E. M., Hoyt, J. M., Johnson, J. K. & Miller, D. L. Hypoxia disrupts proteostasis in Caenorhabditis elegans. *Aging Cell* **14**, 92–101 (2015).

270. Qabazard, B. *et al.* Hydrogen sulfide is an endogenous regulator of aging in Caenorhabditis elegans. *Antioxid. Redox Signal.* **20**, 2621–2630 (2014).

271. Romanelli-Credrez, L., Doitsidou, M., Alkema, M. J. & Salinas, G. HIF-1 Has a Central Role in Caenorhabditis elegans Organismal Response to Selenium. *Front. Genet.* **11**, (2020).

272. Valkova, N. & Kültz, D. Constitutive and inducible stress proteins dominate the proteome of the murine inner medullary collecting duct-3 (mIMCD3) cell line. *Biochim. Biophys. Acta - Proteins Proteomics* **1764**, 1007–1020 (2006).

273. Yang, X., Xiao, P. & Shi, X. Molecular mechanism of paraquat-induced ferroptosis leading to pulmonary fibrosis mediated by Keap1/Nrf2 signaling pathway. *Mol. Biol. Rep.* **50**, 9249–9261 (2023).

274. Seufert, L. Elucidating the role of Musashi RNA-binding proteins in tubular epithelial cells and acute kidney injury. (University of Cologne, 2023).

275. Ni, L., Yuan, C. & Wu, X. Targeting ferroptosis in acute kidney injury. *Cell Death Dis.* **13**, 182 (2022).

276. Alam, M. M. *et al.* Contribution of NRF2 to sulfur metabolism and mitochondrial activity. *Redox Biol.* **60**, 102624 (2023).

277. Zorova, L. D. *et al.* Mitochondrial membrane potential. *Anal. Biochem.* **552**, 50–59 (2018).

278. Kakadia, J. *et al.* Mechanisms linking hypoxia to phosphorylation of insulin-like growth factor binding protein-1 in baboon fetuses with intrauterine growth restriction and in cell culture. *FASEB J.* **35**, e21788 (2021).

279. Texada, M. J. *et al.* A fat-tissue sensor couples growth to oxygen availability by remotely controlling insulin secretion. *Nat. Commun.* **10**, 1955 (2019).

280. Yoon, D. *et al.* Increased size of solid organs in patients with Chuvash polycythemia and in mice with altered expression of HIF-1alpha and HIF-2alpha. *J. Mol. Med. (Berl).* **88**, 523–30 (2010).

281. Jun, J. C. *et al.* Adipose HIF-1α causes obesity by suppressing brown adipose tissue thermogenesis. *J. Mol. Med. (Berl).* **95**, 287–297 (2017).

282. Libiad, M., Yadav, P. K., Vitvitsky, V., Martinov, M. & Banerjee, R. Organization of the human mitochondrial hydrogen sulfide oxidation pathway. *J. Biol. Chem.* **289**, 30901–10 (2014).

283. Tobler, M. *et al.* Evolution in extreme environments: replicated phenotypic differentiation in livebearing fish inhabiting sulfidic springs. *Evolution* **65**, 2213–28 (2011).

284. Passow, C. N., Arias-Rodriguez, L. & Tobler, M. Convergent evolution of reduced energy demands in extremophile fish. *PLoS One* **12**, e0186935 (2017).

285. Cao, Y.-Y. *et al.* Evaluation of the Metabolic Effects of Hydrogen Sulfide on the Development of Bombyx mori (Lepidoptera: Bombycidae), Using Liquid Chromatography-Mass Spectrometry-Based Metabolomics. *J. Insect Sci.* **20**, (2020).

286. Lee, Y. *et al.* Inverse correlation between longevity and developmental rate among wild C. elegans strains. *Aging (Albany. NY).* **8**, 986–99 (2016).

287. Mörck, C. & Pilon, M. C. elegans feeding defective mutants have shorter body lengths and increased autophagy. *BMC Dev. Biol.* **6**, 39 (2006).

288. Taormina, G. *et al.* Longevity: Lesson from Model Organisms. *Genes (Basel).* **10**, (2019).

289. Lorenzini, A. How Much Should We Weigh for a Long and Healthy Life Span? The Need to Reconcile Caloric Restriction versus Longevity with Body Mass Index versus Mortality Data. *Front. Endocrinol. (Lausanne).* **5**, 121 (2014).

290. Wagener, A., Müller, U. & Brockmann, G. A. The age of attaining highest body weight correlates with lifespan in a genetically obese mouse model. *Nutr. Diabetes* **3**, e62 (2013).

291. Chmielewski, P. P. The association between body height and longevity: evidence from a national population sample. *Folia Morphol. (Warsz).* **83**, 139–145 (2024).

292. Semenza, G. L., Roth, P. H., Fang, H. M. & Wang, G. L. Transcriptional regulation of genes encoding glycolytic enzymes by hypoxia-inducible factor 1. *J. Biol. Chem.* **269**, 23757–63 (1994).

293. Kim, J., Tchernyshyov, I., Semenza, G. L. & Dang, C. V. HIF-1-mediated expression of pyruvate dehydrogenase kinase: a metabolic switch required for cellular adaptation to hypoxia. *Cell Metab.* **3**, 177–85 (2006).

294. Kurban, G. *et al.* Collagen matrix assembly is driven by the interaction of von

Hippel-Lindau tumor suppressor protein with hydroxylated collagen IV alpha 2. *Oncogene* **27**, 1004–1012 (2008).

295. Kurban, G., Hudon, V., Duplan, E., Ohh, M. & Pause, A. Characterization of a von Hippel Lindau Pathway Involved in Extracellular Matrix Remodeling, Cell Invasion, and Angiogenesis. *Cancer Res* **66**, 1313–1322 (2006).

296. Belanger, A. J. *et al.* Hypoxia-inducible factor 1 mediates hypoxia-induced cardiomyocyte lipid accumulation by reducing the DNA binding activity of peroxisome proliferator-activated receptor alpha/retinoid X receptor. *Biochem. Biophys. Res. Commun.* **364**, 567–72 (2007).

297. Koritzinsky, M. *et al.* Gene expression during acute and prolonged hypoxia is regulated by distinct mechanisms of translational control. *EMBO J.* **25**, 1114–25 (2006).

298. UniProt Consortium. CYSL-2 – Cysteine synthase-like protein 2 [Caenorhabditis elegans]. https://www.uniprot.org/uniprotkb/O45679 (2023).

299. UniProt Consortium. CYSL-3 – Cysteine synthase-like protein 3 [Caenorhabditis elegans]. https://www.uniprot.org/uniprotkb/O01592 (2023).

300. UniProt Consortium. CYSL-4 – Cysteine synthase-like protein 4 [Caenorhabditis elegans]. https://www.uniprot.org/uniprotkb/O16284 (2023).

301. Patange, O., Breen, P., Arsuffi, G. & Ruvkun, G. Hydrogen sulfide mediates the interaction between C. elegans and Actinobacteria from its natural microbial environment. *Cell Rep.* **44**, 115170 (2025).

302. Jackson, M. R., Loll, P. J. & Jorns, M. S. X-Ray Structure of Human Sulfide:Quinone Oxidoreductase: Insights into the Mechanism of Mitochondrial Hydrogen Sulfide Oxidation. *Structure* **27**, 794-805.e4 (2019).

303. Moosavi, B., Berry, E. A., Zhu, X.-L., Yang, W.-C. & Yang, G.-F. The assembly of succinate dehydrogenase: a key enzyme in bioenergetics. *Cell. Mol. Life Sci.* **76**, 4023–4042 (2019).

304. Banerjee, R. & Kumar, R. Gas regulation of complex II reversal via electron shunting to fumarate in the mammalian ETC. *Trends Biochem. Sci.* **47**, 689–698 (2022).

305. Jiang, J. *et al.* Hydrogen Sulfide--Mechanisms of Toxicity and Development of an Antidote. *Sci. Rep.* **6**, 20831 (2016).

306. Dai, D.-F., Chiao, Y. A., Marcinek, D. J., Szeto, H. H. & Rabinovitch, P. S. Mitochondrial oxidative stress in aging and healthspan. *Longev. Heal.* **3**, 6 (2014).

307. Wang, Y., Oxer, D. & Hekimi, S. Mitochondrial function and lifespan of mice with controlled ubiquinone biosynthesis. *Nat. Commun.* **6**, 6393 (2015).

308. Feng, J., Bussière, F. & Hekimi, S. Mitochondrial electron transport is a key determinant of life span in Caenorhabditis elegans. *Dev. Cell* **1**, 633–44 (2001).

309. Treinin, M. *et al.* HIF-1 is required for heat acclimation in the nematode Caenorhabditis elegans. *Physiol. Genomics* **14**, 17–24 (2003).

310. Hwang, A. B. *et al.* Feedback regulation via AMPK and HIF-1 mediates ROS-dependent longevity in Caenorhabditis elegans. *Proc. Natl. Acad. Sci. U. S. A.* **111**, E4458-67 (2014).

311. Cochemé, H. M. & Murphy, M. P. Complex I is the major site of mitochondrial superoxide production by paraquat. *J. Biol. Chem.* **283**, 1786–98 (2008).

312. Castello, P. R., Drechsel, D. A. & Patel, M. Mitochondria are a major source of paraquat-induced reactive oxygen species production in the brain. *J. Biol. Chem.* **282**, 14186–93 (2007).

313. Ramachandran, P. V *et al.* Lysosomal Signaling Promotes Longevity by Adjusting Mitochondrial Activity. *Dev. Cell* **48**, 685-696.e5 (2019).

314. Hansen, M., Hsu, A.-L., Dillin, A. & Kenyon, C. New genes tied to endocrine, metabolic, and dietary regulation of lifespan from a Caenorhabditis elegans genomic RNAi screen. *PLoS Genet.* **1**, 119–28 (2005).

315. Melo, J. A. & Ruvkun, G. Inactivation of conserved C. elegans genes engages pathogen- and xenobiotic-associated defenses. *Cell* **149**, 452–66 (2012).

316. Munkácsy, E. & Rea, S. L. The paradox of mitochondrial dysfunction and extended longevity. *Exp. Gerontol.* **56**, 221–33 (2014).

317. Miwa, S. *et al.* Low abundance of the matrix arm of complex I in mitochondria predicts longevity in mice. *Nat. Commun.* **5**, 3837 (2014).

318. McElroy, G. S. *et al.* Reduced expression of mitochondrial complex I subunit Ndufs2 does not impact healthspan in mice. *Sci. Rep.* **12**, 5196 (2022).

319. Yuan, Y. *et al.* Enhanced energy metabolism contributes to the extended life span of calorie-restricted Caenorhabditis elegans. *J. Biol. Chem.* **287**, 31414–26 (2012).

320. Ng, L. T. *et al.* Lifespan and healthspan benefits of exogenous H2S in C. elegans are independent from effects downstream of eat-2 mutation. *NPJ aging Mech. Dis.* **6**, 6 (2020).

321. Friedman, L. *et al.* Prolyl 4-hydroxylase is required for viability and morphogenesis in Caenorhabditis elegans. *Proc. Natl. Acad. Sci. U. S. A.* **97**, 4736–41 (2000).

322. Tullet, J. M. A. *et al.* Direct Inhibition of the Longevity-Promoting Factor SKN-1 by Insulin-like Signaling in C. elegans. *Cell* **132**, 1025–1038 (2008).

323. Ayyadevara, S. *et al.* Lifespan extension in hypomorphic daf-2 mutants of Caenorhabditis elegans is partially mediated by glutathione transferase CeGSTP2-2. *Aging Cell* **4**, 299–307 (2005).

324. Dancy, B. M. *et al.* Glutathione S-transferase mediates an ageing response to

mitochondrial dysfunction. *Mech. Ageing Dev.* **153**, 14–21 (2016).

325. Lee, S., Lim, G.-E., Kim, Y.-N., Koo, H.-S. & Shim, J. AP2M1 Supports TGF-β Signals to Promote Collagen Expression by Inhibiting Caveolin Expression. *Int. J. Mol. Sci.* **22**, (2021).

326. Pendyala, L. *et al.* Intravenous ifosfamide/mesna is associated with depletion of plasma thiols without depletion of leukocyte glutathione. *Clin. Cancer Res.* **6**, 1314–21 (2000).

327. Zhang, M. Y., Dugbartey, G. J., Juriasingani, S. & Sener, A. Hydrogen Sulfide Metabolite, Sodium Thiosulfate: Clinical Applications and Underlying Molecular Mechanisms. *Int. J. Mol. Sci.* **22**, (2021).

328. Lv, S., Li, X., Zhao, S., Liu, H. & Wang, H. The Role of the Signaling Pathways Involved in the Protective Effect of Exogenous Hydrogen Sulfide on Myocardial Ischemia-Reperfusion Injury. *Front. cell Dev. Biol.* **9**, 723569 (2021).

329. Eltzschig, H. K. & Eckle, T. Ischemia and reperfusion--from mechanism to translation. *Nat. Med.* **17**, 1391–401 (2011).

330. Powell-Coffman, J. A. Hypoxia signaling and resistance in C. elegans. *Trends Endocrinol. Metab.* **21**, 435–40 (2010).

331. Long, Z. *et al.* Targeting ferroptosis: a new therapeutic opportunity for kidney diseases. *Front. Immunol.* **15**, 1435139 (2024).

332. Zhou, K. I., Pincus, Z. & Slack, F. J. Longevity and stress in Caenorhabditis elegans. *Aging* vol. 3 733–753 at https://doi.org/100367 [pii] (2011).

333. Brown-Borg, H. M. Longevity in mice: is stress resistance a common factor? *Age (Dordr).* **28**, 145–62 (2006).

334. Mashiach, E. *et al.* Mesna: a novel renoprotective antioxidant in ischaemic acute renal failure. *Nephrol. Dial. Transplant.* **16**, 542–551 (2001).

335. Son, W.-C., Kamino, K., Lee, Y.-S. & Kang, K.-S. Lack of effects of sodium 2-mercaptoethane sulfonate (mesna) on Ochratoxin A induced renal tumorigenicity following life-time oral administration of Ochratoxin A in DA and Lewis rats. *Toxicol. Lett.* **142**, 19–27 (2003).

336. European Chemicals Agency. Mesna - Registration Dossier. at https://echa.europa.eu/registration-dossier/-/registered-dossier/10923/7/8.

337. Kimura, Y. *et al.* 3-Mercaptopyruvate sulfurtransferase produces potential redox regulators cysteine- and glutathione-persulfide (Cys-SSH and GSSH) together with signaling molecules H2S2, H2S3 and H2S. *Sci. Rep.* **7**, 10459 (2017).

338. Zainol Abidin, Q. H. *et al.* Synthesis of Sulfides and Persulfides Is Not Impeded by Disruption of Three Canonical Enzymes in Sulfur Metabolism. *Antioxidants (Basel, Switzerland)* **12**, (2023).

339. Kim, Y. C. & Hummer, G. Proton-pumping mechanism of cytochrome c oxidase:

a kinetic master-equation approach. *Biochim. Biophys. Acta* **1817**, 526–36 (2012).

340. Nicholls, P., Marshall, D. C., Cooper, C. E. & Wilson, M. T. Sulfide inhibition of and metabolism by cytochrome c oxidase. *Biochem. Soc. Trans.* **41**, 1312–6 (2013).

341. Murphy, B., Bhattacharya, R. & Mukherjee, P. Hydrogen sulfide signaling in mitochondria and disease. *FASEB J.* **33**, 13098–13125 (2019).

342. Guan, H., Sun, J., Liang, X. & Yao, W. Protective Role of Cytochrome C Oxidase 5A (COX5A) against Mitochondrial Disorder and Oxidative Stress in VSMC Phenotypic Modulation and Neointima Formation. *Curr. Vasc. Pharmacol.* **21**, 128–142 (2023).

343. Radin, I., Kost, L., Gey, U., Steinebrunner, I. & Rödel, G. The mitochondrial copper chaperone COX11 has an additional role in cellular redox homeostasis. *PLoS One* **16**, e0261465 (2021).

344. Aschner, M. *et al.* Hydrogen Sulfide (H2S) Signaling as a Protective Mechanism against Endogenous and Exogenous Neurotoxicants. *Curr. Neuropharmacol.* **20**, 1908–1924 (2022).

345. Sasaki, H., Sugiyama, M. & Sasaki, N. Establishment of renal proximal tubule cell lines derived from the kidney of p53 knockout mice. *Cytotechnology* **71**, 45–56 (2019).

346. Brezis, M. & Rosen, S. Hypoxia of the renal medulla--its implications for disease. *N. Engl. J. Med.* **332**, 647–55 (1995).

347. Gai, Z., Gui, T., Kullak-Ublick, G. A., Li, Y. & Visentin, M. The Role of Mitochondria in Drug-Induced Kidney Injury. *Front. Physiol.* **11**, 1079 (2020).

348. Alam, M. M. *et al.* Contribution of NRF2 to sulfur metabolism and mitochondrial activity. *Redox Biol.* **60**, 102624 (2023).

349. Suzuki, R., Hotta, K. & Oka, K. Transitional correlation between inner-membrane potential and ATP levels of neuronal mitochondria. *Sci. Rep.* **8**, 2993 (2018).